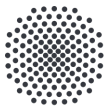# Coolability of Volumetrically Heated Particle Beds

Muhammad Rashid

Universität Stuttgart
Institut für Kernenergetik
und Energiesysteme

Coolability of Volumetrically Heated Particle Beds

Von der Fakultät Energie-, Verfahrens- und Biotechnik
der Universität Stuttgart zur Erlangung der Würde eines
Doktor-Ingenieurs (Dr.-Ing.) genehmigte Abhandlung

vorgelegt von

M. Sc. Muhammad Rashid
geboren in Vehari, Pakistan

Hauptberichter:
Prof. Dr.-Ing. habil. Eckart Laurien

Mitberichter:
Hon. Prof. Dr.-Ing. Michael Durst

Tag der Einreichung:
10.11.2016

Tag der mündlichen Prüfung:
22.03.2017

IKE

Acknowledgments

M. Rashid

Abstract

In case of a severe nuclear reactor accident, with loss of coolant, a particle bed may be formed from the fragmentation of the molten core in the residual water at different stages of the accident. To avoid further propagation of the accident and maintain the integrity of the reactor pressure vessel, the decay heat of the particle bed must be removed. To better understand the various thermo-hydraulic processes within such heat-generating particle beds, the existing DEBRIS test facility at IKE has been modified to be able to perform novel boiling, dryout and quenching experiments. The essential experimental data includes the pressure gradients measured by 8 differential pressure transducers along the bed height as a function of liquid and vapour superficial velocities, the determination of local dryout heat fluxes for different system pressures as well as the local temperature distribution measured by a set of 51 thermocouples installed inside the particle bed. The experiments were carried out for two different particle beds: a polydispersed particle bed which consisted of stainless steel balls ($2\ mm$, $3\ mm$ and $6\ mm$ diameters) and an irregular particle bed which consisted of a mixture of steel balls ($3\ mm$ and $6mm$) and irregularly shaped Al_2O_3 particles. Additionally, all experiments were carried out for different flow conditions, such as the reference case of passive 1D top-flooding, 1D bottom flooding (driven by external pumps and different downcomer configurations) and 2D top-/bottom-/lateral flooding with a perforated downcomer.

In this work, it has been observed that for both particle beds with downcomer configurations an open downcomer leads to the best coolability (dryout heat flux = 1560 kW/m^2, polydispersed particle bed, psys = 1 bar) of the particle bed, mainly due to bottom-flow with enhanced natural convection. It has also been shown that a potential lateral flow via a perforation of the downcomer does not bring any further improvements in coolability. By contrast, in comparison to the open (non-perforated) downcomer the measured dryout heat flux was reduced by 40% to 956 kW/m^2. However, both downcomer configurations lead to a better coolability in comparison to the reference case of pure top-flooding (dryout heat flux = 738 kW/m^2). The dryout heat flux values along with the pressure-drop data can further be used for the validation of numerical models used in simulation codes.

Kurzfassung

Im Fall eines schweren Kernreaktorunfalls mit Verlust von Kühlwasser kann geschmolzenes Kernmaterial durch Kontakt mit im Reaktordruckbehälter verbliebenem Restkühlwasser fragmentiert werden, wodurch eine Schüttung aus einzelnen Partikeln entsteht. Die Nachzerfallswärme dieser Partikelschüttung muss abgeführt werden, um die Integrität des Reaktordruckbehälters zu gewährleisten und das weitere Voranschreiten des Unfalls zu verhindern. Um die verschiedenen thermohydraulischen Vorgänge im Inneren von sich selbst erwärmenden Partikelschüttungen besser zu verstehen, wurde die vorhandene IKE-Versuchsanlage DEBRIS für spezifische Experimente zum Siede-/Dryout- und Flut (Quench)-Verhalten von Partikelschüttungen (Kühlmittel Wasser) modifiziert. Die wesentlichen experimentellen Messdaten sind mit acht piezoresistiven Drucksensoren entlang der Schüttbetthöhe ermittelte Druckgradienten als Funktion der Leerrohrgeschwindigkeiten von flüssiger und dampfförmiger Kühlmittelphase. Zudem wurden lokale Dryout-Wärmestromdichten für verschiedene Systemdrücke sowie lokale Temperaturverteilungen mit Hilfe von 51 in der Schüttung verteilten Thermoelementen bestimmt. Die Experimente wurden mit zwei verschiedenen Schüttbetten durchgeführt, zum einen mit einer polydispersen Schüttung aus Edelstahlkugeln (2 mm, 4 mm und 6 mm Durchmesser) und zum anderen mit einer Schüttung aus einer Mischung von Edelstahlkugeln (3 mm und 6 mm Durchmesser) und unregelmäßig geformten Al_2O_3-Partikeln. Alle Experimente wurden für unterschiedliche Strömungsbedingungen durchgeführt, u. a. mit passiv getriebenem Kühlmittelzustrom in der Schüttung von oben (1D top-flooding) als Referenzfall, einem Kühlmittelzustrom in der Schüttung von unten, bei Zwangskonvektion mittels Pumpe und passiv getriebenem Naturumlauf innerhalb der Schüttung bei verschiedenen Downcomer-Konfigurationen (1D bottom-flooding) sowie mit einem passiv getriebenen Kühlmittelzustrom von oben/unten/seitlich über einen perforierten Downcomer (Zentralrohr, 2D top-/bottom-/lateral-flooding). Im Rahmen dieser Arbeit konnte für die Schüttbetten mit Downcomer-Konfigurationen gezeigt werden, dass mit der offenen Downcomer-Konfiguration die beste Kühlbarkeit erreicht wird (Dryout-Wärmestromdichte 1560 kW/m^2, polydisperse Schüttung, p_{sys}= 1 bar). Dies ist im Wesentlichen auf eine verbesserte natürliche

Konvektionsströmung innerhalb der Schüttung zurückzuführen, die durch die Kühlmittelzufuhr über den Downcomer im Bodenbereich der Schüttung hervorgerufen wird. Es konnte ebenfalls gezeigt werden, dass mögliche laterale Strömungen, die durch eine Perforierung des Downcomers ermöglicht wurden, zu keiner weiteren Verbesserung der Kühlbarkeit führen. Im Vergleich zum Downcomer ohne Perforierung wurde mit 956 kW/m^2 sogar eine um 40 % reduzierte Dryout-Wärmestromdichte ermittelt. Allerdings erzielten beide Downcomer-Konfigurationen eine Verbesserung der Kühlbarkeit im Vergleich zum Referenzfall (Dryout-Wärmestromdichte 738 kW/m^2). Die ermittelten Dryout-Wärmestromdichten und Druckgradienten können weiterhin für die Validierung von numerischen Modellen, die in Simulationscodes implementiert sind, verwendet werden.

Contents

Nomenclature

A	$[m^2]$	cross sectional area
c_p	$[kJ.kg^{-1}.K^{-1}]$	specific heat capacity
d_a	$[m]$	area mean diameter
d_e	$[m]$	effective particle diameter
d_l	$[m]$	length mean diameter
d_m	$[m]$	mass mean diameter
d_n	$[m]$	number mean diameter
d_v	$[m]$	volume mean diameter
F_i	$[N/m^3]$	interfacial friction force
g	$[m/s^2]$	gravity acceleration
G_g	$[kg/m^2.s]$	vapor mass-flux density
h	$[m]$	bed height
h_{fg}	$[kJ/kg]$	heat of vaporization (latent heat)
J	$[m/s]$	superficial velocity
J_l^0	$[m/s]$	liquid inlet superficial velocity
J_l	$[m/s]$	liquid superficial velocity
J_g	$[m/s]$	gas superficial velocity
K	$[m^2]$	permeability of porous medium
$K_{rel,g}, K_{rel,l}$	$[-]$	relative permeabilities of gas and liquid phases
p_{sys}	$[Pa]$	pressure
Q_{vol}	$[kW/m^3]$	volumetric heat input
q	$[kW/m^2]$	heat flux density
T	$[°C]$	temperature
T_{sat}	$[°C]$	saturation temperature
t	$[s]$	time
z	$[m]$	axial coordinate

Nomenclature

Greek Letters

α	$[-]$	void fraction
ϵ	$[-]$	porosity
η	$[m]$	passability of porous medium 5pt
$\eta_{rel,g}, \eta_{rel,l}$	$[-]$	relative passabilities of gas and liquid phases
ρ	$[kg/m^3]$	density
σ	$[N/m]$	surface tension

Abbreviations

AMM	accident management measures
BWR	boiling water reactor
CCFL	counter-current flooding limit
CCM	corium-coolant mixing
DC	downcomer
DHF	dryout heat flux density
EPR	European pressureized reactor
FCI	fuel/coolant interaction
IPB	irregular particle bed
NPP	nuclear power plant
NPS	nuclear power station
PDB	polydispersed particle bed
perf	perforated
PTFE	polytetrafluorethylen (teflon)
TMI-2	three miles island unit 2
RPV	reactor pressure vessel
SAM	severe accident management

List of Figures

List of Tables

Chapter 1

Introduction

The increased demand for nuclear energy across the globe has lead to technological developments in the field of nuclear power plants, with a significant focus being placed on the safety implications of an increase in nuclear energy. When it comes to nuclear-reactor safety, the foremost strategy adopted is to prevent accidents in order to ensure the safe operation of nuclear power plants. One of the most important aspects of preventative safety strategies is "coolability", i.e. maintaining the coolable state of the fuel rods by transporting the residual heat out of the fuel assembly, as well as maintaining "long-term coolability". Under normal operating conditions, even after the reactor has been shut down, heat is produced by the radioactive decay of fission products. Therefore, in order to achieve long-term coolability, the safe removal of this heat (decay heat) from the reactor core for an extended period of time is necessary. State-of-the-art reactor core cooling systems capable of achieving both coolable state and long-term coolability are currently in place. Such core cooling systems play a vital role in maintaining safety barriers in plant operation by providing an adequate amount of coolant to transport both residual and decay heat out of the reactor core.

Secondly, in the case of the failure of accident prevention measures, new and effective plans necessary for dealing with these accidental damages to the public and environment must be considered. Such failure could be caused by human error or natural disasters, such as the Three Miles Island-2 (TMI2) accident [1] and the Fukushima Daiichi nuclear power plant (NPP) accident, caused by an earthquake and tsunami, respectively.

An unprecedented and severe accident scenario caused by human error or resulting from a natural disaster beyond the scope of plant design may result in the failure of all available reactor cooling systems. Due to the presence of decay heat and absence of adequate coolant, the reactor core may dry out, heat up, and eventually melt down. At very high temperatures, the exothermic reaction between Zirconium (fuel rod cladding)

and the superheated steam adds to the severity of the situation. If the molten corium ($UO_2 + ZrO_2 + structural\ materials$) is not sufficiently cooled down, the reactor pressure vessel (RPV) may fail, and, subsequently, the molten corium may relocate to the lower plenum of the reactor. The failure to stop the progression of the molten corium may breach all safety barriers and pose great risk of damage to the public and the environment.

1.1 Debris Bed Formation

In the event of a severe nuclear accident with loss of coolant, the hot corium, on coming in contact with the residual water, will fragmentise to form a debris bed. In light water reactors (LWRs), the formation of a debris bed can be described as "in-vessel formation" (see Figure 1.1) and "ex-vessel formation" (see Figure 1.2). Debris bed formations take place due to a possible interaction of hot corium melt and water. When a severe accident occurs, even after the reactor has been shut down, the core fuel continues to generate decay heat. At the same time, the failure of all cooling systems will result in a lack of supply of the coolant to transport the decay heat out of the system. The evaporation of available water will result in a decreased water level, and the core would be uncovered and eventually dryout. This dryout would result in the high temperatures of fuel rods and core materials. At temperatures above 1500 K, the exothermic reaction between the Zirconium of the fuel rod cladding and the superheated steam produces additional heat at high rates, which leads to an accelerated increase in temperature and the degradation process.

At this stage in the accident, the restoration of the cooling systems will bring hot rods directly in contact with the coolant and give rise to thermal stresses. Due to such thermal stresses, the rods may crumble and form a debris bed surrounded by intact core regions. In order to achieve a stable, coolable state in the core, the hot debris bed must be cooled down to coolant saturation temperatures through quenching (i.e. re-flooding the bed).

If the core is not maintained at a stable condition, the presence of decay heat in the debris bed may again lead to an increase in temperatures and a meltdown. With a continued temperature increase, depending upon the physical properties of the materials, different materials would melt down at different times (see Figure 1.3), and the molten core would relocate into the lower core regions. In adition to decay heat, the heat-up of the core is determined by the cooling conditions imposed by the residual water level in the core, leading to maximum temperatures in the central part of the upper third of the core. The core parts still covered with water are sufficiently cooled, while the heatup in the upper regions is partly delayed by cooling by the steam flow [2]. Due to the presence of a larger
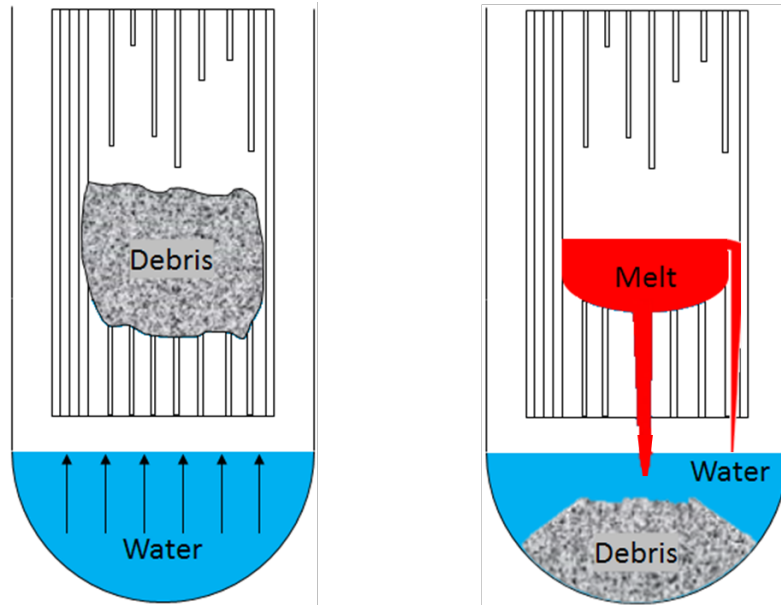
Figure 1.1: In-vessel particulate debris bed formation [59].

temperature gradient, a crust would form, and the molten material will accumulate on the crust [3]. The stability of the crust depends on its coolability, e.g. via heat conduction, radiation, and steam flow. With poor coolability of the crust, the melt would almost directly flow into the lower head of the plenum, and, with better coolability of the crust, large melt pools will be formed. Depending upon the heat flux distribution in the inner melt pool, the inner boundaries, and the heat removal rate, the crust may fail, leading to the release of the melt pool into the lower head of the RPV. The melt may release laterally from the upper region, or may release at different mass fluxes directly downwards through the bottom. Coming into contact with the residual water, the molten core may form a particle debris bed. The debris bed formation process directly depends on the mass flux of the melt jets [4], [5]. Keeping the reactor safety perspective in mind, small mass fluxes are favorable, since they result in better melt fragmentation, whereas, in the case of larger mass fluxes, the interaction between the melt and the residual water is limited. This not only may result in the formation of the melt pool in the lower head, but may also lead to a steam explosion. In reactor typical cases, the expected system pressure strongly depends on the reactor type, as well as the accident history. For pressurised water reactors, significantly higher pressures are possible in the vessel. But, due to depressurisation, either automatically, or manually by accident management measures, system pressures below 10 bar could be expected. For ex-vessel particles, an upper limit for the pressure is given by the maximum pressure load of the containment. Dependent on the reactor type, a maximum system pressure of about 10 bar (1 MPa) may be assumed [6].
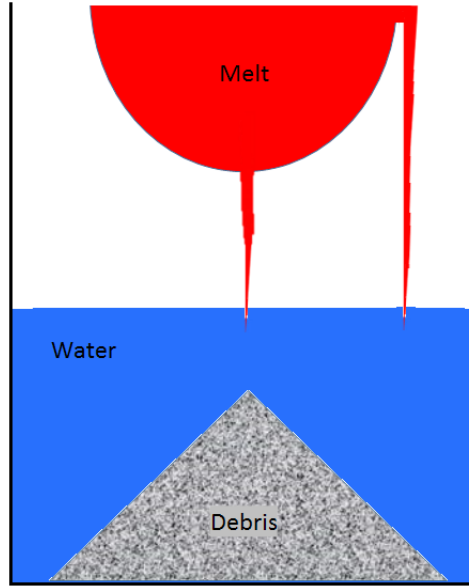
Figure 1.2: Ex-vessel particulate debris bed formation (in the reactor cavity).

To ensure the retention of the nuclear material inside the RPV, the dryout and subsequent melting of the material must be prevented. This could be achieved by refilling the water pool in which the debris bed is immersed, either by re-flooding or through condensation of the steam escaping from the debris bed. While the steam leaves the debris bed, the surrounding water must provide water influx to replace the evaporated water inside the debris bed. These phenomena result in the natural circulation of water and hence support the achievement of the long-term coolability of the nuclear material in the lower head of the RPV. At this stage in the accident, failure to achieve long-term coolability would result in the dryout and melt down of the heat-generating nuclear material and may form a melt pool at the bottom of the RPV, thus putting the integrity of the RPV at risk. If no counter measures can be taken (e.g. flooding the reactor cavity and thereby cooling the RPV from outside) "in-vessel retention", as proposed for some Westinghouse Advanced Pressurized Water reactors, AP-600 (Theofanous, et al. [7])), the lower head will fail, leading to melt outflow from the RPV (ex-vessel scenario).

The melt released into the reactor cavity will put the integrity of the containment in danger. The melt must be retained inside the containment by achieving long-term coolability of the nuclear material. Failure to do so would breach the containment foundation and would release radioactive material into the environment, which would have severe consequences. In addition to emergency cooling systems, accident management measures (AMM) are being introduced in nuclear power plants to prevent melt release into the environment by retaining the nuclear material within the cavity.
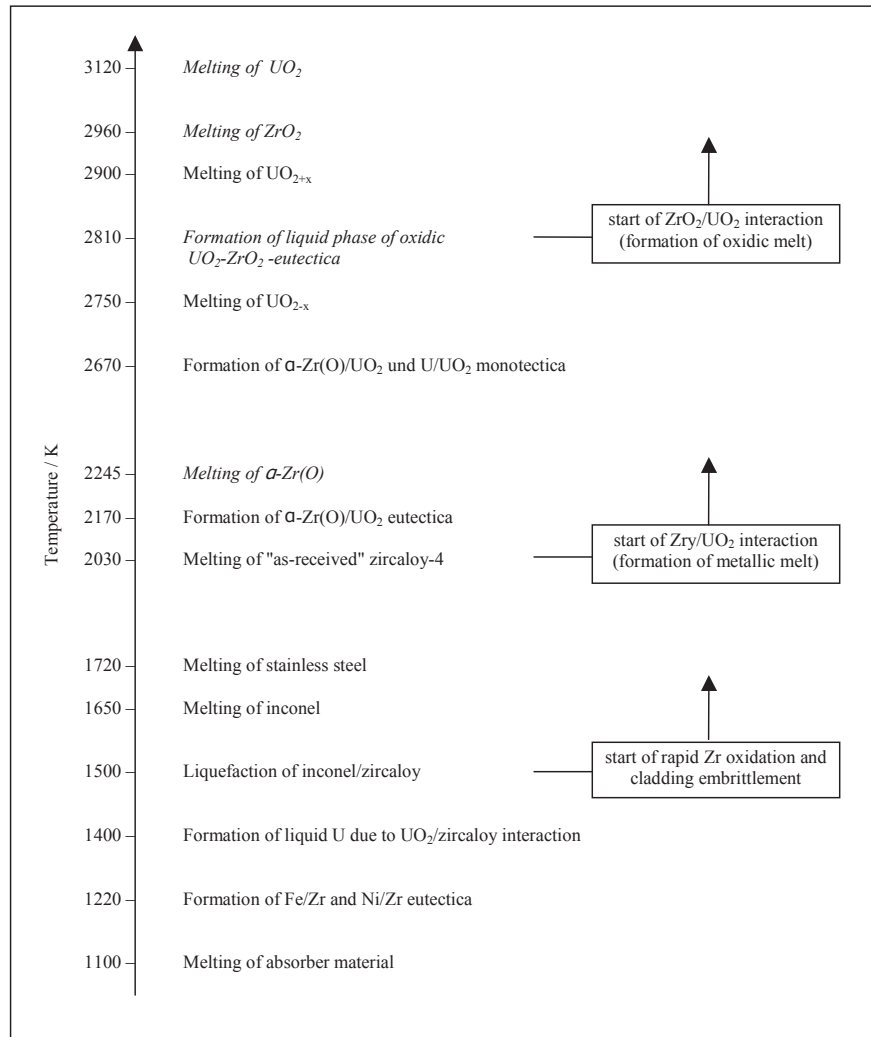
Figure 1.3: Chemical interactions and formation of liquid phases in the core with increasing temperature [2].

The reactor cavity can be assumed to be filled with water, especially in the case of the boiling water reactor (BWR), wherein water pools 7-10 m deep are foreseen; in existing PWRs, only about 1-2 m of water depth is expected. The melt flowing out of the broken vessel pours into this water. Again, as described above for the lower head, the melt jet breaks up and fragments, leading to the formation of a debris bed. A large melt pool can generally be considered less favorable for breakup than a limited diameter of outflow from the RPV. Depending on the size of the vessel breach and the depth of water pool, different bed types may be envisaged. If a melt jet with a limited diameter falls into a deep water pool, a significant breakup of melt and formation of a debris bed is expected again, with good chances of coolability via the surrounding water pool (see Figure 1.2).

To avoid a containment-wall breach in an ex-vessel scenario, different cooling concepts

are being considered. The Tian Wan core catcher and European Pressurized Reactor (EPR) core catcher (see Seiler et al. [8], Sehgal [9], Fischer [10]) can be classified as enclosure concepts, applied for ex-vessel melt retention. The Tian Wan core catcher (see Tian Wan [11]) provides an enlarged and diluted melt pool (through the addition of sacrificial material) and is then cooled from outside. The EPR contains a core catcher in a lateral spreading compartment, where melt is collected, conditioned with sacrificial concrete, and subsequently spread over a large surface area of about 170 m^2. With a combination of top-flooding (adding water from the top) and bottom-flooding (cooling from the bottom via a cooling circuit), it is likely that the melt could be safely retained within the cooling boundaries (see Fischer et al. [12], Bittermann et al. [13]), which would prevent both further accident progression and the release of radioactive material into the environment.

A significant surface increase, based on the breakup of corium (is a lava-like mixture of portions of a nuclear reactor core nuclear fuel, control rods and structural materials of affected components of reactor) while coming in contact with water, is also considered to retain the melt inside the reactor cavity (see Sehgal [9]). This would result in the formation of a debris bed. The porous bed structure, with a much larger surface, enables the ingression of water, which, in turn, enhances the chances of achieving the long-term coolability of corium. The breakup of the corium melt in conjunction with quenching is considered to yield rapid cooling. On the other hand, the breakup of melt is greatly reduced with thicker melt jets as well as with shallow water pools. This may result in bed types containing molten parts that mix with the debris bed on the cavity floor.

In the COMET concept (see Alsmeyer et al. [14], Alsmeyer and Tromm [15]), the breakup of the melt is aided by the bottom injection of water into the melt layer (see Figure 1.4). In this concept, the melt flowing out of the vessel is collected in the dry reactor pit and is allowed to spread over the available cavity area. To provide water supply to the melt from the bottom, a sacrificial layer, including nozzles with plugs, is installed in the cavity foundation. These nozzles are connected to a water pool placed at a higher level. The spreading melt attacks the sacrificial layer, as well as the plugs, and opens the water path. Due to the hydrostatic head, the water is injected through the nozzles into the melt. The water is forced up through the melt and evaporates. The resulting high-volume steam-generation process yields a rapid breakup of the melt. As a result, a solidified structure called 'porous' is formed (see Widmann et al. [16]), from which heat can be removed.

In the recent history of nuclear reactors, we have seen two major and severe accidents involving core meltdown: *Fukushima Daiichi* and *Three Mile Island Unit 2 (TMI-2)*.
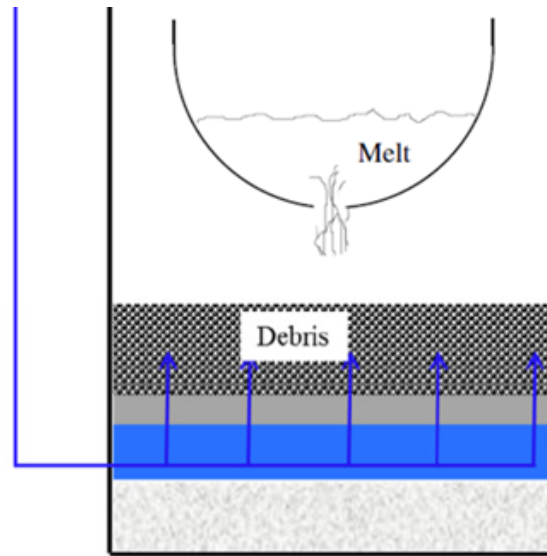
Figure 1.4: Ex-vessel particulate debris in the COMET core catcher [59].

On March 11, 2011, the Fukushima Daiichi Nuclear Power Station (NPS) was hit by an earthquake of magnitude 9.0 on the Richter scale, followed by a tsunami with waves as high as 15 m. Out of a total of six units, three units, 1 to 3, were in operation, and the other three units, 4 to 6, were in maintenance modes. It is likely that Units 1 to 3 were automatically scrammed (shut down by rapid insertion of control rods to stop the nuclear chain reaction) at the time of the earthquake, but external power supplies and almost all in-house AC power supplies were lost due to the earthquake and the tsunami, leading to the failure of the reactor cooling systems.

In the severe accident at Fukushima Daiichi NPS, the reactor cores in the three reactors (1-3) were badly damaged. Reactors and spent fuel pools at the Fukushima Daiichi NPS lost their cooling capabilities. It is likely that the fuel melting occurred at a large scale and that some part of the melt reached the bottom of the containment vessel through the RPV (Takano, et al. [17]). Explosions occurred in Units 1, 3, and 4, presumably caused by the hydrogen released from the core damage and filling the reactor buildings.

On March 28, 1979, an accident involving a loss of coolant took place at Unit 2 of the Three Mile Island plant in Pennsylvania, which resulted in a severely damaged reactor core (see Figure 1.5). This accident was unique in its severity for its time; a large amount of melted core material formed a debris bed while coming in contact with the residual water. A detailed account of the sequence of events during the TMI-2 accident is given by Wolf et al. [3]. During the first phase of the accident, loss of coolant took place in the primary cooling system. The continued decay heat generation via the fuel and insufficient heat removal from the system characterized the second phase of the accident. Due to the
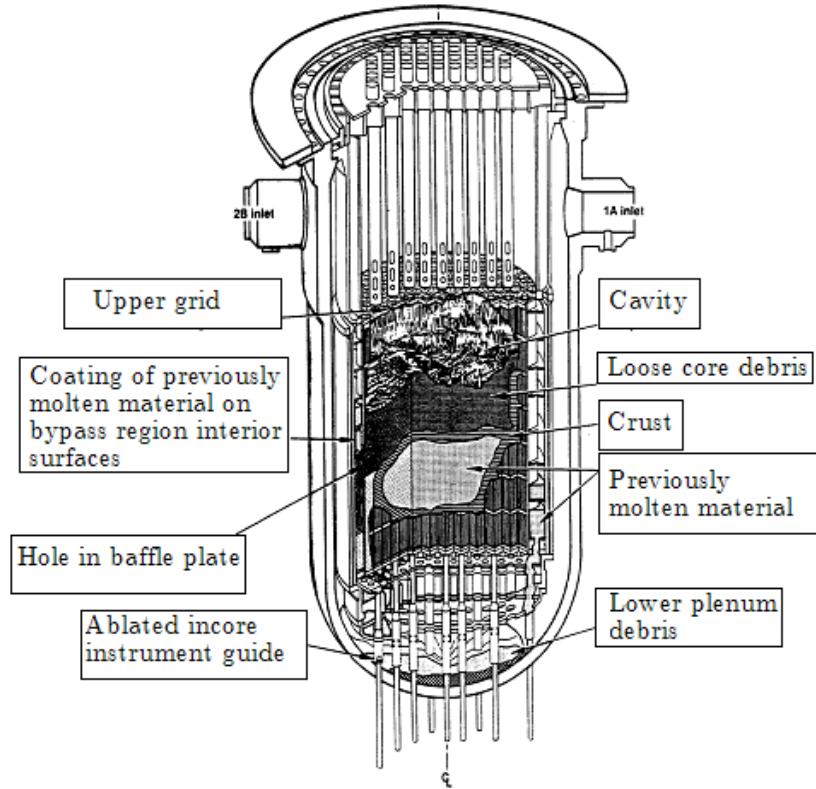
Figure 1.5: TMI-2 RPV final state.[2]

insufficient coolant supply to the vessel, the liquid level in the reactor vessel decreased and partially uncovered the core. Subsequent events led to an increase in temperatures and the meltdown of core material. At the end of the early phase, degraded fuel rods may have collapsed and formed a debris bed in the core region (Dorsselaere et al. [18]). In the later phase of the accident, the core was re-flooded with coolant that induced rapid cooling and thermal shock. The melted core coming in contact with the coolant may have formed a debris bed (Wolf et al. [3]).

The information about the early phases of the accident was gained from post-accident analysis of the measured data and the core types at end-state. The accident scenario up to the time of core relocation at 224 minutes has also been extensively analyzed and reviewed. However, the sequence of events that took place within the reactor vessel during core relocation is not well defined (Kemeny et al. [1], Wolf et al. [3], Richard et al. [19]). Extensive oxidation of the fuel cladding, a partial meltdown of the reactor core, and the release of fission products from the fuel raised questions about the design and safety of nuclear reactors, the integrity of the lower head of the reactor pressure vessel, and the

---

[2]Source: http://www.nrc.gov/images/reading-rm/photo-gallery/20071114-006.jpg

accident progression, as well as accident management strategies (Wolf et al. [3]).

In order to avoid remelting, further propagation of the severe accident, failure of safety barriers and environmental pollution with radioactive material the coolability of heat generating particulate beds must be assumed. Hence, within the scope of severe accident managemetn (SAM) strategies the long-term coolability of heat generating particl beds takes the forefront role and requires detailed understanding of coolability of particle beds. For example in case of restablishment of coolant supply, at a stage when there exists molten core inside the reactor vessel, the direct contact of the coolant with the molten core may result in steam explosion and lead to additional hazards. Therefore, due to the complex nature of the severe accidents comprehensive experiments, especially with regard to the coolability behavior of the particle bed formed as a result of contact between the hot melt and the coolant, are needed to develope a better understanding of the coolability of particle beds which are volumetrically heated by decay heat.

1.2 State of the Art

1.2.1 Experimental Studies

In the aftermath of the TMI-2 accident, different experimental and numerical investigations were initiated in order to gain knowledge, not only about the course of the accident, but also about post-accident phenomena. The main focus has been on debris bed behavior involving the formation of the bed, shape and size investigations of the particles, and, most importantly, the coolability behavior of the debris bed. To gain insight into the particle bed formation, morphology of particles, size distribution and porosity (ratio of the hollow space between particle in a controlled volume, $\varepsilon = V_{hollow}/V_{total}$) of the bed formed, different experiments have been carried out. These experimental studies provide valuable data for carrying out an experimental investigation of the coolability of a debris bed. Spencer et al. [20] performed Corium-Coolant Mixing (CCM) tests at Argonne National Laboratory to investigate molten fuel-coolant interactions for different parameters, e.g. corium mass, water pool depth, water temperature and initial pressure, etc. For different CCM tests, molten corium was poured into a water pool of approximately 1 m in depth. Different CCM tests resulted in heap-like debris beds with loosely bounded particles. The particles formed were of different shapes and sizes. Tests with different parameter variations resulted in particles having diameters of 0.8 mm - 5 mm, with some fragments having diameters of over 10 mm. An effect of higher initial water temperatures, larger melt mass

and jet diameters was observed on the bed porosity (ε). Huhtiniemi et al. [21], [22] developed the KROTOS program at Joint Research Center, Ispra, Italy (JRC-Ispra), focused on the quenching and steam explosion behavior of two different molten materials (Al_2O_3 and $UO_2 - ZrO_2$) in different conditions (water sub-cooling, fuel/coolant mass ratio). The particles formed in these tests were found to be much smaller (with average diameters of $1\ mm$ to $1.7\ mm$) than those found in CCM tests.

Extensive investigations on debris formation were performed by Magallon et al. [23], [24], [25] in the FARO (Fuel melt And Release Oven) test series at JRC-Ispra. They performed fuel coolant interaction (FCI) experiments to study the quench behavior of large amounts of prototypic corium ($UO_2 - ZrO_2$) melt. Heap-like debris beds consisting of different shapes and different particle diameters were observed. The particle size ranged from $0.25\ mm$ to $11\ mm$, with mean particle sizes ranging from $2.5\ mm$ to $4.8\ mm$. In the same experiments, the melt reached the bottom of the test section in liquid form without fragmentation, and agglomerated debris was observed. The COTELS tests [26] in Japan were carried out to investigate the energetic corium-water interaction under ex-vessel conditions. Compared to in-vessel corium, the ex-vessel corium, melted through lower head could contain metalic components, therefore $60\ kg$ mixture of UO_2 and ZrO_2, containing Zr and stainless steel was used. Most of the poured corium broke up, and only a small amount of ingot corium (cake) was found on the pool bottom. The sizes of corium particles ranged from a few hundred microns to more than $10\ mm$. The shape was spherical in the middle sizes, while it was irregular in both the small and large sizes. The particles had many pores not only on their surfaces but also inside.

Quenching and explosion behavior have also been investigated in experiments at the TROI facility in KAERI (South Korea) [27]. During these experiments, the quenching behavior of different molten materials ($ZrO_2 - Zr$ and $UO_2 - ZrO_2 - Zr$) was studied. A significant effect of corium composition on the characteristics of the particles formed was observed. A large number of fine particles with diameters smaller than $0.7\ mm$ were found. Solid as well as hollow-shell debris was found in these experiments. Karbojian et al. [28] have investigated the processes of formation and the characteristics of debris within the framework of the DEFOR (DEbris bed FORmation) program at KTH in Sweden. Different corium simulant materials ($CaO - B_2O_3$, $WO_3 - CaO$, $WO_3 - Bi_2O_3$ or $MnO - TiO_2$) and different parameters (water sub-cooling, depth of water pool) were investigated. A strong influence of water sub-cooling on the spreading of debris on the bottom of the pool and on particle-size distribution was observed. In these tests, the sub-cooling and the water pool depth had a strong influence on the characteristics of the debris formation, e.g. with decreased water pool depth, the molten material could reach the bottom of the pool and
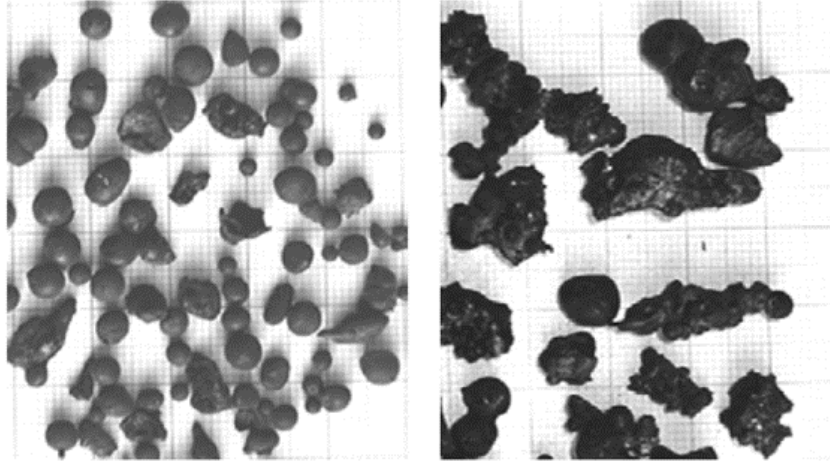
Figure 1.6: Typical shape of fragments collected in PM12 experiment [29].

lead to agglomeration or even cake formation. Kaiser et al. [29] have performed PREMIX (the PREMIXing phase of melt coolant interaction) experiments with a non-radioactive simulant material ($> 90\%$ Al_2O_3 with very small portions of other oxides); $< 10\%$ iron) under realistic conditions. In total, eighteen tests, PM01-PM18, were performed over a span of five years (1994 - 1999) to study the influence of different parameters, e.g. melt mass, degree of sub-cooling, system pressure, and duration of melt release. In most of the PREMIX tests, the particles formed were of a rounded shape or irregular shape with partly hollow porous structures. The typical diameters ranged from 2 mm to 5 mm at the fragment catcher and from 5 mm to 10 mm at the bottom of the facility (see Figure 1.6). The particles from the PREMIX experiments with an equivalent sieve diameter range of 2 mm to ≤ 10 mm were used for this study.

From the investigations of different parameters, such as water depth, system pressure, the sub-cooling of water, and melt composition, a large amount of data on the formation of the debris bed was collected. It has been observed that particles of different shapes (spherical and irregular) and different diameters (1 mm to 10 mm) can be expected. Very high porosity ($\varepsilon = 0.5$ to 0.6) was obtained in some of the DEFOR experiments.

Li and Ma [30] have investigated the effect of particle size, particle-size distribution, and bed porosity (ε) on void fraction and pressure drop through a particle bed formed in a cylindrical test section. In the case of a monodispersed particle bed, composed of single sized particles, the particle diameter is a directly known parameter. Meanwhile, in the case of complex particle beds composed of particles of different sizes, e.g. a polydispersed particle bed and an irregular particle bed, a mean particle diameter (effective diameter d_e) is needed to characterize the particle bed of multi-sized particles. In particle technology

studies, some analytical approaches have been adopted to calculate the mean particle diameter of a mixture of particles of different sizes. Based on different size distribution functions, different mean diameters, e.g. volume mean (d_v), mass mean diameter (d_m), area mean diameter (d_a), length mean diameter (d_l), and number mean diameter (d_n), can be calculated as shown below (see Eq. (1.1) to (1.4)) (Li and Ma, [30], J.F.Richardson et al., [31]):

$$d_v = d_m = \frac{\sum w_i d_i}{\sum w_i} \tag{1.1}$$

$$d_a = \frac{\sum w_i}{\sum (w_i/d_i)} \tag{1.2}$$

$$d_l = \frac{\sum (w_i/d_i)}{\sum (w_i/d_i^2)} \tag{1.3}$$

$$d_n = \frac{\sum (w_i/d_i^2)}{\sum (w_i/d_i^3)} \tag{1.4}$$

where w_i is the mass fraction of particles of i-th size class (diameter d_i) within the given size range. By assuming the same shape of particles (spheres in the case of the polydispersed particle bed) and constant density, mass fraction can also be expressed in terms of diameter (see Eq. (1.5)).

$$w_i = \frac{n_i d_i^3}{\sum n_i d_i^3} \tag{1.5}$$

where n_i is the number of particles of diameter d_i. Any of the above mentioned mean diameter could be used as the effective particle diameter (d_e). However, in this work the effective particle diameter (d_e) is ideally determined by the use of Ergun friction model for single phase flow.

Abe and Sudo [32] have conducted air-water experiments to investigate the counter current flooding limit (CCFL) for a two-phase flow in a porous bed of 200 mm height. The bed was made of glass particles with diameters of 4.5 mm to 14.5 mm. Air and water at specified flow rates were used to simulate the two-phase flow inside the bed. The local void fraction and local pressure distribution measurements were used to estimate the wall and interfacial shear stresses.

Within the framework of the STYX test series at VTT (Technical Research Centre of Finland), Lindholm et al. [33] carried out a dryout test under top-flooding condition by immersing the bed in water (only water supply to the particle bed is from the waterpool above the bed), both for uniformly mixed and stratified bed geometries. The particle bed with a diameter of 300 mm and a depth of 600 mm was placed in a cylindrical container

inside a pressure vessel. The particle bed consisted of mixtures of alumina (Al_2O_3) of different sizes and irregular shapes over a broad particle-size distribution. The sizes of the particles used in these tests ranged from 0.25 mm to 10 mm in diameter. The measured porosity of the bed was $\varepsilon = 0.37$. For heating purposes, an electrical heater module with six horizontal resistance band levels was imbedded in the bed. Based on the single-phase pressure drop measurements, an effective particle diameter of 0.8 mm was calculated from Erguns equation. Under top-flooding conditions, smaller dryout heat flux values were observed, mainly due to the significantly small particle diameter ($< 1 \ mm$).

Zeisberger and Mayinger [34] have experimentally investigated the boiling heat transfer in a particle bed maintained in a glass container of 500 mm x 150 mm. The particle bed was approximately 125 mm in height and had a total bed porosity $\varepsilon \leq 0.2$. Experiments were carried out for a monodispersed bed as well as a mixture of two different particle sizes. The particles used were made of steel spheres of 4.0 mm diameter and glass spheres of 0.95 mm diameter. The bed was heated using an induction coil, and as a coolant the refrigerant R134a (1,1,1,2-tetrafluoroethane) was used at pressures between 0.8 MPa and 1.8 MPa while deionized water was used at pressures between 0.2 MPa and 2.0 MPa. Contrary to small cylindrical types, it was observed that, with a gap at the bottom of the bed, buoyancy-driven convective flows would result inside the test section. Consequently, the flow of coolant into the bottom of the bed increased, and hence the coolability of the bottom region of the bed was improved.

Atkhen and Berthoud [35] have studied the coolability of a debris bed in multidimensional configurations at the SILFIDE facility. Stainless steel spherical particles with diameters of 2, 3.17, and 7.18 mm were used. The particle bed was made in a 500 mm x 600 mm x 100 mm parallelepipedic crucible. The SILFIDE experiments show that, in cases of bottom injection experiments, the coolability of the particle bed is significantly better in terms of CHF values, in comparison to the pure top-flooding experiments.

The COOLOCE experiment series at the VTT Technical Research Centre of Finland were carried out in order to study the effect of the bed geometry on the coolability of the debris bed (Takasuo et al. [36]). They observed that, if the two debris bed configurations have equal height, then the coolability of the conical bed is improved compared to the cylindrical bed due to the multi-dimensional infiltration of water through the surface of the cone.

In addition to long-term coolability of the debris bed, it is necessary to study the cool-down (quenching) behavior of dry hot debris beds. Most recently, two experimental facilities, PRELUDE (Préliminaire sur le Renoyage ExpérimentaL d'Un Lit de Debris) and PEARL, have been set up at the French Institute of Radioprotection and Nuclear

1. INTRODUCTION

Safety (IRSN) to investigate the quenching behavior of hot dry beds. In the PRELUDE test series, G. Repetto et al. [37], [38] performed a series of quenching experiments by flooding the preheated monodispersed bed of stainless steel particles with diameters of 4 mm, 2 mm and 1 mm or polydispersed debris involving different sizes (diameters of 170 mm and 290 mm, and 200 mm to 250 mm height). Quenching experiments were carried out at different fixed inflow rates. Slower quench front progression for smaller particle beds has been observed. Moreover it was also observed that a by-pass around the debris did not enhance the coolability. Tutu et al. [39] at the Brookhaven National Laboratory also experimentally investigated debris quenching under a forced water flow from the bottom, using spherical particles. It has been observed that for smaller liquid inflow rates and lower initial bed temperatures the quench front progresses in a one-dimensional manner, but for large liquid inflow rates and higher initial bed temperatures becomes transient. POMECO (POrous MEdia COolability) experiments were performed at the KTH (Royal Institute of Technology, Stockholm, Sweden) with sand particles to study the quenching of non-uniform, irregularly shaped particles of small size under top- and bottom-flooding conditions (Nayak et al. [40]). In these experiments, a radially stratified bed (consisting of sand particles with a mean diameter range of 0.2 mm to 4.01 mm), heated by conduction from an array of thin heaters, was quenched under top- and bottom-flooding conditions. Experiments were also performed with the installation of a downcomer inside the bed, which enhanced the quenching rate of the hot bed. It was concluded that the quenching rate with pure top-flooding was small and use of downcomer resulted in an improved quenching rate. It was also found that in comparison to the high porosity regions, the lower porosity regions showed slower quench rates.

Tung and Dhir's experiments addressed the quenching behavior of a dry hot debris bed with variable permeability (both radial and axial porosity distributions). They also studied the bottom quenching of a hot particle bed (consisting of steel particles and heated via conduction) with either a constant liquid flow rate or a constant driving head (Tung and Dhir [41]). They observed in the top-flooding experiments that the counter current flooding limit (CCFL) plays a key role in controlling the quench front velocity for an axially stratified bed, whereas, for a radially stratified bed, very little cross-flow at the boundary between the layers was observed. The high porosity region was quenched first while the low porosity region was later quenched in the bottom-flooding mode due to the fill up of the bed.

Sehgal et al. [42] carried out quenching experiments for homogenous and axially stratified sand particle beds, both for top- and bottom-flooding conditions. They found that a low porosity layer and its mean particle size play key roles in determining the quenching

time. Moreover, the quenching under bottom-flooding conditions significantly reduced the quenching time of the particle bed.

The previous test series at the DEBRIS test facility (IKE, University of Stuttgart) have been mainly focused on addressing the issue of the long-term coolability of hot debris beds with monodispersed spherical particles (oxidized stainless steel balls of 3 mm and 6 mm diameter), as well as experiments with a layered bed (3 mm steel balls on top of 6 mm steel balls) [43]. More detailed information about the work by Schäfer et al. can be found in [44] and [45]. These experiments were performed at ambient pressure and increased system pressure of 3 bar and 5 bar in saturation conditions, wherein, the heating power and the coolant mass flow were varied. Furthermore, a series of experiments dealt with the cool-down behavior of a superheated particle bed (6 mm steel balls) flooded either from above or from below with cold water (flooding/quenching experiments). The most important finding of these experiments was the importance of the interphase friction term in calculating the pressure drop behavior of the monodispersed particle bed.

Schäfer also carried out experiments with a polydispersed particle bed [46] of the same bed configuration (particle-size distribution) as used in this work. It has been observed that, for flow conditions with a pure top-flooding scenario, the water can only flow downwards against the upward-flowing steam and leads to a counter-current flow condition inside the particle bed. In general, the pressure gradient (dp/dz) in comparison with the initial value of the pure water column ($\rho_l g$) assumes negative values, as shown in Figure 1.7, wherein the pressure fractions (fluid-particle friction, interphase friction) from the pressure equation Eq. ((1.6) and (1.7)) are presented. For low vapor superficial velocities, the pressure drop is dominantly caused by the interphase friction, whereas the pressure drop caused by the particle-friction term is negligible. With increasing vapor superficial velocity, the influence of the particle friction on the overall pressure gradient increases, while that of the interphase friction term decreases.

1.2.2 Theoretical/Model Studies

The main goal of the experimental studies is not only to provide an understanding of the debris coolability under different thermo-hydraulic conditions, but also to generate an experimental database that could be used for the validation of different numerical codes being developed for reactor safety research. Numerical codes, e.g. the WABE-2D (WAter BEd) code, Schmidt, [6], MEWA (Melt and WAter) code, Buck et al. [47], and ICARE/CATHER, Fichot et al. [48] code developed by IRSN, mainly focus on the modeling of two-phase (water and steam) flow in a solid debris bed. The WABE-2D code deals with the thermo-hydraulic behavior of water and steam in a porous debris bed. The
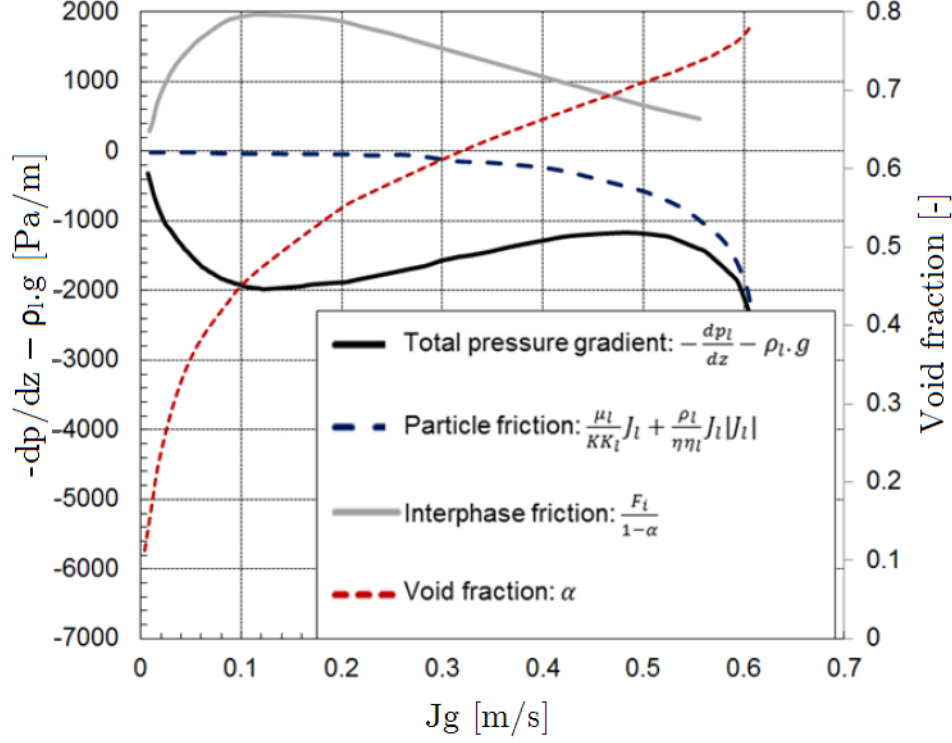
Figure 1.7: Total pressure drop for fluid phase, particle friction, interphase friction, and void fraction for monodispersed 3 mm particle bed, $J_l^0 = 0\ mm/s$, $p_{sys} = 1\ bar$ [44].

MEWA code as part of the German system code ATHLET-CD (Analysis of Thermal-Hydraulics of LEaks and Transients-Core Degradation) is being developed at IKE, University of Stuttgart, to investigate in-/ex-vessel corium behavior. Different modules of the MEWA code deal with a wider range of issues involved in reactor safety, including core melting, melt relocation, melt pool formation, and the thermo-hydraulic behavior of two-phase flow in a porous debris bed. Such numerical codes still under development and continuously apply to the debris experiments to justify the empirical correlations used in the models. The flow inside the debris bed is mainly governed by the pressure drop which consists of the hydrostatic part (index g) and the friction part (index F).

$$\left(-\frac{dp}{dz}\right)_{tot} = \left(-\frac{dp}{dz}\right)_g + \left(-\frac{dp}{dz}\right)_F \ where \ \left(-\frac{dp}{dz}\right)_g = \rho g \tag{1.6}$$

Following the approach taken by Darcy [49], the pressure loss for single-phase flow is proportional to the superficial velocity defined by an empirical formula.

$$\left(-\frac{dp}{dz}\right)_F = \frac{\mu}{K}J \tag{1.7}$$

Ergun [50] extended Darcy's model to take into account the turbulent term.

$$\left(-\frac{dp}{dz}\right)_F = \frac{\mu}{K}J + \frac{\rho}{\eta}J|J| \tag{1.8}$$

where μ, ρ, K, η and J are the dynamic viscosity, density of the fluid, permeability of the porous medium, passability of the porous medium, and superficial velocity of the fluid. The superficial velocity J represents the volume flow of the fluid based on the total flow cross-section with no debris inside the pipe or cylinder. The permeability K and passability η describe the permeability of the porous medium due to its geometric properties (porosity ε, particle diameter d_{p}). Compared to total flow cross section (i.e. considering no debris inside a pipe or cylinder) they also take into account the reduction in the cross-section and increase in the flow path of the fluid and are defined by Eq. (1.9) and Eq. (1.10) (Kaviany, [51]).

$$K = \frac{d_p^2 \varepsilon^3}{C_1(1-\varepsilon)^2} \, [m^2] \qquad (1.9) \qquad\qquad \eta = \frac{d_p \varepsilon^3}{C_2(1-\varepsilon)} \, [m] \qquad (1.10)$$

where the parameters C_1 and C_2 (Kozeny-Karman parameters) can be obtained from pressure-drop measurements for particle beds and usually have values of $C_1 = 150$, and $C_2 = 1.75$, which are applicable to a wide range of materials and flows.

For the two-phase flow, in order to take into account the enhanced friction effects caused by the presence of the other phase, the extended Ergun equations include additional factors, known as the relative permeabilities K_{rel} and passabilities η_{rel}.

$$\left(-\frac{dp_l}{dz}\right) = \rho_l g + \frac{\mu_l}{KK_{rel,l}}J_l + \frac{\rho_l}{\eta\eta_{rel,l}}J_l|J_l| \tag{1.11}$$

$$\left(-\frac{dp_g}{dz}\right) = \rho_g g + \frac{\mu_g}{KK_{rel,g}}J_g + \frac{\rho_g}{\eta\eta_{rel,g}}J_g|J_g| \tag{1.12}$$

The relative permeabilities and passabilities are usually defined as a function of the volumetric vapor content α and have a significant influence on the calculation of pressure drop or the maximum heat flux from the bed.

$$K_{rel,g}(\alpha) = \alpha^n \qquad\qquad\qquad K_{rel,g}(\alpha) = \alpha^m \tag{1.13}$$

$$K_{rel,l}(1-\alpha) = \alpha^n \qquad\qquad\qquad K_{rel,l}(1-\alpha) = \alpha^m \tag{1.14}$$

Here, with an increasing exponent n or m the friction of flow increases (component K_{rel} less than 1, 1 means no friction) which increase the pressure drop inside the bed.

1. INTRODUCTION

Other two-phase friction models have been considered by Lipinski [52], Reed [53], and Hu & Theofanous [54]. The classic approaches to formulation for existing dryout models, listed by some authors, is shown in Table (1.1). There, the corresponding exponents have been adjusted exclusively via the maximum steam superficial velocity at the occurrence of dryout.

Table 1.1: Classic formulations of relative permeability K_{rel} and passability η_{rel}

	$K_{l,rel}$	$\eta_{l,rel}$	$K_{g,rel}$	$\eta_{g,rel}$
Lipinski [52]	$(1-\alpha)^3$	$(1-\alpha)^3$	α^3	α^3
Reed [53]	$(1-\alpha)^3$	$(1-\alpha)^5$	α^5	α^5
Hu and Theofanous [54]	$(1-\alpha)^3$	$(1-\alpha)^6$	α^6	α^6

All these classical models do not explicitly take into account the interphase friction between steam and water and, therefore, provide unsatisfactory results for the pressure gradients and dryout heat flux values [43], especially for counter-current conditions with large particle diameters and small superficial gas velocities. The calculations based on the classical models of Lipinski [52]], Reed [53]] and Hu & Theofanous [54], without explicit consideration of the interphase friction term, show the inability of such models to reproduce the pressure drops (for both co- and counter-current conditions) inside debris beds as measured in experiments (see Schäfer et al. [43], Tutu et al. [55]). The model calculations for Hofmann's experiments [56] failed to reproduce the DHF values of the bottom-flooding condition with the classical model formulation used for top-flooding, i.e. without interfacial friction (see also Schmidt [6]). This leads to the conclusion that an interphase friction term needs to be included in the models in order to correctly predict the maximum dryout heat flux for both co- and counter-current flow conditions inside the bed. By introducing an interphase friction term F_i in the extended Erguns equations, Schulenberg & Müller [57] and Tung & Dhir [58] provided an improved approximation of the model calculations to predict the experimental results (see Eq. (1.15) and Eq. (1.16)).

$$\left(-\frac{dp_l}{dz}\right) = \rho_l g + \frac{\mu_l}{K K_{rel,l}} J_l + \frac{\rho_l}{\eta \eta_{rel,l}} J_l |J_l| - \frac{F_i}{1-\alpha} \tag{1.15}$$

$$\left(-\frac{dp_g}{dz}\right) = \rho_g g + \frac{\mu_g}{K K_{rel,g}} J_g + \frac{\rho_g}{\eta \eta_{rel,g}} J_g |J_g| - \frac{F_i}{\alpha} \tag{1.16}$$

Using adiabatic air/water experimental data, Schulenberg & Müller [57] modeled the interphase friction term. Maintaining the Reed's classical friction formulation [53]], they defined the interphase friction term (see Eq. (1.17)) based on relative permeabilities and

Table 1.2: Flow regime bounds

Bubbly flow	$0 < \alpha \leq \alpha_1 = 0.3$	$for\ \gamma < 0.29$
	$= 0.6(1 - \gamma)^2$	$for\ \gamma > 0.29$
Bubbly/slug flow transition regime	$\alpha_1 < \alpha \leq \alpha_2 = \pi/6 \approx 0.52$	
Slug flow	$\alpha_2 < \alpha \leq \alpha_3 = 0.6$	
Slug/annular transition regime	$\alpha_3 < \alpha \leq \alpha_4 = \pi 2^{0.5}/6 \approx 0.74$	
Annular flow	$\alpha_4 < \alpha \leq 1$	

passabilities in quadratic-dependence on the relative speed between the fluids and the solid.

$$F_i = W(\alpha)\frac{\rho_l K}{\eta\sigma}(\rho_l - \rho_g)g\left(\frac{J_g}{\alpha} - \frac{J_l}{(1 - \alpha)}\right)^2 \ with\ W(\alpha) = 350(1 - \alpha)^7\alpha \qquad (1.17)$$

Based on the visual observation of adiabatic experiments (air/water experiments), Tung & Dhir [58] derived friction formulations (particle-fluid friction and fluid interphase friction) for different flow regimes and transitions in a particle bed. Depending on the vapor content (void = α), three flow regimes (bubbly flow, slug flow, and annular flow regime) are identified in Table (1.2) (see also Figure (1.8)), where, in reference to bubbly flow, α is set to the ratio (γ) of the bubble diameter to the particle diameter. In between three distinct flow regimes, there exists a transition phase.

(a) Bubbly Flow $\alpha < 0.3$ (b) Slug Flow $\alpha < 0.6$ (c) Annular Flow $\alpha > 0.74$
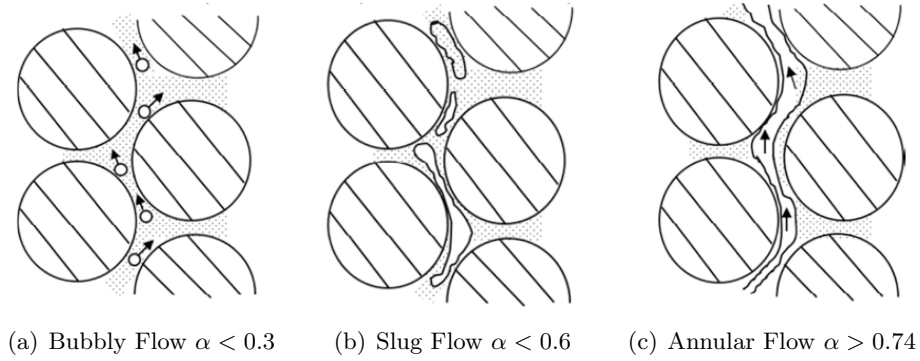
Figure 1.8: Sketches of different flow regimes for an adiabatic gas/liquid flow, Tung & Dhir [58].

The Tung & Dhir model calculations showed promising results when compared to the experimental results for larger particle diameters ($\geq 6\ mm$). However, Schmidt [6] remarked that, for smaller particles (dp $< 6\ mm$), the Tung & Dhir model shows significantly lower dryout heat flux values when compared to the measured dryout heat flux data.

1. INTRODUCTION

The further modifications to the original Tung & Dhir model suggest that, concerning smaller particles, the onset of annular flow is expected for relatively smaller void fractions than that predicted in the original Tung & Dhir model (Schmidt, [6]). For particles with smaller diameters, Schmidt modified the flow patterns with a relatively steep transition towards slug and annular flow regimes. The modifications made by Schmidt have been incorporated into the friction formulations in the MEWA-2D code, which is fundamentally based on the Tung & Dhir model. The MEWA-2D code has been further modified and developed by Rahman [59] at IKE University of Stuttgart.

Rahman [59] modified the flow patterns in the bubbly and slug flow regimes with a gradual decrease in void fraction as compared to the rapid decrease suggested by Schmidt. The experimental observations by Haga [60] and Stürzel [61] verify the modification made by Rahman. The experimental measurements by Haga [60] suggest that the annular flow regime is established at void fraction $\alpha = 0.32$ and 0.25 for $2\ mm$ and $1\ mm$ particles, respectively. Similarly, Stürzel [61] performed adiabatic air/water experiments to investigate different flow regimes with debris beds with different particle diameters. Stürzel's findings suggest that the onset of transition between slug and annular flow takes place at void fraction $\alpha = 0.6$, 0.55 and 0.48 for $10\ mm$, $7\ mm$, and $5\ mm$ particle, respectively. Rahman further modified the relative permeabilities and passabilities for vapor/particle and liquid/particle friction. The classical Tung & Dhir model predicts dryout heat flux too low for counter-current flow conditions (top-flooding), which may be caused by interfacial friction that is too high. Rahman [59] also introduced a reduction factor to the interfacial friction in the bubbly, slug, and annular flow regimes.

So far the experimental studies have mainly focused on the 1D flow conditions (1D top-/bottom-flooding) for both dryout and quenching experiments. In dryout experiments, the focus has been on the determination of maximum heat (dryout heat flux (DHF)) that can be removed from the particle beds under steady state boiling conditions. The studies of the pressure behavior under steady state boiling conditions, which is an important aspect of coolability of volumetrically heated particle beds, are also limited to mainly monodispersed particle beds of single sized particles. For quenching experiments primarily the quench behavior has been studied with water supply either from a water reservoir above the bed (1D top-flooding) or from the bottom of the bed under forced inflow conditions (1D bottom-flooding). Whereas in case of 1D bottom-flooding (open-downcomer) under hydrostatic head the inlet flowrate is strongly dependent on the pressure profile inside the particle bed.

1.3   Aim of Work

As mentioned above, the available experimental data on the coolability of debris beds have been mainly focused on monodispersed particle beds (uniform particle beds with particles of the same diameter) and one-dimensional flow conditions. However, debris bed resulting from a severe accident in a nuclear reactor may consist of particles of different shapes and diameters, leading to different bed porosities. Similarly the flow conditions inside such debris bed are more of a multidimensional nature. Therefore, this work aims to extend the available experimental data on coolability of particle beds by using more realistic particle configurations.

Additionally, improvements on coolability under different flow conditions are investigated, and thereby different downcomer configurations, such as an open downcomer (1D, top-/bottom-flooding) and a perforated downcomer (2D top-/bottom-/lateral-flooding), are applied. Both the multi-diameter particle beds (specifically the irregular particle bed) and the downcomer configurations aim at a more realistic experimental representation of the flow situation in a nuclear debris bed.

Given the importance of coolability of debris beds for improvements in severe accident management (SAM) strategies, the aim is to contribute to the existing understanding and knowledge of the coolability behavior of particle beds with a focus on multi-diameter particle beds, e.g. polydispersed particle bed (2 mm, 3 mm and 6 mm diameters) and irregular particle bed (a mixture of stainless steel balls (3 mm and 6 mm) and irregularly shaped Al_2O_3 particles). Hence, within the scope of this experimental work, it is intended to contribute to the existing experimental database, by providing pressure drop, dryout heat flux data, and the coolability of debris beds.

Chapter 2

Experimental Setup and Test Conditions

In this chapter an overview of the experiments performed, test conditions and boundary conditions is given. In order to perform the experimental tasks, the existing DEBRIS test facility has been modified. In addition, a test setup for a reduced bed height has been established for quenching experiments. A brief description of the existing DEBRIS test facility [45] and the modifications made for this study is provided in the following sections.

Figure 2.1 shows the schematic of the complete setup, including pressure vessel, piping and pumping system, storage tank and volumetric heating system. The main parts of the DEBRIS facility consist of a pressure vessel made of stainless steel whose walls can withstand pressure up to 40 *bar* and temperatures up to 300 °C. The pumping system, supported by a piping system and flow meter, allows experiments to be performed by feeding water to the crucible at the bottom (bottom-flooding) or at the top (top-flooding). The heating system is one of the most important parts of the test facility. To best simulate the decay heat generated by the radio-active particle bed (particle bed resulting from melt core and water interaction in the reactor pressure vessel), a volumetric inductive heating system is used. An oil-cooled 2-winding induction coil connected to an HF-generator is installed around the crucible (see Figure 2.1). The coil is connected with a HF-generator which operates at a frequency of 200 kHz and has a nominal power output of upto 140 kW.

2.1   Main Test Section

Main test section is mounted inside the pressure vessel and the induction coil is installed around the tubiular test section. The particle bed is placed inside the main test section
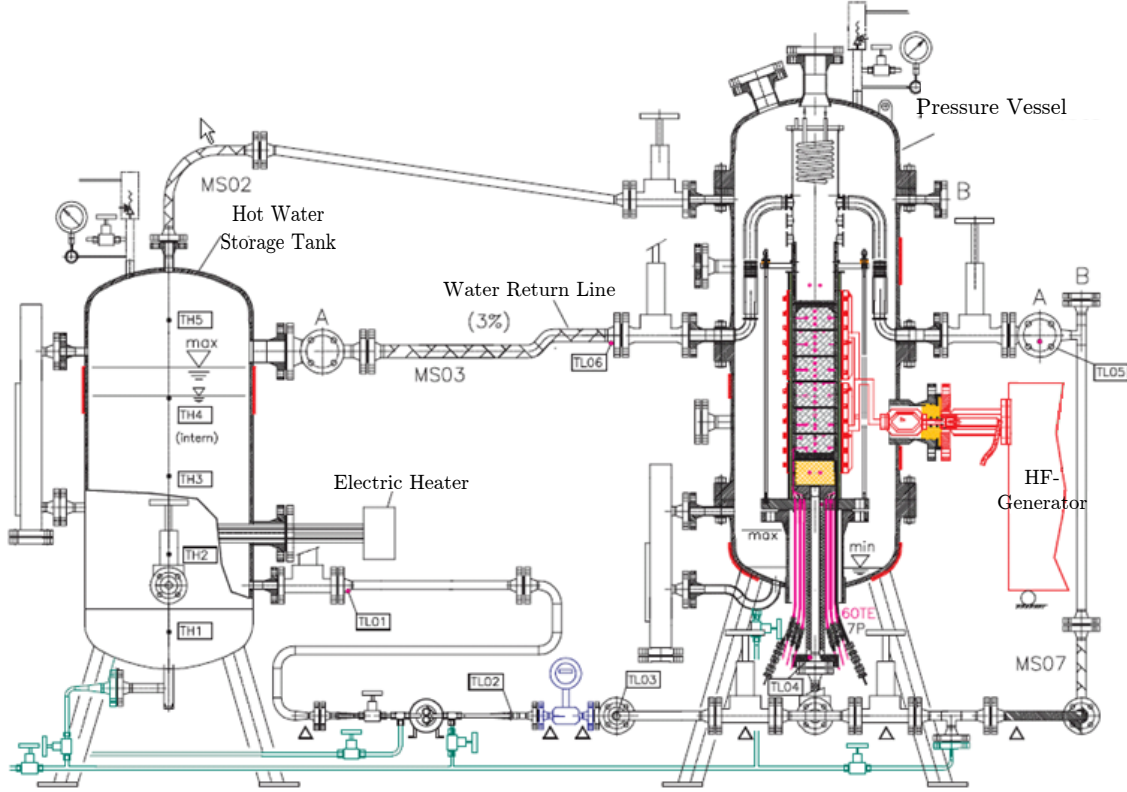
Figure 2.1: Schematic of the DEBRIS test facility [45].

and inductively heated. Depending upon different boundary conditions, e.g. experiments with and without downcomer configurations, change of particles, boiling and quenching experiments, the main test section had to be modified and at times rebuilt. Different types of test sections used for boiling/dryout and quenching experiments as well as the respective instrumentation are described below.

2.1.1 Boiling/Dryout Test Setup

The main test section (crucible) is mounted inside the pressure vessel. Based on different temperature boundary conditions, different crucibles (made of different materials) are used. For steady state boiling experiments, wherein, most of the time, the temperature remains at saturation temperature, the crucible itself is made of PTFE (Polytetrafluoroethylene/TEFLON), which has a melting temperature of 327 °C (see Figure 2.2(a)). The total height of the PTFE crucible is 870 mm and has an inner diameter of 125 mm. The same crucible is also used for dryout experiments wherein the temperature rises above saturation temperature but is maintained far below the temperature limit of PTFE (327 °C). To achieve bottom-flooding conditions under natural convection, a tubular down-

comer has been installed at the center of the test section, which, when opened, enables the water to flow into the bottom of the bed. The tubular downcomer made of PTFE has an inner diameter of 10 mm and an outer diameter of 18.5 mm. The installation of the downcomer required complete reconstruction of the existing setup, as all the thermocouples installed at the central position of the bed (see also Section 2.1.2) had to be repositioned.
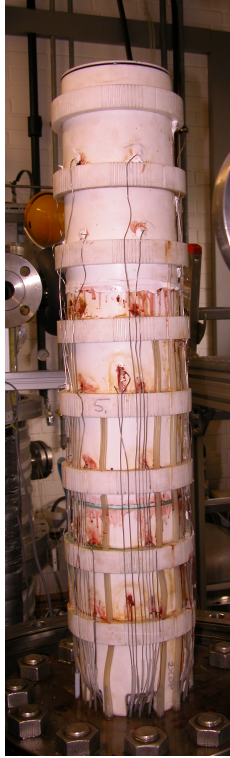
(a) PTFE crucible for boiling/dryout experiments

(b) Quartz glass crucible (L) and fire cement crucible (R) for quenching experiments

Figure 2.2: Crucibles used for boiling/dryout and quenching experiments.

Instrumentation of boiling/dryout test setup

During the boiling experiments, primarily measured are the pressure difference at different axial positions and temperatures at different axial and radial positions. For boiling/dryout experiments, the thermocouples come through the flange at the bottom and are inserted from the sides through the walls of the crucible at specific locations. The thermocouples measure the temperature in the voids between the particles, which are filled with liquid, vapor, or a mixture of both. In total there are 60 thermocouples (1 mm, Type N), of
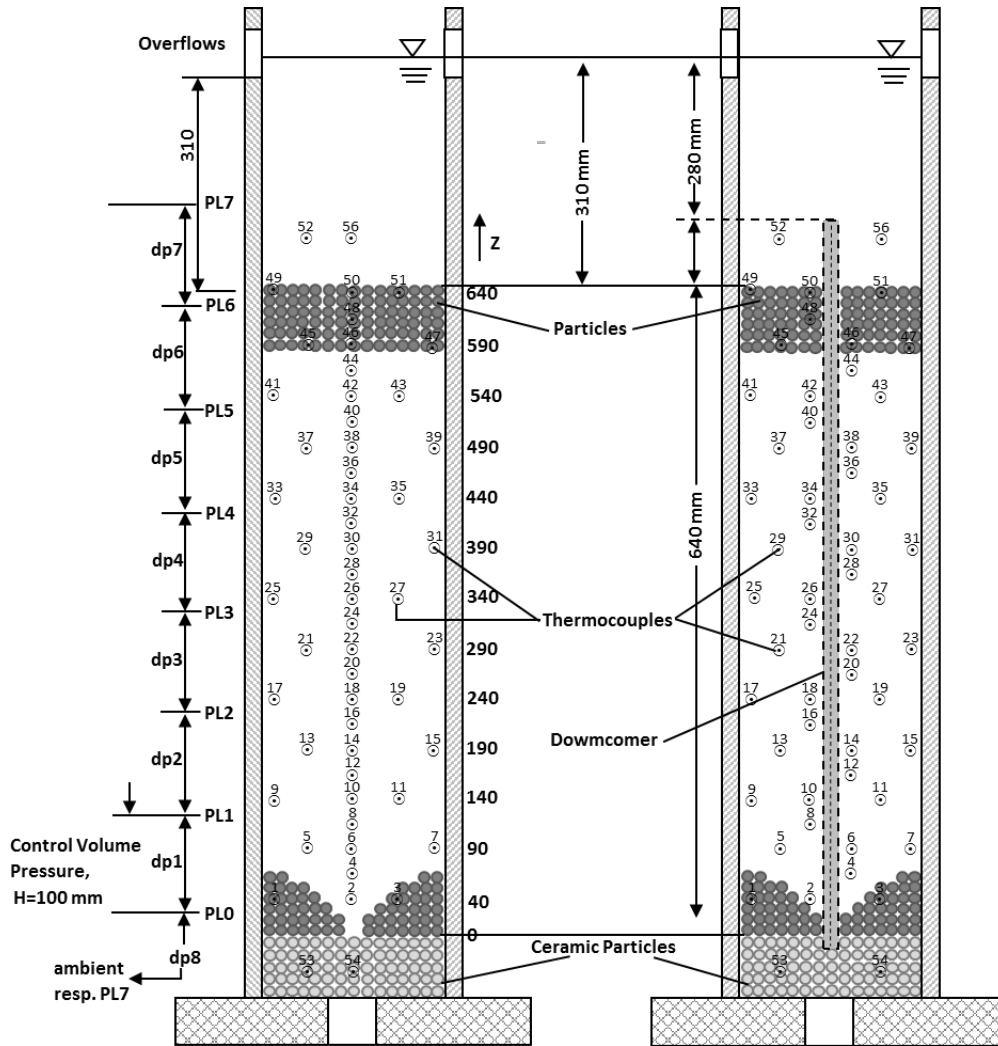
Figure 2.3: Instrumentation diagram of the main test section (boiling/dryout).

which 51 are located in the debris bed at 25 levels. The thermocouples are located at the following positions (see Figure 2.3):

- at 13 levels along the bed height, and at each level temperature is measured at three different radial locations: close to the crucible wall, at half radius, at the center of the particle bed

- in addition, at 12 extra levels in the center

- two thermocouples below the bed to measure water inlet temperature

- two thermocouples above the bed to measure the water outlet temperature

For pressure measurements during steady state boiling experiments, eight differential pressure transducers are used (100 *mbar*, class 0.1). The pressure taps are uniformly

distributed at 100 mm intervals along the bed height. Each of the pressure transducers measures the pressure difference between two specific levels, e.g. dp1 measures the pressure difference between the levels PL0 and PL1, and, similarly, the pressure transducers dp2-dp6 measure the pressure difference between levels PL1 and PL6. The pressure transducer dp7 measures the pressure difference between the uppermost level of the bed, PL6, and the water pool at level PL7. The pressure transducer dp8 is used for measuring the total pressure difference between levels PL0 and PL7. The exact position of the thermocouples and pressure taps can be seen in Figure 2.3.

2.1.2 Quenching Test Setup

The experimental parameters for quenching experiments are quite different than those for boiling/dryout experiments. The expected bed temperatures for quenching experiments were much higher than the melting point of PTFE (327°C). Due to the high initial overheat temperatures (e.g. 800°C) and high temperature transients in the flooding/quenching test series with dry beds, the PTFE test section from the boiling/dryout experiments is unsuitable for quenching experiments. The extreme thermomechanical conditions during the flooding led to the use of three different test sections for quenching experiments (see Figure 2.2(b)).

The first test section consisted of two different cylinders/tubes (inner and outer cylinders/tubes) made of two different materials. The inner cylinder consisted of bonded ceramic rings (alumina fibers > 98% Al_2O_3, 70% porosity, temperature resistant up to 1200°C) with a height of 50 mm, an inner diameter of 150 mm, and an outer diameter of 175 mm. Due to the high wall porosity and mechanical sensitivity of the ceramic material, an external tube made of quartz glass was mounted around the inner tube. The external quartz glass tube had an overall height of 870 mm, an inner diameter of 200 mm, and a wall thickness of 3.5 mm. The annular gap between the inner ceramic tube and the outer quartz glass tube was lined with soft ceramic mats and served for lateral thermocouple positioning. Over the course of the quenching experiments, the inner ceramic tube showed a great tendency, induced by thermo-mechanical forces, to crack or even break, which led to an undesired outflow of coolant water into the annular gap between the inner ceramic and outer quartz glass tubes. Due to the problems recognized during the use of the first type of test section, the second test section consisted only of a quartz glass (thermally stable up to temperatures of 1000°C) tube with an inner diameter of 150 mm and a wall thickness of 5 mm, while different heights of 500 mm and 870 mm were used.

Despite the use of thermally stable materials for test sections, over the course of the quenching experiments, multiple defects (such as leaks, glass cracks and broken glass

Figure 2.4: Broken quartz glass test section.

etc.) appeared in the test section. In some cases, the test sections failed to sustain the temperature increase and no useful data were generated. The very time-consuming and costly repairs or replacement measures of such test section variations ultimately led to the establishment of a third type of test section - a hollow cylinder made from refractory cement material with an inner diameter 150 mm, medium wall thickness of 20 mm, and a container height of 1000 mm. An essential advantage of this type of test section is the option for low-cost and relatively simple in-house production (casting and curing the hollow cylinder was done locally in the lab) for replacement demand. The thermocouples used for temperature measurements had to be repositioned, and, because no pressure measurements were carried out for the quenching experiments, all the pressure transducers were also removed. This resulted in the reconstruction and re-instrumentation of the main test section. Over the course of the quenching experiments, a few limitations were observed, and, for a certain number of experiments, a new test section made of fire cement was used.

In the quenching experiments, the particle bed was heated to higher, predefined temperatures. During the heat-up phase of the quenching experiments, the quartz glass test section cracked and, in some cases, even broke completely (see Figure 2.4).

Later in the experiments, it was also observed that the behavior of the quartz glass test section was different for different particle beds. Compared to an irregular particle bed (a mixture of irregularly shaped Al_2O_3 and stainless steel spheres, see also Section 2.2), for a polydispersed particle bed (a mixture of stainless steel spheres, see also Section 2.2), the

test section cracked or broke at relatively higher bed temperatures. In order to understand the different bed behavior during the heat-up phase of the quenching experiments, it is important to understand the bed characteristics, e.g. the shape of the particles, surface roughness, and particle-size distribution. In the case of an irregular particle bed (with a particle-size range of 2-10 mm, see also Section 2.2), the smaller particles tend to fill the void between the larger particles. At the same time, the irregular shapes of the particles also lead to increased friction between the particles. Therefore, as compared to experiments with polydispersed particle bed (with a particle size range of 2-6 mm), the experiments with irregular particle bed resulted in breakage of the test sections at lower temperatures. There, the increase in bed temperature, the associated thermal expansion of the particles, the particle shape, and the size distribution played a key role in determining the test section behavior.

2.1.2.1 Instrumentation of quenching test setup

For transient quenching experiments, no pressure measurements are carried out, hence no pressure transducer is installed (see Figure 2.5). Whereas, for temperature measurements the same number of thermocouples, as for boiling experiments, is used. As mentioned in the preceding section, different type of test section is used for quenching experiments which results in reconfiguration of the thermocouples (see Section 2.1.1). In this case the thermocouples come through the flange and are placed directly into the particle bed in a vertical direction at defined axial and radial positions. The overall measurement position of the thermocouples is same as used for boiling/dryout experiments (see also Section 2.1.1).

2.1.2.2 Quenching Test Setup with Reduced Bed Height

The unforeseeable technical difficulties resulted in the damage to the main test section which led to expensive repairs and excessive time delays. In order to avoid further delays and continue with the quenching experiments, it was decided to conduct the quenching experiments with a test section of reduced height [62]. On one hand, due to the constructive and electrical adjustment to the existing inductive coil assembly, the small test section could not be installed in the existing DEBRIS test setup. On the other hand, to better detect the quench front progression in the near wall regions, the need for increased thermocouple density in the near wall regions was realized. Installing more thermocouples to the existing DEBRIS setup would have meant an extension of the data acquisition system and very elaborate design change for the thermocouples to pass through the pressure vessel, which due to cost and time constraints was also not possible. Therefore it was
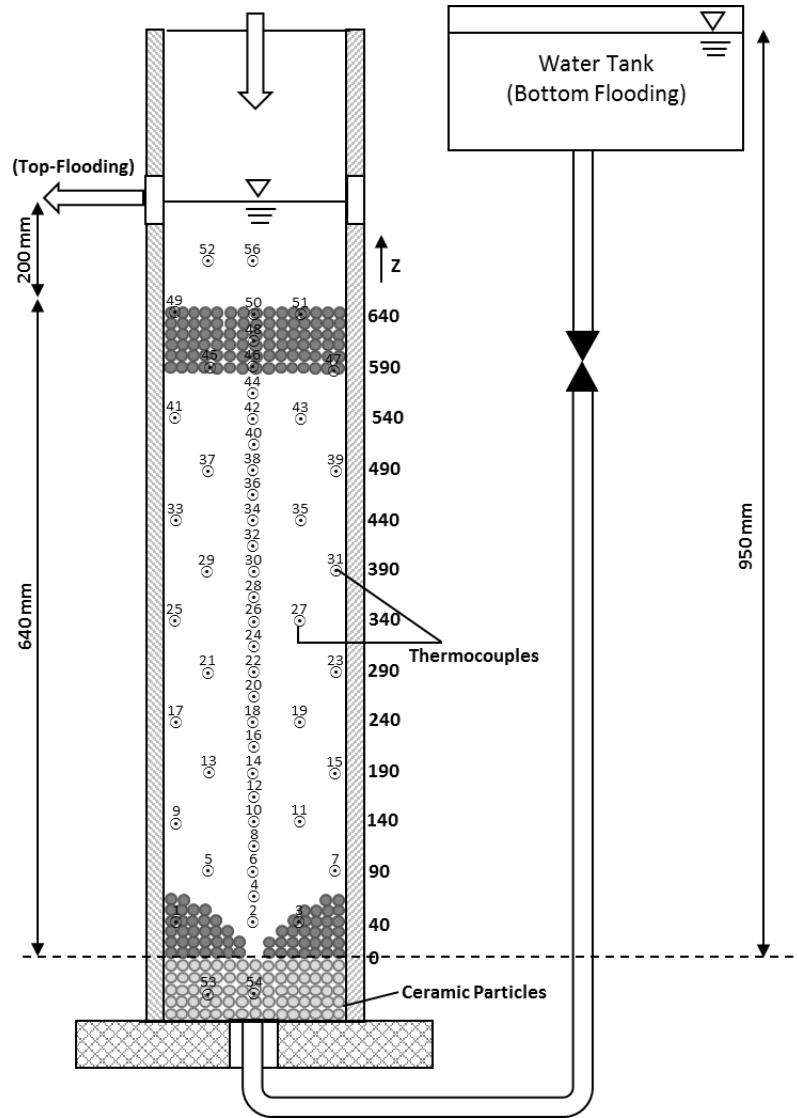
Figure 2.5: Instrumentation diagram of the main test section (quenching).

decided to use a complete separate setup with reduced test section height (see also Section 2.4).

The fundamental conceptual requirements of the new test setup, i.e. volumetric inductive heating of the bed, possibility of flooding from below (bottom-flooding) and from above (top-flooding), correspond to those of DEBRIS test setup. As in the case of DEBRIS test facility no pressure measuring device is installed because the test setup is exclusively designed for quenching tests. Differences exist in the measurement instrumentation (modified arrangement of the temperature measurement points in the bed, in particular more measuring points in the near wall regions) and of course in the height of the particle bed.

2. EXPERIMENTAL SETUP AND TEST CONDITIONS

Figure 2.6 shows a cut section through the setup with surrounding inductive coil. The stainless-steel base plate is used to accommodate the main test section and for axial guidance of the thermocouples in the bed. The main test section consists of a quartz glass tube (internal diameter 150 mm, length 300 mm, wall thickness 5 mm), which in an extended version is also used in the DEBRIS test setup. Using threaded rods the test section is fixed between the base plate and the upper stainless steel plates. Two PTFE rings with grooves for O-rings are simultaneously used on the upper and lower regions of the quartz glass tube for radial and axial sealing. On the upper plate a connector ring is welded to the flange which is used to mount the steam condensor. The heating system consists of a frequency generator and a spiral water cooled copper induction coil. The frequency generator operates at a frequency of 200 kHz and has a nominal output of 20 kW.
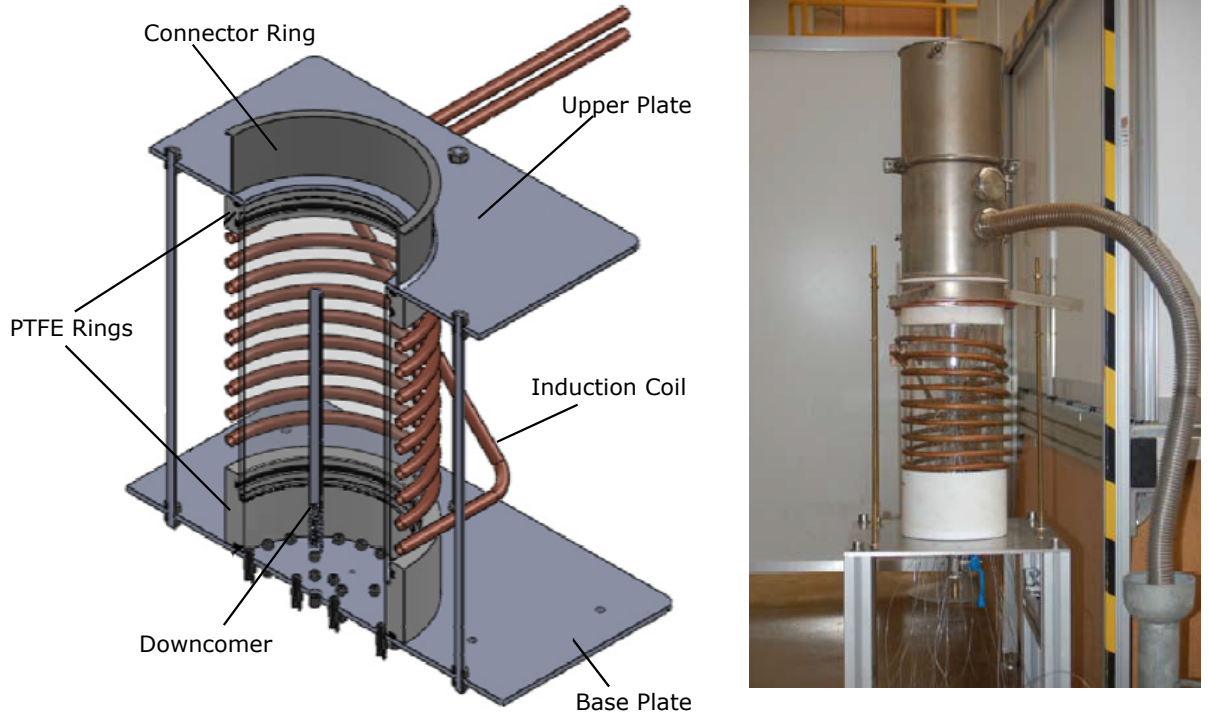
Figure 2.6: New test setup with reduced height [62].

The main test section is made of quartz glass crucible of height 300 mm. The particles are filled inside the quartz glass crucible to make a bed height of 200 mm. Figure 2.7 shows the schematic instrumentation of the test section. In total 36 (1 mm, Type N) thermocouples for temperature measurements are installed (see Figure 2.7). In order to investigate the bypass effects the thermocouple density is increased in the near-wall regions (see Figure 2.7). Along the bed height at 3 main levels (level 1-3) at a distance of 80 mm
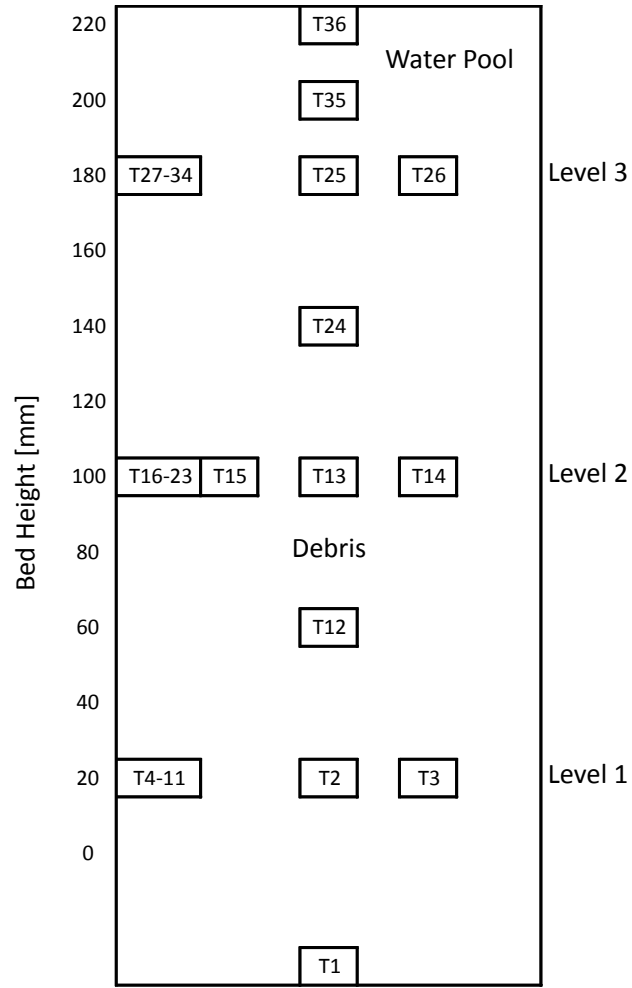
Figure 2.7: Layout of thermocouples for DEBRIS test setup with reduced height.

each, 24 evenly distributed thermocouples (T4-11, T16-23, T27-34) are installed on the periphery of the bed. One thermocouple each is installed below (T1, see Figure 2.7) and above (T36, see Figure 2.7) the bed to measure the inlet and outlet temperature of the water. The bed is volumetrically heated using magnetic induction heating system.

2.2   Particle Bed Types

For boiling, dryout, and quenching experiments, two different bed types have been used for the current test series (see also Table 2.1 and Table 2.2): Polydispersed particle bed (PDB) and Irregular particle bed (IPB). The polydispersed particle bed is composed of a mixture of pre-oxidized stainless steel balls of three different sizes - 2 mm, 3 mm, and 6 mm - mixed at a ratio of 20%, 30%, and 50% by weight, respectively (see Figure 2.8(a)). The measured porosity ε of the polydispersed particle bed is 0.37. A bed height of 640 mm is used for all the test series with the polydispersed particle bed.

The irregular particle bed consists of a mixture of irregular aluminum oxide particles with equivalent diameters of 2-10 mm and stainless steel balls of 3 mm and 6 mm diameters. The irregular alumina particles are the fragmentation particles resulting from the PREMIX experiments carried out at the Research Centre (Kaiser et al. [28]) (see also Figure 2.8(b)). These particles are mainly composed of Al_2O_3, thus the inductive heating generation is very low, as will be discussed in Section 3.1.1. In order to provide enough heating power to the particle beds, additional 6 mm and 3 mm steel spheres are mixed with the irregularly shaped particles. The spheres comprise about 44.1% of the volume of the bed and 68.5% of its weight. A bed of height of 650 mm and a diameter of 125 mm are maintained in all the experiments with IPB. The measured porosity of the bed is $\varepsilon = 0.38$. At the bottom of the bed, a thin layer of ceramic particles of 4 mm diameter (see Figure 2.8(c)) is used to avoid direct thermal contact of the particle bed to the aluminum plate on which the test section is built.

2.3   Test Conditions

The experiments carried out during this study have mainly dealt with two aspects of particle beds coolability: long-term coolability and the cool-down behavior of the dry hot particle beds. The results have been categorized into two main categories as discussed below:

Table 2.1: Polydispersed particle bed composition

Particles	Material	Diameter	Weight	Wt.	Vol.
[-]	[-]	[mm]	[kg]	[%]	[%]
Spheres	Pre-oxidized Steel	6	30	50	50
Spheres	Pre-oxidized Steel	3	18	30	30
Spheres	Pre-oxidized Steel	2	12	20	20
	Total Weight		60		

Table 2.2: Irregular particle bed composition

Particles	Material	Diameter	Weight	Wt.	Vol.
[-]	[-]	[mm]	[kg]	[%]	[%]
Spheres	Pre-oxidized Steel	6	11.4	43.7	28.1
Spheres	Pre-oxidized Steel	3	6.4	24.8	16
Irregular	Al_2O_3	>5-10	5.4	20.8	38.6
Irregular	Al_2O_3	>2-5	2.8	10.7	17.3
			26		

(a) Stainless Steel Spheres   (b) Irregular PREMIX Particles

(c) Ceramic Particles
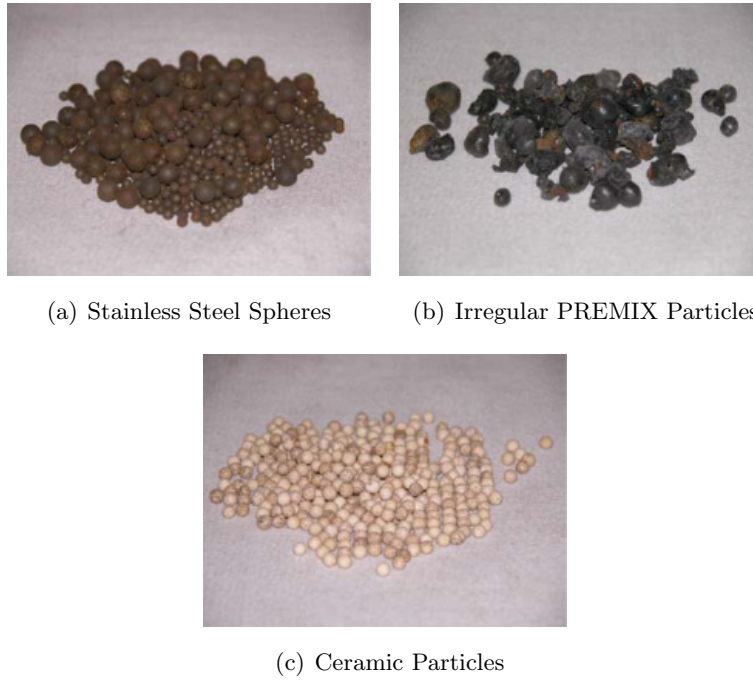
Figure 2.8: Different particles used in experiments.

2.3.1 Boiling/Dryout Experiments

The boiling/dryout experiments have been carried out at three different system pressures (1, 3, and 5 *bar*) to understand the long-term coolability of the particle bed. The term "long-term coolability" defines the coolable state of the particle bed, where heat is transported out of the particle bed for an extended duration of time and the temperatures are maintained at saturation. In experiments, the volumetric heating power applied to the saturated particle bed is increased stepwise; steady states are reached before changing steps. At a steady state, the respective pressure drop is measured for different bed sections along the bed height, which helps understanding of the friction behavior between different phases. The measured pressure drop data mainly act as a tool for understanding

the friction behavior of the beds and are used for the verification of the friction laws that are included in the existing dryout models.

Dryout experiments provide data about dryout heat flux. Dryout heat flux is the maximum amount of heat that can be transported out of the bed without the occurrence of a dry zone inside the bed. As mentioned earlier, the volumetric heating power is increased stepwise until a dry zone, e.g. a temperature increase above saturation indicated by one or more thermocouples, is detected.

2.3.2 Quenching Experiments

In the current study, the quenching experiments are only performed at atmospheric pressure. The aim of the quenching experiments is to study the cool-down behavior of the dry hot particle bed. The intention is to investigate the inflow of sub-cooled water into the super-heated particle beds and the progression of the respective quench front. The time needed for different super-heated beds to reach the saturation temperature has also been discussed.

2.4 Flow Conditions

Depending upon the direction of the coolant water, three main flow conditions have been realized in this work. In systematic order, the flow conditions are:

- **Counter-current Flow:** Under steady boiling conditions with no additional water supply to the bottom of the bed, the evaporated water must be replaced with water from the overlying water pool so that bed dryout can be avoided. The coolant water ingresses downwards into the bed while the generated steam moves upwards. Hence a counter-current flow is established between the coolant water and the steam (see also flow condition (I)).

- **Co-current Flow:** In this flow pattern, the water is fed into the bottom regions of the bed. Both the steam and the coolant water mainly flow in the same direction, and a co-current flow is established inside the bed. For experiments with tubular downcomer configurations, e.g. an external downcomer or a downcomer installed in the center of the bed (see also flow conditions (II) and (III)), both the co- and counter-current flow exist inside the bed.

- **Lateral Flow:** The installation of a perforated downcomer in the center of the particle bed provides the lateral flow of coolant water into the bed (see also flow condition (IV)).

Under co- and/or counter-current flow conditions, the flow inside the particle bed is also categorized as having one-dimensional (1D) flow conditions. In the case of a real particle beds, the flow is more of a multidimensional nature. Therefore, the lateral flow in combination with the axial flow leads to a two-dimensional (2D) flow condition, which is closer to the flow in a nuclear particle bed. A brief description of different flow conditions adopted for different boiling/dryout and quenching experiments are outlined below (also see Table 2.3).

(I) *1D top-flooding (water supply from the top)*

For boiling/dryout experiments, the water is supplied from an overlying water pool of a constant height of 310 mm above the bed (see Figure 2.2(a)). Under steady-state boiling conditions, the steam generated inside the bed tends to escape upwards, while the water under gravity tends to flow downwards (top to bottom also is called "top-flooding"). This leads to a 1D counter-current flow condition inside the bed. In quenching experiments, the hot dry particle bed is flooded with water from the top. Within a short interval of time, due to a high inlet rate, a water pool 200 mm high is built on top of the bed and is maintained during quenching. For 1D top-flooding flow conditions, two different sets of experiments were performed: *(a) top-flooding without a downcomer (b) top-flooding with a closed downcomer.*

Initially, the experiments were carried out without using a downcomer. Later on, for different downcomer configurations, a PTFE tube (length 660 mm, outer diameter 19 mm, inner diameter 10 mm) is installed in the center of the particle bed along the bed height. In these experiments, the downcomer is kept closed and no water can flow into it. Hence the only water supply to the particle bed is from the overlying water pool, resulting in a 1D top-flooding condition. The experiments carried out for a closed downcomer configuration are mainly calibration experiments, which not only are focused on studying effects induced by the presence of a central downcomer inside the particle bed, but also contribute to the stepwise change towards 2D experiments.

(II) *1D bottom-flooding (water supply from the bottom via pump (forced inflow/via water tank under hydrostatic head)*

By using a pump, the coolant water is supplied to the hot particle beds at fixed inflow rates. The coolant water and the steam generated inside the bed both flow upwards, forming a 1D co-current flow condition. Furthermore in the quenching test series, water, under the hydrostatic head, is supplied from a water tank maintained at a height of 950 mm from the bottom of the bed.

(III) *1D top-/bottom-flooding (water supply from the top and bottom via internal/external downcomer, natural circulation)*

The water is supplied from the overlying water pool above the bed (i.e. top-flooding), which is also supplied to the bottom of the particle bed via an internal downcomer (i.e. natural convection). For boiling experiments, in another variation of this flow condition, the water is supplied to the bottom of the particle bed via an external downcomer. The external downcomer is connected to the overflow of the overlying water pool above the bed. This flow condition represents a combination of flow condition (I) and flow condition (II). In this case, both co- and counter-current flows are established inside the bed. Both for boiling and quenching experiments, the flow is of a 1D nature.

(IV) *2D top-/bottom-/lateral-flooding (water supply from the top with a perforated downcomer)*
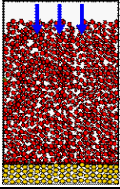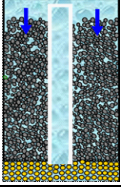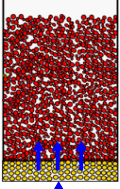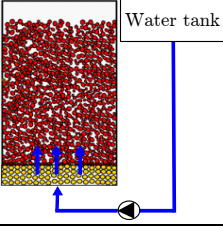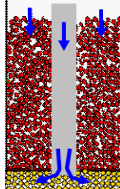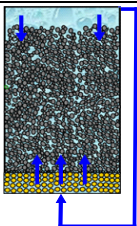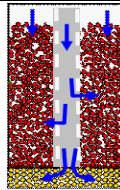
In this flow condition, a perforated downcomer (i.e. a porous downcomer, for boiling and quenching experiments, made of PTFE and an aluminum-tube 660 mm long, with an outer/inner diameter of 20 mm/10 mm, respectively, and a pore area/pipe area ratio of 0.9) is installed in the center of the particle bed. In addition to the top-/bottom-flooding, the perforated downcomer provides lateral water flow in the radial direction. Therefore, due to the simultaneous presence of co-/counter- as well as lateral-water flow, a 2D flow condition is expected inside the particle bed.

2.5   Test Matrix

This section provides an outline of the experiments carried out in this experimental investigation. An overview of the boiling/dryout and quenching experiments is given in Tables 2.4, 2.5 and 2.6 respectively. The experiments are categorized with respect to the bed types (PDB and IPB, see Section 2.2) and the flow conditions (I) - (IV) (see Section 2.4). All experiments are performed at ambient pressure, while boiling/dryout experiments are also carried out at higher system pressures (3 and 5 bar). In both boiling/dryout and quenching experiments, for flow condition (II) (bottom-flooding with water supply from the bottom via pump), another parameter varied was the coolant inlet flow rate. Here the inlet flow rate is defined as liquid superficial velocity J_l^0 which is calculated from the measured volumetric flow rate of the liquid.

Table 2.3: Different Flow Conditions

Flow Conditions		Boiling/Dryout Experiments	Quenching Experiments
(I)	1D top-flooding	without downcomer	
		closed downcomer	
(II)	1D bottom-flooding	without downcomer forced flow	
		external downcomer hydrostatic head	
(III)	1D top-/bottom-flooding	internal open downcomer natural circulation	
		external downcomer natural circulation	
(IV)	2D top-/bottom-/lateral-flooding	perforated downcomer	

Table 2.4: Polydispersed particle bed: overview of the test matrix for boiling/dryout experiments for defined flow conditions

		Polydispersed Particle Bed			
		(I)	(II)	(III)	(IV)
Flow Conditions		closed DC	external DC	open DC	perforated DC
		J_l^0 =0 mm/s	hydrostatic head		
System Pressure [bar]	1	✓	✓	✓	✓
	3	✓	n.p.[a]	✓	✓
	5	✓	n.p.[a]	✓	✓

[a] Experiments not performed in this study (see also Schäfer [45]).

Table 2.5: Irregular particle bed: overview of the test matrix for boiling/dryout experiments for defined flow conditions

		Irregular Particle Bed				
		(I)	(II)	(III)	(III)	(IV)
Flow Conditions		without DC	without DC	open DC	external DC	perforated DC
		J_l^0 = 0 mm/s	via pump	natural circulation		
System Pressure [bar]	1	✓	0.5 / 0.7 / 1.3 / 2.9 / 7.1	✓	n.u.d.[1]	✓
	3	✓	0.3 / 0.6 / 2.8	✓	n.u.d.[1]	n.a.[2]
	5	✓	0.3 / 0.6 / 2.7	✓	n.u.d.[1]	n.a.[2]

[1] No useful data availabe due to the unstable flow conditions (see Section 3.2).

[2] Experimental data not available due to the limitations of the heating setup.

Table 2.6: Overview of the test matrix for quenching experiments for defined flow conditions

Polydispersed Particle Bed

Flow Conditions (I) (1D top-flooding, water from top) - (Fire cement/Ceramic test section)

	T_{avg} [°C]	T_{center} [°C]	T_{max} [°C]
1	260	289	318
2	268	287	338
3	276	285	360
4	324	354	432
5	323	374	438
6	437	484	534
7	451	494	548
8	474	531	660
9	541	583	653
10	627	680	747
11	651	714	799

Flow Condition (II) (1D bottom-flooding, water pumped into the bed) - (Fire cement/Ceramic test section)

	J_l^0 mm/s	T_{avg} [°C]	T_{center} [°C]	T_{max} [°C]
1	1.9	339	339	445
2	2.3	595	663	745

(1D bottom-flooding, water supplied into the bed via water tank under hydrostatic head) - (Fire cement/Ceramic test section)

	T_{avg} [°C]	T_{center} [°C]	T_{max} [°C]
1	326	326	447
2	387	384	546
3	513	515	631
4	571	624	725

(Flow Condition (III) (1D top-/bottom-flooding, water pool + central downcomer) - (Quartz glass test section)

	T_{avg} [°C]	T_{center} [°C]	T_{max} [°C]
1	244	239	333
2	256	251	340
3	323	333	447
4	345	380	454
5	349	388	457
6	346	379	459

Continuation of Table 2.6

Flow Condition (IV) (2D top-/bottom-/lateral-flooding, water pool + perforated central downcomer) - (Fire cement test section)

	T_{avg} [°C]	T_{center} [°C]	T_{max} [°C]
1	230	308	396
2	251	339	422
3	594	633	761

Irregular Particle Bed

Flow Condition (I) (1D top-flooding, water from top) - (Quartz glass test section)

	T_{avg} [°C]	T_{center} [°C]	T_{max} [°C]
1	355	365	530
2	397	411	492
3	475	493	755

Flow Condition (II) (1D bottom-flooding, water pumped into the bed) - (Fire cement test section)

	J_l^0 mm/s	T_{avg} [°C]	T_{center} [°C]	T_{max} [°C]
1	2.3	322	383	416
2	2.3	415	476	527

(1D bottom-flooding, water supplied into the bed via water tank under hydrostatic head) - (Fire cement/Ceramic test section)

	T_{avg} [°C]	T_{center} [°C]	T_{max} [°C]
1	261	291	336
2	330	385	442
3	418	478	530

Flow Condition (III) (top-/bottom-flooding, water pool + central downcomer) - (Quartz glass test section)

	T_{avg} [°C]	T_{center} [°C]	T_{max} [°C]
1	272	317	394
2	308	380	451

Flow Condition (IV) (top-/bottom-/lateral-flooding, water pool + perforated central downcomer) - (Fire cement test section)

	T_{avg} [°C]	T_{center} [°C]	T_{max} [°C]
1	279	347	439
2	292	362	448

Chapter 3

Experimental Results

The experimental results are described in terms of three important cooling aspects of debris coolability, boiling behavior, dryout behavior and the quenching behavior. The aim of the boiling experiments is to study pressure drop and temperature behavior of the debris bed under saturation conditions without the formation of any dry zone inside the bed. The formation of a dry zone marks the onset of dryout of the debris bed. The dryout experiments are mainly the study of the long-term coolability of the debris bed i.e. how much heat can be removed from a saturated debris bed without formation of any dry zone inside the debris bed. The quenching experiments are related to the study of cool-down behavior of dry hot debris bed (i.e. particle bed with zero liquid saturation and above saturation temperatures). The following chapter discusses the experimental results in terms of different cooling aspeects (boiling, dryout and quenching) for different test conditions (see also Chapter 2).

3.1 Calibration Experiments

In order to understand the chracteristics (e.g. volumetric heat generation rate and effective particle diameter) of particle beds, calibration experiments were carried out as discussed below.

3.1.1 Heat-Input Calibration

The heat input calibration experiments provide the data for volumetric heat generation by different particle beds. At different heating levels (induction power regulated by setting the generator level) the saturated particle bed is electro-magnetically heated to temperatures below saturation temperature and the respective increase in temperature is recorded by the thermocouples installed at different positions inside the bed. Based on the adiabatic

3. EXPERIMENTAL RESULTS
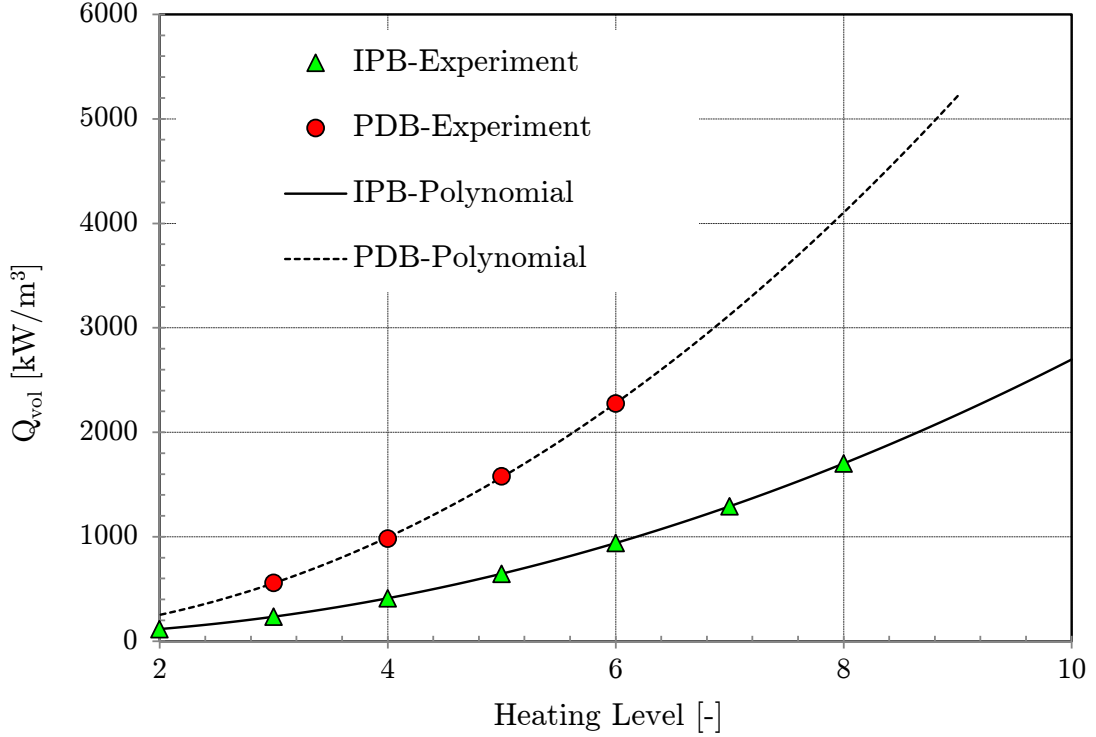
Figure 3.1: Volumetric heat generation by different particle beds, PDB and IPB, at different heating levels.

assumption, at certain generator level, the average temperature gradient is used to estimate the heat generation by the particle bed. Assuming the downward heat loss through the insulator (layer of ceramic balls below the bed) and lateral heat loss through the wall of the crucible negligible, the volumetric heat generation by polydispersed and irregular particle bed can be calculated by the equations Eq. 3.1 and Eq. 3.2 where ε is the measured porosity of the particle bed, $(\rho_w, \rho_s, \rho_a, C_p^w, C_p^s, C_p^a)$ are the densities and specific heats of water (index w), stainless-steel balls (index s) and Al_2O_3 (index a) respectively.

$$Q_{vol} = [\varepsilon\rho_w C_p^w + (1-\varepsilon)\rho_s C_p^s]dT/dt \tag{3.1}$$

$$Q_{vol} = [\varepsilon\rho_w C_p^w + 0.69(1-\varepsilon)\rho_s C_p^s + 0.31(1-\varepsilon)\rho_a C_p^a]dT/dt \tag{3.2}$$

Figure 3.1 presents the average volumetric heat generation for the total bed height for different particle beds at different generator levels. The heat generated inside the particle bed depends on the generator level, particle diameter and the inductive coupling efficiency of the material. The weak coupling effect of irregular PREMIX (Al_2O_3) particles mainly

contributes to the poor heat generation inside irregular particle bed. For a generator level 5, the heat generated by polydispersed particle bed is approximately 2.5 times higher than the heat generated by irregular particle bed (see Figure 3.1). The overall heating of the irregular particle bed is a result of direct heating from induction as well as indirect heating via heat conduction from stainless-steel spheres mixed with irregular Al_2O_3 particles.

The axial heat generation profile, averaged at different controlled volumes along the bed height, shows some local in-homogeneities (see Figure 3.2(a)). Some local heat losses in top and bottom regions of the heating coil have also been observed. In addition the poly-dispersed nature of particle beds and different particle materials (stainless-steel spheres and Al_2O_3 irregular particles) with different coupling efficiencies also contribute to local in-homogeneities in heat generation. Even though axial heat-generation profiles of different experiments with same bed configurations, performed on different dates, showed some local discrepancies but the integral heat flux over the whole bed height at different generator levels shows good reproduceability behavior(see Figure 3.2(b)). The effective
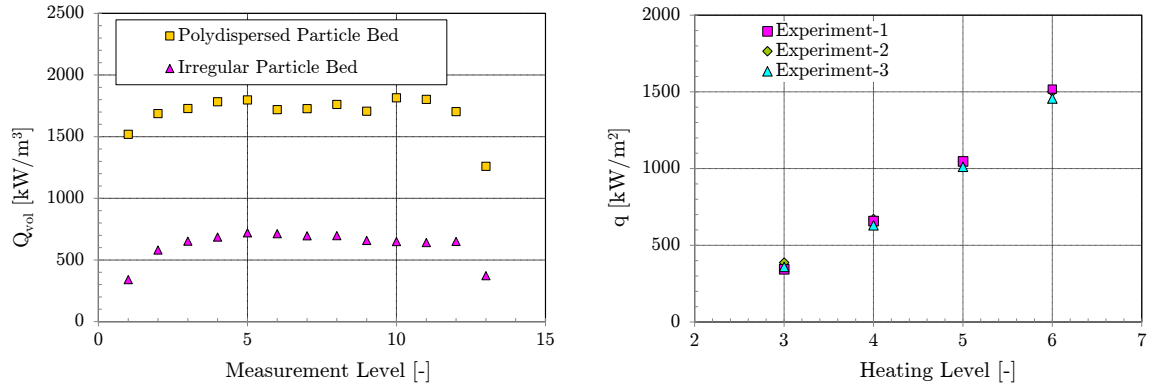
(a) Average values of volumetric heat generated by different particle beds(PDB) and (IPB), at 13 measurement levels along the bed height, heating level 5.

(b) Comparison of integral heat flux for different experiments for PDB.

Figure 3.2: Heat generation behavior of different particle beds, PDB and IPB.

heat flux q is defined as the integral heat generation of the bed and is given by Eq. 3.3 where (h) is the total height of the bed.

$$q = Q_{vol}h \tag{3.3}$$

The calculated average heat flux data as well as the fitted curve for different generator levels (induction power) is shown in Figure 3.3. The heat input curve was further used to calculate the gas superficial velocity J_g.
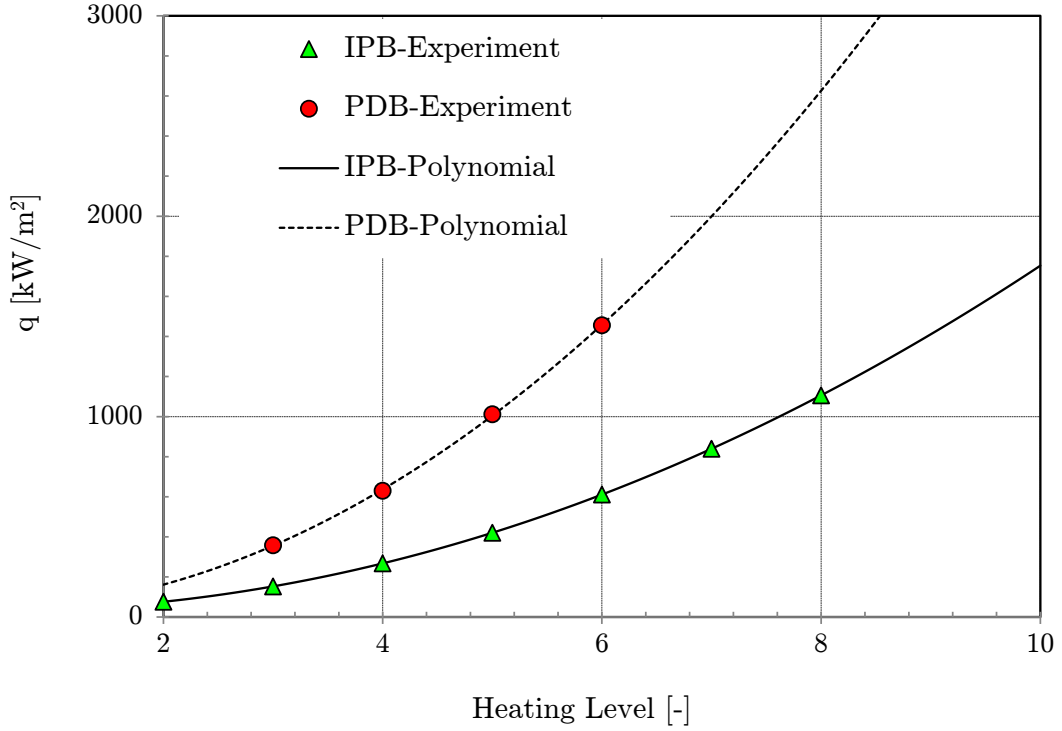
Figure 3.3: Heat flux generation in different particle beds, PDB and IPB, at different heating levels.

3.1.2 Single-Phase Pressure Drop (Particle Bed Characterization)

In terms of friction models the effective particle diameter d_e along with porosity ε (ratio of the hollow space in a controlled volume $= V_{hollow}/V_{total}$) of the bed plays an important role to calculate the flow friction. In order to understand the frictional pressure drop characteristics and to approximate the effective particle diameter of the bed, adiabatic single-phase pressure drop experiments have been carried out. Using water as the working fluid the pressure drops are measured at different liquid superficial velocities (J_l^0) (see Figure 3.4). For a given water inflow velocity, the pressure drops are determined at six measurement positions, dp1 to dp6 (see Figure 2.3). The average experimental data for pressure gradients of polydispersed particle bed and of irregular particle bed are shown in the Figure 3.4. The measured pressure gradients for irregular particle bed are smaller than the ones for polydispersed particle bed. Ergun's empirical correlation has been widely accepted to calculate the pressure drop in single phase flow through porous beds

$$-\frac{dp}{dz} = \frac{150(1-\varepsilon)^2\mu}{d_e^2\varepsilon^3}J + \frac{1.75(1-\varepsilon)\rho}{d_e\varepsilon^3}J^2 \tag{3.4}$$
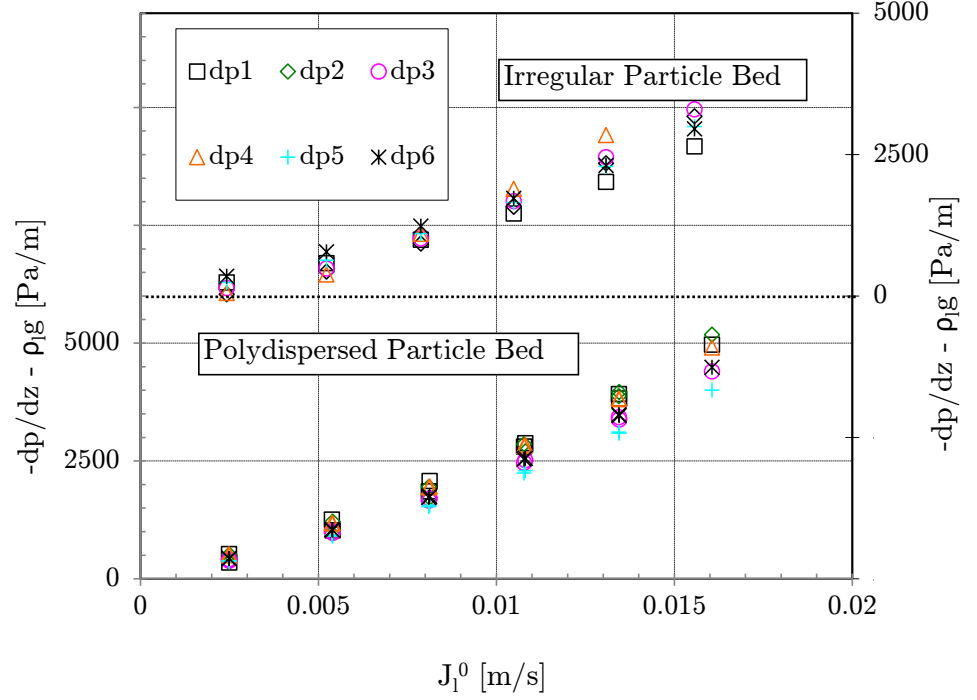
Figure 3.4: Single-phase pressure gradients for different particle beds, PDB and IPB, measured at six different bed sections (dp1-dp6) along the bed height at different superficial inflow velocities.

where dp/dz is the pressure gradient along the bed height, μ the dynamic viscosity of fluid, ρ the density of the fluid, J the superficial velocity of fluid, ε the porosity of the particle bed and d_e is defined as the effective particle diameter. The Eq. 3.4 can also be defined as the sum of inertial and viscous forces (see Eq. 3.5)

$$\left(-\frac{dp}{dz}\right)_{tot} = \left(-\frac{dp}{dz}\right)_{grav} + \left(-\frac{dp}{dz}\right)_{F} \qquad (3.5)$$

$(-\frac{dp}{dz})_{grav} = \rho g$ is the pressure drop caused by hydrostatic head. Ergun's correlation (see Eq. 3.4) has been used to calculate the pressure drop by adjusting particle diameter to fit the experimental pressure drop data (see Figure 3.5). The best-fit particle diameter is then defined as the effective particle diameter, which is 2.85 mm for polydispersed particle bed and 3 mm for irregular particle bed (IPB) (see Table 3.1).
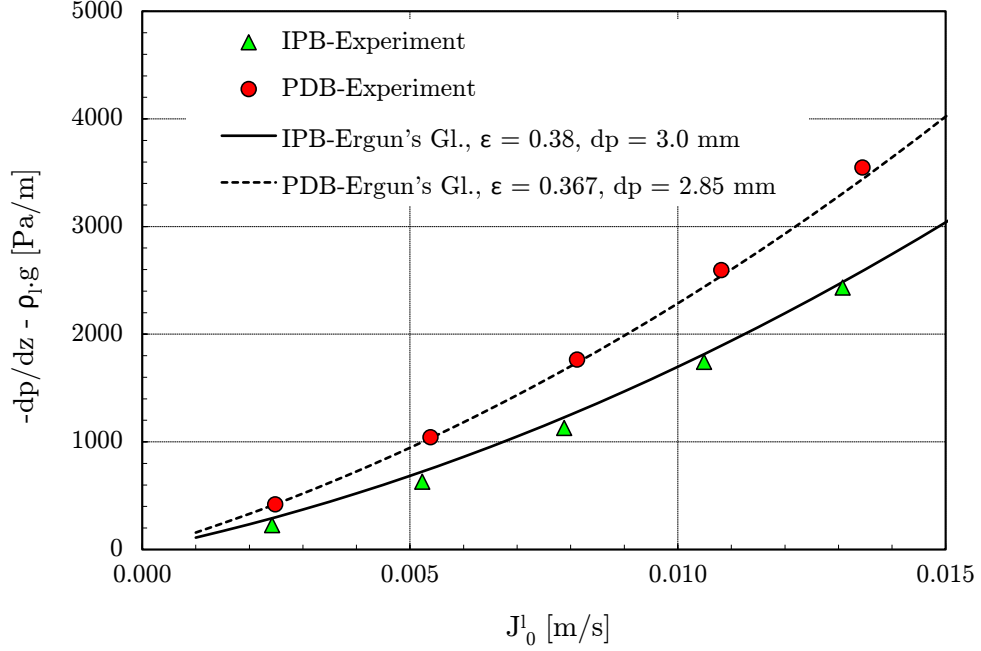
Figure 3.5: Overall single-phase pressure gradients for different particle beds, PDB and IPB.

3.2 Boiling Experiments

The aim of the boiling experiments is to test the friction laws based on pressure-drop measurements in a debris bed under steady-state boiling conditions. The local mass flow rates of liquid and vapor phase, in steady boiling state, result from the mass conservation equation, i.e. the locally evaporated liquid volume must at any section of the bed be locally replaced. The vapor mass and the derived local vapor mass flow or the local vapor superficial velocity $J_g(z)$ is calculated from the volumetric heating power of the bed. For this purpose, the heating power is integrated along the axial bed height (z) and using Eq. 3.6 the corresponding local vapor superficial velocity $J_g(z)$ is calculated.

$$J_g(z) = \frac{\int_0^z Q_{vol}(z)dz}{\rho_g h_{fg}} \tag{3.6}$$

where $Q_{vol}(z)$ is the volumetric heat-generation rate and h_{fg} is the heat of vaporization. With known $J_g(z)$ and $J_l(z)$ and the modeling approaches (see Section 1.2.2) the pressure gradient $-dp/dz$ and the local vapor content (void α) could be calculated. The boiling/dryout experimental results for defined experimental conditions (see Section 2.2 - 2.4) are discussed in the following sections.

Table 3.1: Effective particle diameter based on Ergun's equation and analytical mean particle diameters

Partile bed	Effective particle diameter	Volume mean/ Mass mean diameter	Area mean diameter	Length mean diameter	Number mean diameter
	d_e	d_v/d_m	d_a	d_l	d_n
PDB	2.85 mm	4.3 mm	3.53 mm	2.91 mm	2.53 mm
IPB	3 mm	-	-	-	-

(I) *1D top-flooding (water supply from top: without downcomer, with closed downcomer)*

In a nuclear reactor accident scenario with the failure of all cooling systems, a situation could arise where the only coolant supply to the heat-generating particles is from the existing water pool inside the reactor pressure vessel. In order to experimentally investigate such a scenario pure top-flooding experiments are carried out.

In pure 1D top-flooding (see Section 2.4) experiments no additional water was pumped into the bed ($J_l^0 = 0 \; mm/s$). The water, only driven by gravity, had to flow from the water pool above the bed down into the porous bed. Once the liquid starts boiling, the reflux condenser at the top was started which helps in maintaining a water pool above the bed. The steam generated by the particle bed moves upward and escapes from the top of the bed. In this case a counter-current flow between the rising steam and downward flowing water is established inside the particle bed.

At the DEBRIS test facility, previously, Schäfer [43] carried out some of the experiments for similar flow conditions (*1D top-flooding without downcomer*) and similar polydispersed particle bed configuration, hence, within this research work, those experiments were not repeated and also not discussed here.

Irregular particle bed without downcomer

In Figure 3.6 the pressure gradients as a function of vapor superficial velocity and vapor mass flux for IPB with $J_l^0 = 0 \; mm/s$ are given. The data shown are obtained, at given cooling conditions, for irregular particle bed (IPB) at three different system pressures [63], [64]. It has been noted that the pressure gradient observed for the entire vapor superficial velocity $J_g(z)$ range is negative. The system-pressure increase primarily has effect on the physical properties of the vapor phase of the coolant. With an increase in system pressure the vapor density increases strongly whereas the decrease in latent heat of vaporization is negligible. This leads to the fact that for the same volumetric heat input, at higher
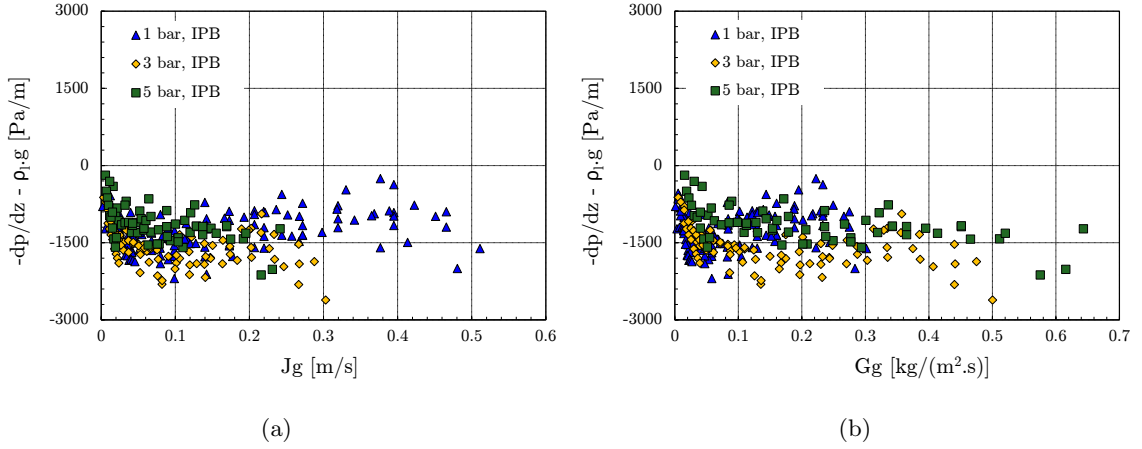
Figure 3.6: Measured pressure gradients vs. vapor superficial velocity resp. vapor mass flux for IPB , 1D top-flooding, $J_l^0 = 0$ mm/s, $p_{sys} = 1/3/5$ bar.

system pressure, significantly lower vapor volume exists (see also Eq. 3.6). This increase in vapor density means that at higher system pressure e.g. 3 bar and 5 bar relatively more vapor mass can be removed through the packed bed cross-section at the top (see Figure 3.6(b)), maximum vapor mass flux $G_g = 0.3/0.5/0.65$ $kg/(m^2 s)$ for $p_{sys} = 1/3/5$ bar. This also means that with the increasing system pressure there should be a decrease in the interfacial friction factor. This effect can be seen from the experimental data of the 5 bar experiments where a relatively lower pressure drop has been observed.

Polydispersed Particle Bed with closed downcomer

The particle bed formed, as a result of nuclear reactor accident, may have irregular bed geometry (e.g. heap-shaped bed) with non-homogeneous internal structure having high porosity regions. In parts of the bed the porosity could be large enough to develop a low friction (particle friction) downcomer like scenario. Based on the density difference between two phases and presence of a low friction region natural circulation of water may establish inside the particle bed. In order to study such a scenario experiments are carried out with a concentrically installed downcomer inside the particle bed. Three different variations of downcomer are investigated here. Here only the experimental results for flow conditions under closed downcomer configuration (see also Section 2.4) are discussed.

The goal of the experiments with closed downcomer was to study the coolability of the particle bed in a systematic manner to quantify the extent of changes with gradual changes in the flow conditions from (I) to (IV). The flow condition (I) with a closed downcomer in the center of the bed represents a pure 1D top-flooding condition (see Section 2.4) where the only water supply to the particle bed is from the water pool lying above the bed.

Figure 3.7 presents the measured pressure gradients for polydispersed particle bed, with a concentrically installed closed downcomer, both as a function of the steam superficial velocity J_g (see Figure 3.7(a)) and the vapor mass flux G_g (see Figure 3.7(b)). The pressure gradients are measured for three different system pressures 1 bar, 3 bar and 5 bar [65], [66]. The pressure gradients exhibit a typical pure top-flooding case behavior where a counter-current flow condition between the up flowing steam and the down flowing water sets inside the particle bed. Under a predominantly counter-current flow situation the interfacial friction plays the key role in determining the pressure gradient. The observed pressure gradients mainly maintained negative values for all three system pressures. For 1 bar system pressure and a vapor superficial velocity $J_g = 0.2 \ m/s$ or corresponding vapor mass flux $G_g = 0.1 \ kg/(m^2 s)$, the minimum pressure gradient is -3000 Pa/m while for higher system pressures around -1200 Pa/m (see Figure 3.7). A steady decrease in pressure drop with increasing system pressure can be derived from the increase in vapor density. This increase in vapor density also means that at higher system pressure, e.g. 3 bar and 5 bar relatively more vapor mass can be removed through the packed bed cross-section at the top (see Figure 3.6(b), maximum vapor mass flux $G_g = 0.32/ \ 0.53/ \ 0.72 \ kg/(m^2 s)$ for $p_{sys} = 1/3/5 \ bar$.

Though it is difficult to quantify the extent of influence from the presence of the tubular downcomer at the center of the particle bed, but compared to pure top-flooding case the influence, from the presence of the central tube, on the qualitative behavior of the pressure drop is negligible. Hence the experiments with irregular particle bed and closed downcomer configuration are not discussed here.

(a)   (b)
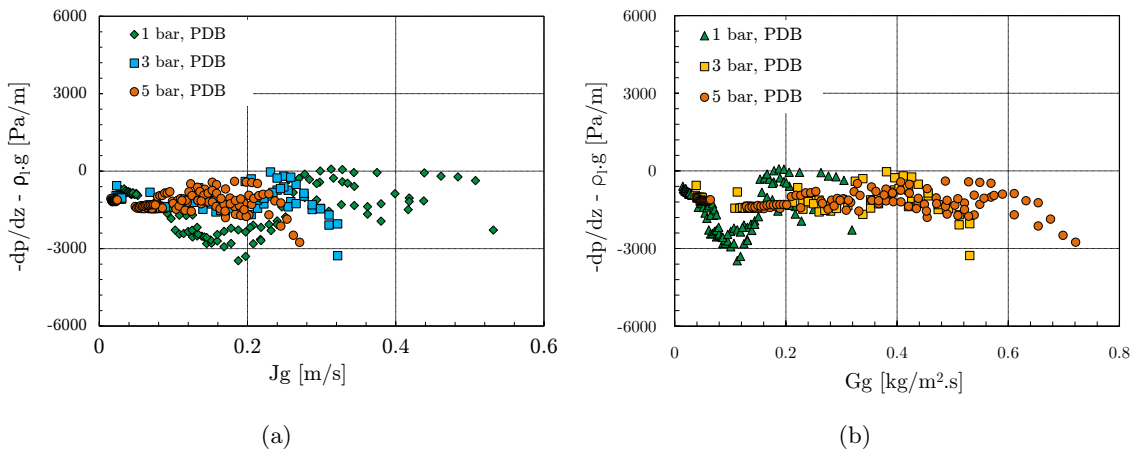
Figure 3.7: Measured pressure gradients vs. vapor superficial velocity resp. vapor mass flux for PDB, closed downcomer, 1D top-flooding, $J_l^0 = 0 \ mm/s$, $p_{sys} = 1/3/5 \ bar$.

3. EXPERIMENTAL RESULTS

(II) *1D bottom-flooding (water supply from the bottom using a pump, forced inflow)*

At certain stage of the nuclear reactor accident, where the molten core on coming in contact has formed a particle bed inside the reactor pressure vessel, the water may be pumped into the vessel to achieve a stable coolable state of the heat-generating particles. The bottom-flooding experiments with an external water supply via pump aim to develop an understanding of the above mentioned accident scenario. In order to investigate the basic thermo-hydraulics of bottom-flooding conditions, 1D bottom-flooding where water is pumped (see also flow condition (II)) into the bottom of the particle bed at different inflow rates, pressure gradients inside the bed were measured.

The experiments with 1D bottom-flooding via pump for polydispersed particle bed were conducted with similar flow conditions by Schäfer [46] and so in this section the experimental results with 1D bottom-flooding (via pump) are only presented for irregular particle bed (IPB).

Irregular particle bed

Figure 3.8 represents the measured pressure gradient data for 1D bottom-flooding experiments at three different system pressures 1 *bar*, 3 *bar* and 5 *bar* [63], [64]. The water is pumped (forced inflow condition) into the lower section of the bed at different inflow rates ranging from 0.5 *mm/s* to 7.1 *mm/s*. In this flow condition the steam generated inside the particle bed and the coolant water both flow in the same direction (upwards) and would result in a co-current flow condition inside the particle bed. However, a water pool is still maintained above the bed using a reflux condenser. Thereby, in addition to the forced inflow of water to the particle bed, depending upon the steam flow, water flows downwards into the particle bed. This leads to a counter-current flow condition, as observed in pure 1D top-flooding experiments; hence in parts of the bed a mixture of co- and counter-current flow exists. In case of bottom-flooding, it was observed that, due to heat losses, the inlet liquid temperature was below saturation temperature. So it was necessary to add a correction for sensible heating of subcooled liquid while calculating the vapor superficial velocities.

$$J_g(z) = \frac{\int_0^z \dot{Q}_{vol}(z)dz - GC_p^l(T_{sat} - T_0)}{\rho_g h_{fg}} \quad (3.7)$$

where G is the inlet mass flux with inlet temperature T_0. It can be seen from Figure 3.8 that, at very low bottom inflow rate ($J_l^0 < 1 \ mm/s$), the pressure gradient behavior is almost similar to top-flooding with small rise in maximum vapor velocity followed by
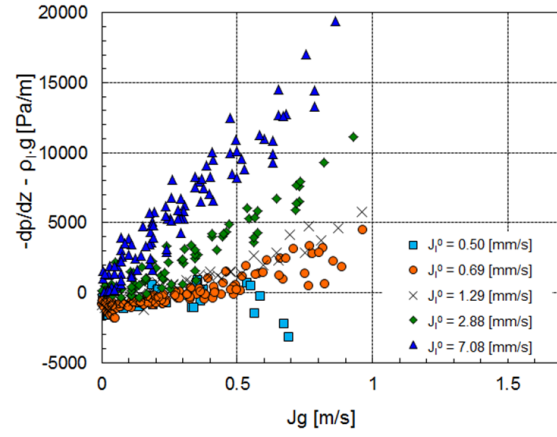
(a) 1bar
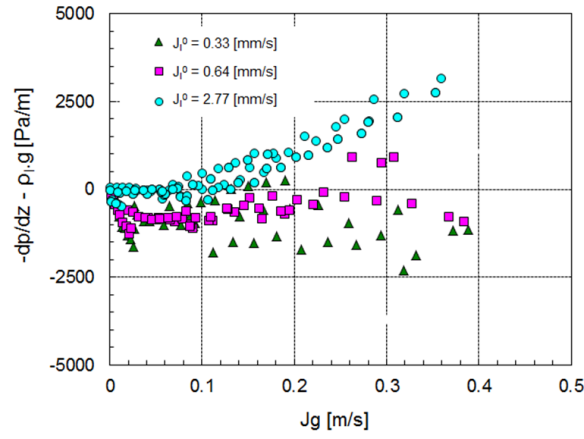
(b) 3bar
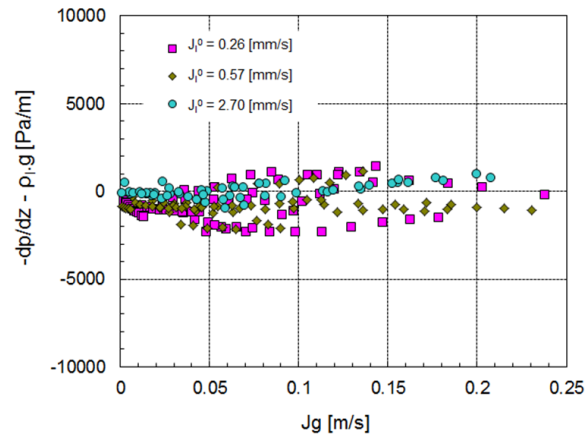
(c) 5bar

Figure 3.8: Measured pressure gradients vs. vapor superficial velocity for different inflow rates for IPB, 1D bottom-flooding via pump, $J_l^0 > 0$ mm/s, $p_{sys} = 1/3/5$ bar.

51

a subsequent drop in pressure gradient. The negative pressure-gradient profile for such small inflow rates indicate the presence of counter-current flow inside the particle bed. In this region the interfacial friction plays a dominant role. This effect is in particular more pronounced in results of 1 bar and 3 bar experiments with inflow rates of $J_l^0 = 0.5 \ mm/s$ and $J_l^0 = 0.69 \ mm/s$ for 1 bar and $J_l^0 = 0.33 \ mm/s$ and $J_l^0 = 0.64 \ mm/s$ for 3 bar respectively. In these experiments the pressure gradients maintain negative values for a larger range of vapor superficial velocity. The only exception here are the experiments at a system pressure of 5 bar (see Figure 3.8(c)). Initially, for very small vapor superficial velocities $J_l^0 < 0.69 \ mm/s$, with low water inflow rates $J_l^0 = 0.26 \ mm/s$ and $J_l^0 = 0.57 \ mm/s$, the pressure gradients take negative values, i.e. interfacial friction playing the key role. However, with increasing vapor superficial velocity (J_g) a large scatter in the pressure gradient data with alternating positive and negative values is observed. This measured data suggests an unstable flow conditions inside the particle bed with presence of co- and counter-current two-phase flow inside the particle bed, hence the key role switching between the interfacial friction and the fluid-particle friction.

As the bottom inflow rate increases ($J_l^0 < 1.3 \ mm/s$), the pressure gradient starts increasing with increase in vapor velocity. This is mainly caused by the co-current flow between vapor and liquid. In this scenario, the fluid-particle friction is the dominant component in the overall pressure gradient which increases with increase in both liquid as well as vapor velocities. At high liquid inflow ($J_l^0 = 7.1 \ mm/s$), there is almost a linear relationship of the pressure gradient with the vapour flow rate.

Figure 3.9 represents a comparison of pressure gradients for three different system pressures (1 bar, 3 bar and 5 bar) at an inflow rate of about $J_l^0 \approx 2.8 \ mm/s$. The maximum pressure gradients for 1 bar, 3 bar and 5 bar system pressure are about 11100 Pa/m at $J_g = 0.93 \ m/s$, 3100 Pa/m at $J_g = 0.36 \ m/s$ and about 1000 Pa/m at $J_g = 0.2 \ m/s$ respectively. The pressure measurements in 1 bar experiments exhibit relatively larger pressure gradients mainly due to the smaller vapor density. As explained earlier with the increase in system pressure there is a significant increase in the vapor density. Thus, in a given cross section of the particle bed, for lower system pressure (1 bar), more water will be displaced resulting in increased fluid-particle friction and hence higher pressure gradients.

(III) *1D top-/bottom-flooding (water supply from the top and bottom via internal/external downcomer, natural circulation)*

Non-homogeneous internal structure with high porosity regions may exist in a real nuclear debris bed. Such high porosity regions may even form local channels inside the
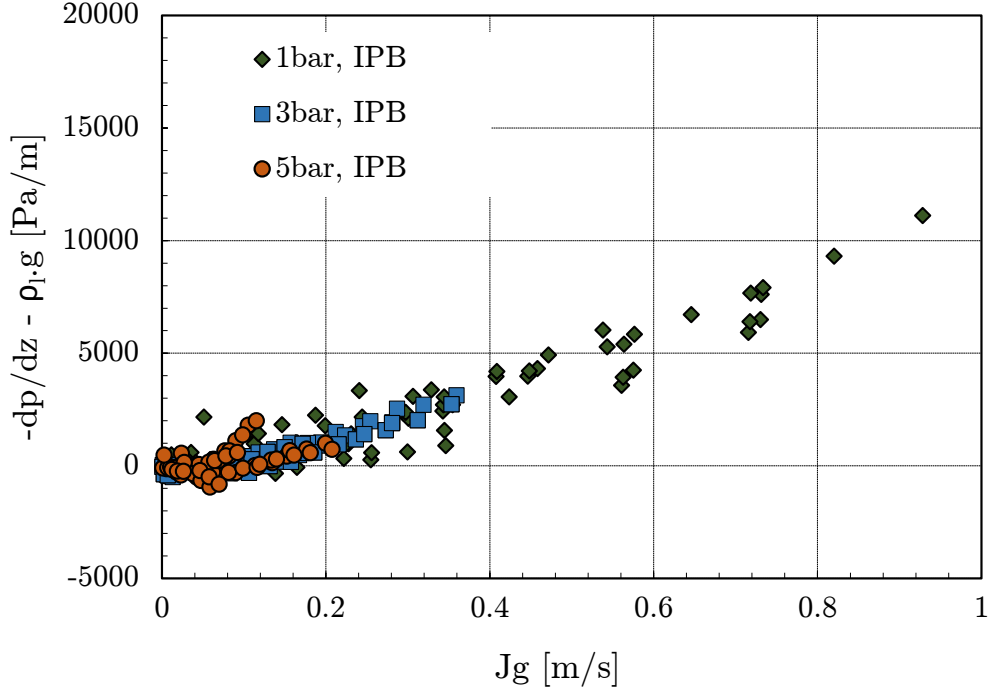
Figure 3.9: Comparison of pressure gradients, IPB, 1D bottom-flooding via pump, $J_l^0 \approx$ 2.8 mm/s, $p_{sys} = 1/3/5$ bar.

particle bed especially in the near-wall regions offering low resistance flow path to the water establishing a natural circulation of water inside the particle bed. For boiling/dryout experiments with 1D top-/bottom-flooding flow condition ((II), natural circulation) two doncomer configurations were investigated: *internal open downcomer* and *external downcomer*.

A concentrically installed downcomer open both at top and bottom was used in experiments to represent a hypothetical scenario where, in real debris bed, the existance of high porosity regions may lead to natural circulation via channel flow inside the debris bed. In addition to the water supply from top, the water may also flow into the bottom of the particle bed via open downcomer. As compared to the particle bed, where maximum flow resistance caused by two-phase flow exists, the open downcomer offers a low resistance flow path to the water. With an increase in vapor volume, caused by an increased heat input, the height of the water pool above the particle bed also increases hence the hydrostatic head on the top opening of the downcomer. Thereby the flow via the downcomer would also set-in leading to a water circulation loop inside the particle bed.

Additionally some boiling/dryout experiments with an external downcomer loop were also carried out. The external downcomer loop was connected, on one hand, to the overflow

line above the particle bed and, on the other hand, to the bottom of the particle bed. Under hydrostatic head the overflowing water entered the bottom of the particle bed via external downcomer. The liquid influx into the outer loop depends, on one hand, on the density dependent pressure difference (void) and the friction pressure ratios of two-phase flow (interphase and fluid-particle friction) in the bed, and on the other hand, on the hydrostatic head of the water column and the frictional pressure loss in the outer connection loop. Even though the external downcomer line is well insulated but still, due to unavoidable heat losses along the circulation line, liquid sub-cooling takes place. The sub-cooling of the water results in more heat being used for the sensible heating of the lower part of the particle bed and hence less latent heat is available for evaporation.

Polydispersed particle bed with internal open downcomer

This section describes the experimental results for polydispersed particle bed under open downcomer flow conditions at three different system pressures 1 bar, 3 bar and 5 bar[66]. Figure 3.10 represents the measured experimental pressure gradients with an

(a)   (b)
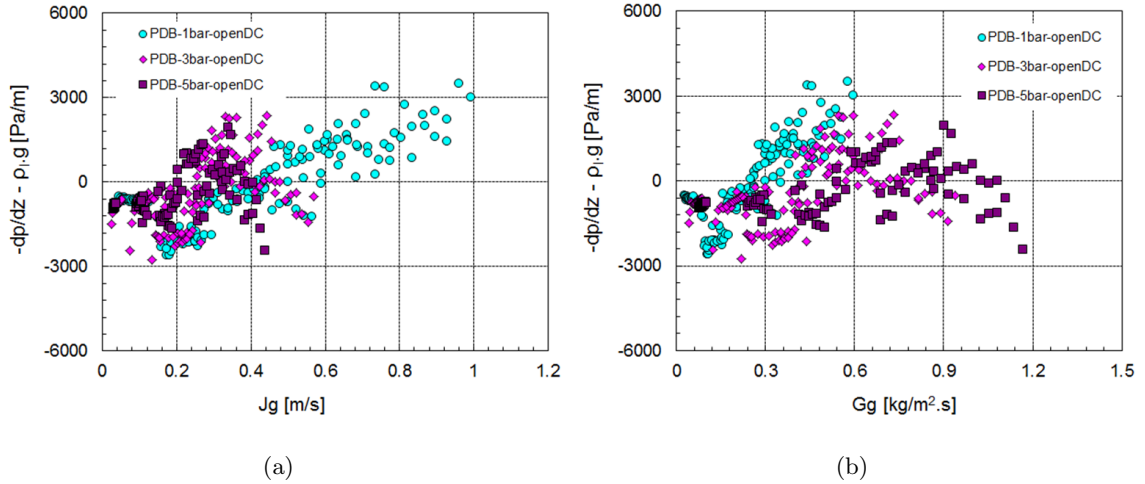
Figure 3.10: Measured pressure gradients vs. vapor superficial velocity resp. vapor mass flux for PDB, internal open downcomer, 1D top-/bottom-flooding, $J_l^0 = 0\,mm/s$, $p_{sys} = 1/3/5\,bar$.

internal water supply from the water pool above the particle bed via an open central downcomer (a PTFE tube installed in the center of the particle bed). The water inside the downcomer is approximately at saturation temperature. The internal flow through the particle bed is primarily driven by the pressure difference between the liquid column inside the downcomer and the two-phase flow inside the particle bed. In this flow conditions, in addition to the water supply from top, water also flows into the bottom of the particle bed leading to a mixed flow situation inside the particle bed. Predominantly, in the upper part

of the particle bed, a counter-current flow situation (between downward flowing water and the upward flowing vapor) exists. In the lower part of the particle bed, the water entering the particle bed via open downcomer flows in the same direction (upwards) as that of the vapor, resulting in a co-current flow situation.

The results with open downcomer show medium pressure drops, for $Jg < 0.2\ m/s$ (approximately $-2400/-2000/-1800\ Pa/m$ for $p_{sys} = 1/3/5\ bar$), which mainly indicate the dominance of interfacial friction caused by counter-current flow condition. The pressure drop is followed by a significant increase in positive pressure gradient values e.g., at system pressure $1\ bar$ and $J_g = 1\ m/s$ to a maximum of $3000Pa/m$ ($2300/1800\ Pa/m\ J_g \approx$ 0.4 /0.34 m/s for $p_{sys} = 3/5\ bar$). This increase in pressure gradient values is caused by the dominance of fluid-particle friction over the interfacial friction. The conventional pressure reduction to negative values, when approaching individual dryout heat flux, is only seen at the higher system pressures ($3\ bar$ or $5\ bar$) but, interestingly, not at $1\ bar$. A conclusive explanation for this could not be found. The changes to the pressure gradient values indicate the presence of both co- and counter flow conditions, and hence suggest a change in the dominance regions of the individual friction terms (interphase friction, fluid-particle friction) determining the overall pressure drop of the particle bed. The effect of increase in system pressure can be seen in Figure 3.10(b). With increase in system pressure more steam is produced and removed from the particle bed before the counter-current flooding limit (CCFL) between water and vapor is reached. This would result in vapor blocking the downward flowing water from entering parts or complete cross section of the particle bed. The limited or no water access to the parts of the bed lower than that level results in dryout of the bed. The area-based vapor mass flow $G_{(g)}$ almost doubles from $G_{(g)} = 0.6\ kg/(m^2s)$ at $p_{sys} = 1\ bar$ to about $G_g = 1.15\ kg/(m^2s)$ at $p_{sys} = 5\ bar$ (see Figure 3.10(b)).

Irregular particle bed with an internal open downcomer

For irregular particle bed with an internal open downcomer (1D top-/bottom-flow condition), experiments were carried out at $1\ bar$. In boiling experiments the heat input was gradually increased and for each step increase in heat input steady-state data for both temperature and pressure is measured. The heat input was increased till one or more thermocouples indicate a steady increase in bed temperature which is defined as the coolability limit of the particle bed. For irregular particle bed, due to relatively lower heat generation by the particles (see also Section 3.1.1), even at the highest heating level 10 (heating level range 0 to 10) no thermocouple indicated an increase in temperature above saturation temperature (see Figure 3.11). This means under given boundary conditions
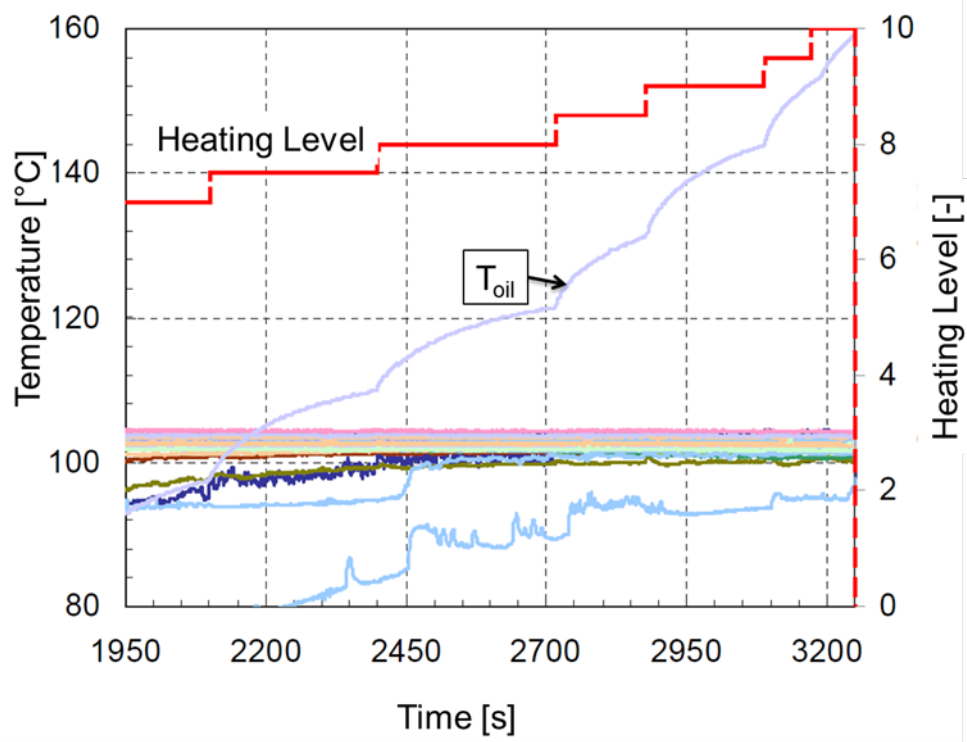
Figure 3.11: Irregular particle bed temperature and oil temperature (cooling oil for inductive coil) profile at different heating levels, internal open downcomer, 1D top-/bottom-flow condition, $p_{sys} = 1\ bar$.

(at maximum heating capacity of the experimental setup) the particle bed is still in a coolable state with no dry zone. At such high heating level, the other factor limiting the capacity of the experimental setup is the temperature of the oil which is being used to cool the inductive heating coil. The rise in oil temperature with increasing heating level is also shown in Figure 3.11. The experiment has to be shut down in order to avoid any damage to the heating system. For higher system pressure of 3 *bar* and 5 *bar*, this limiting factor (increase in oil temperature) would have been even more critical. In case of higher system pressure, to achieve steady boiling conditions and adequate vapor mass flow higher heating level (heating level > 8) for longer period of time would have been needed. This would have resulted in a strong increase in oil temperature. Thereby for irregular particle bed with an internal open downcomer (1D top-/bottom-flow condition), due to the limitation of the setup, no meaningful data (pressure gradients and dryout heat flux) has been achieved.

Polydispersed particle bed with an external downcomer

The measured pressure gradient curve, for polydispersed particle bed with an external
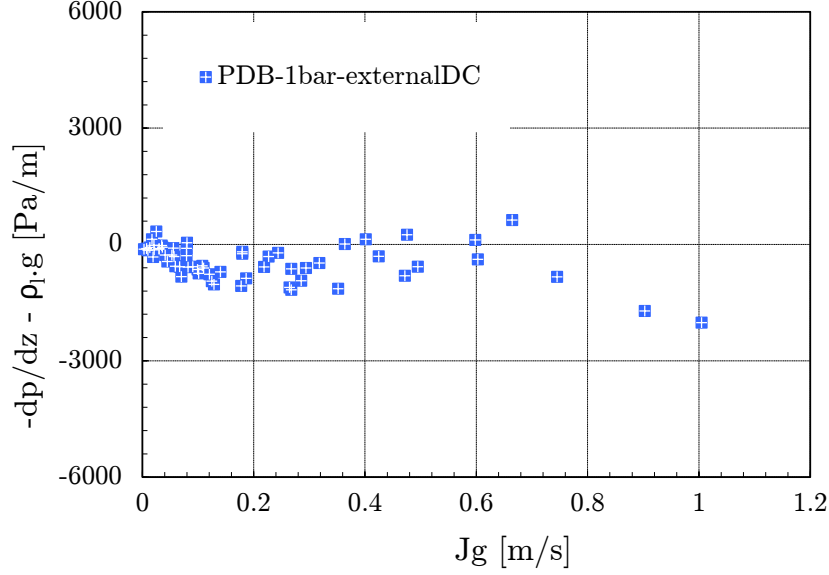
Figure 3.12: Measured pressure gradients, PDB, external downcomer, 1D top-/bottom-flooding, $p_{sys} = 1$ bar.

downcomer, shows larger vapor superficial velocity range (J_g) (see Figure 3.12). The data also display the characteristic shape of the boiling experiments with pure top-flooding condition (counter-current flow condition with dominant interfacial friction term). For smaller vapor superficial velocities ($J_g < 0.2$ m/s) the pressure drops to an average value of -1000 Pa/m before rising again with increasing J_g values. With further increase in vapor superficial velocity (increased heat input), when approaching the dryout heat flux, a second drop in the pressure is observed (approx. -2000 Pa/m at J_g 1 m/s). Due to the low driving pressure differences and the associated small liquid inflow into the particle bed, a co-current flow between water and vapor is only expected in the lower parts of the particle bed, while predominantly, as also indicated by the measured pressure gradient trend (see Figure 3.12), in the larger (upper) parts of the particle bed counter-current flow between the water and the vapor is expected.

Irregular particle bed with an external downcomer

For irregular particle bed, with an external downcomer, no useful data could be ob-

tained mainly because of highly unstable temperature and pressure behavior of the particle
bed. Figure 3.13 represents the measured temperature and pressure data for different gen-
erator levels at 1 bar system pressure, which illustrates the highly instable behavior of the
experiment. No steady-state saturation temperature ($T_{sat} = 100°$C at 1 bar system pres-
sure) could be achieved mainly caused by strong local fluctuations in temperature where
with the increase in applied heat input (heating level > 9) temperature rises up to 170
°C. Strong temperature increase induces strong oscillations in pressure measurements (see
lower diagram in Figure 3.13). Due to large instabilities, no useful interpretation from the
measured data could be made.
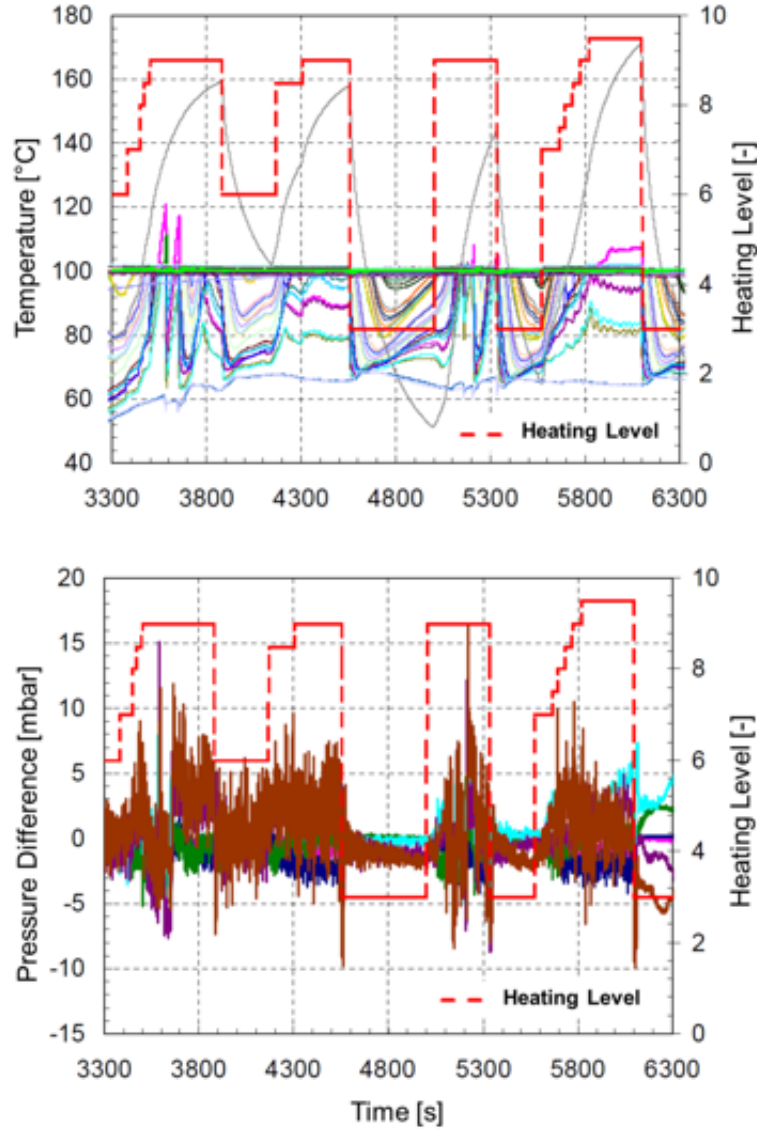
Figure 3.13: Temperature and pressure measurements, IPB, external downcomer, 1D top-
/bottom-flooding, $p_{sys} = 1$ bar.

(IV) *2D top-/bottom-/lateral-flooding (water supply from the top with a per-forated downcomer)*

The flow conditions (I) to (III) discussed in earlier sections are more of one-dimensional in nature where the water is supplied to the particle bed either from top or bottom or simultaneously both, but in a real debris bed, formed as a consequence of a nuclear reactor melt down, the flow is more of a multidimensional nature. Analyses based on one-dimensional configurations underestimate the coolability in realistic multidimensional configurations, where lateral water access and water inflow via bottom regions are favored. In this set of experiments, the tubular downcomer is replaced by an axially perforated downcomer (see also flow condition (IV))[66]. The perforated downcomer will provide, in addition to top- and bottom-flooding, lateral flow of water to different parts of the particle bed. This would result, in comparison to top- and bottom-flooding conditions where water can only flow either from top or bottom or both, in an easy access of water to larger cross sections of the particle bed. Similar to open downcomer (1D top-/bottom-flooding condition) where natural circulation of water takes place, the perforated downcomer with lateral flow may lead to the development of local circulation loops of water inside the particle bed. So the lateral flow in combination with top- and bottom-flooding condition would result in a two dimensional (2D) flow condition inside the particle bed, which is more close to the flow in real debris bed. Relatively easy access of water to different sections of the particle bed would improve the long term coolability of the heat generating particle bed. In this section the experimental results for both polydispersed particle bed and irregular particle bed are discussed.

Polydispersed particle bed with perforated downcomer

Figure 3.14 presents the measured pressure gradient data for polydispersed particle bed as a function of the vapor superficial velocity J_g and the vapor mass flux G_g for three different system pressures 1 *bar*, 3 *bar* and 5 *bar*. Initially the pressure gradient follows a strong continuous decrease with maximum values of approximately -4800 Pa/m at $J_g = 0.16$ m/s, -4200 Pa/m at $J_g = 0.07$ m/s and $J_g = 0.09$ m/s at 1 *bar*, 3 *bar* and 5 *bar* system pressure respectively. With increasing vapor superficial velocities an equally strong increase in pressure gradients has been observed. With further increase in vapor superficial velocities a second drop in pressure, which is even stronger than the first drop at lower J_g values, takes place. The second drop in pressure also indicates the onset of dryout inside the particle bed with vapor mass flow rates of approximately $G_g = 0.37$ $kg/(m^2s)$, 0.6 $kg/(m^2s)$ and 0.72 $kg/(m^2s)$ at 1 *bar*, 3 *bar* and 5 *bar* system pressure respectively.

(a)

(b)
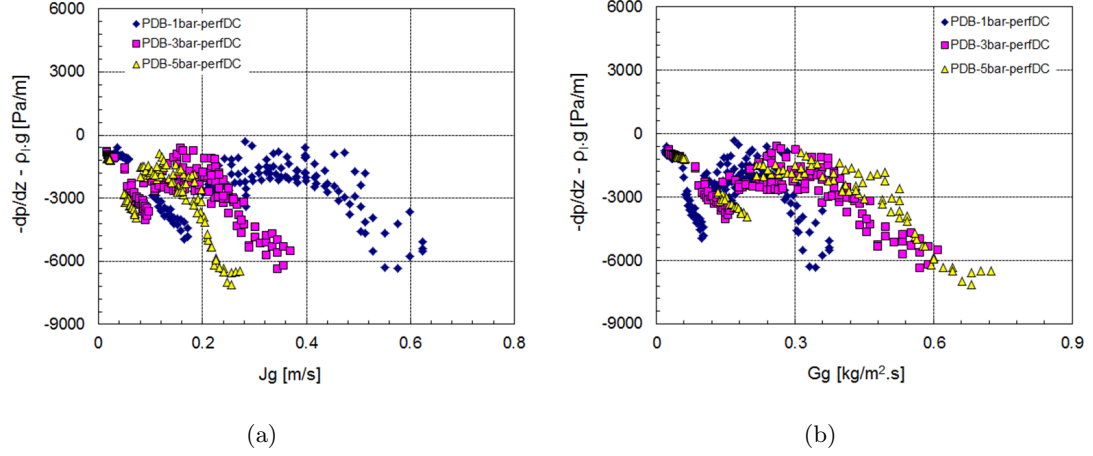
Figure 3.14: Measured pressure gradients vs. vapor superficial velocity resp. vapor mass flux for PDB, perforated downcomer, 2D top-/bottom-/lateral-flooding, $J_l^0 = 0 \ mm/s$, $p_{sys} = 1/3/5 \ bar$.

(a)

(b)

Figure 3.15: Measured pressure gradients vs. vapor superficial velocity resp. vapor mass flux for IPB, perforated downcomer, 2D top-/bottom-/lateral-flooding, $J_l^0 = 0 \ mm/s$, $p_{sys} = 1/3 \ bar$.

Irregular particle bed with perforated downcomer

Figure 3.15 represents the measured pressure gradient data, for irregular particle bed (IPB) as a function of the vapor superficial velocity J_g and the vapor mass flux G_g only for system pressures 1 bar and 3 bar. Due to the limitation of the heating system (see a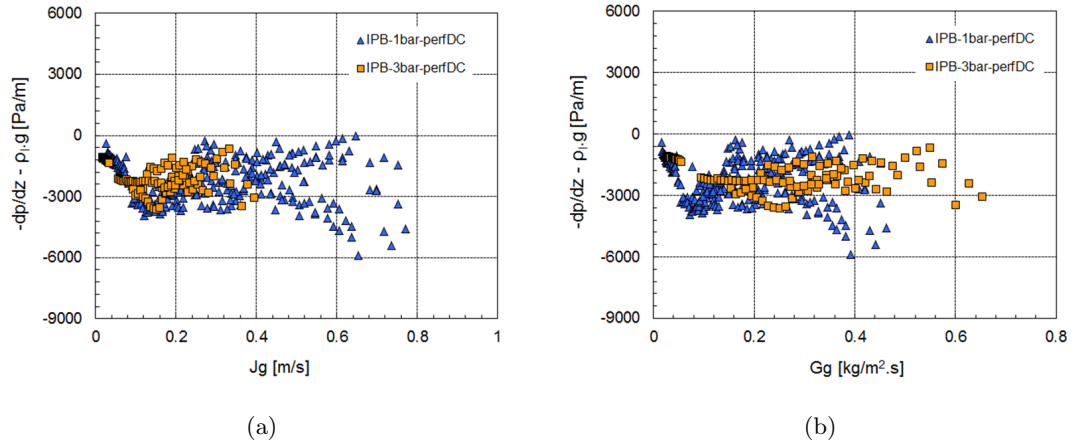lso Section 3.1.1) no measurements were carried out a system pressure of 5 bar. The measured pressure gradients show the typical behavior as observed in pure top-flooding conditions with predominately counter-current flow conditions. Within the range of small vapor superficial velocities of $J_g < 0.15$ m/s the pressure gradients drop to average value of approx. -3600 Pa/m both at system pressure 1 bar and 3 bar. As explained in earlier experimental results for pure top-flooding experiments, at low vapor superficial velocities the interfacial friction plays the key role. With the increase in vapor superficial velocity the pressure gradient $(-dp/dz - \rho_l g)$ reaches to an average value of almost zero, and with the further increase in vapor superficial velocity a second pressure gradient drop takes place to the point a dryout occurs inside the particle bed. At dryout the maximum vapor mass fluxes takes the value of approx. $G_g = 0.44$ $kg/(m^2 s)$ and 0.64 $kg/(m^2 s)$ at system pressure 1 bar and 3 bar respectively. The idea to investigate the lateral flow condition via perforations in the downcomer was to have increased water circulation inside the particle bed which would have resulted in improved coolability of the particle bed. But the results, in comparison to the open downcomer flow condition results, did not indicate any further enhancement in the coolability of the particle bed. Rather the values of the maximum vapor mass flux with perforated downcomer, for polydispersed particle bed, are 35 % lower than the values observed for open downcomer flow condition. In order to understand the plausible explanation for this contradictory behavior, visual observations were made in a separate test with reduced bed height. For perforated downcomer flow condition and a system pressure of 1 bar the boiling processes inside the particle bed were visually observed. It was observed that the steam bubbles penetrate the perforated central downcomer, and create a counter-current flow situation inside the downcomer. This effect intensified with increasing vapor content and at a point became so strong that the whole flow cross section of the downcomer was completely blocked by the rising bubbles, thus prevented the flow of liquid through the downcomer and hence the desired natural circulation has been brought to a standstill in the bed.

3.3 Dryout Experiments

The dryout experiments are mainly the study of the long-term coolability of the debris bed. In a volumetrically heated saturated debris bed, the heat is transported out of the

bed via vaporization. The dryout heat flux (DHF)is the maximum amount of heat that could be removed from the upper surface of the particle bed via vaporization under steady-state boiling conditions without the onset of dryout. The formation of a dry zone marks the onset of dryout inside the particle bed and i.e. under given conditions the bed is no more in a coolable state. In terms of a reactor case, non coolable debris bed means the decay heat present in the real debris bed can no longer be removed by the coolant flow or corresponding evaporation of the coolant. The dryout would be followed by the heat up and subsequently may lead to the melting of the debris bed. The experimental procedure is carried out to determine the dryout heat flux (DHF) by a gradual, small increase in heating power. The onset of dryout is defined when one or more of the thermocouples installed inside the particle bed indicate a continuous increase in bed temperature above saturation temperature.

Figure 3.16 shows the heat input, the measured temperatures and the pressure differences of dryout experiments with irregular particle bed under pure top-flooding conditions at 1 bar system pressure. The saturated particle bed is heated using the inductive heating system and the heat input is increased in small steps allowing the thermal steady-state to establish in between the heat input increments. At $t = 2900$ s, When the heat input is increased from (corresponding heat flux values) 744 kW/m^2 to 791 kW/m^2 (see Figure 3.16) the pressure difference "dp5" decreases to a negative value within a few seconds, and then decreases continuously, indicating that the counter-current flow limit at position "dp5" resp. at corresponding bed height (see Figure 2.3) has been reached. With ongoing heating, the counter-current limit is reached at lower bed positions ("dp4", "dp3" and "dp2") as well. Dryout does not occur immediately after the drop of "dp5". The initial dryout (increase in temperature above saturation temperature) starts at about $t = 900$ s after applying the dryout heat flux and at the position of "T13" (lower bed position, see also Figure 2.3), when "dp2" almost decreases to its lowest value. As the heating continues the dryout area extends to other regions of the particle bed. Immediately after the stop of heating, the temperatures of the dryout area decrease quickly.

The dryout position also depends on the magnitude of the applied heating power and also on the stepwise increment of heating power. Figure 3.17 shows the dryout behavior with an abrupt increase in heating power from 76 kW/m^2 to 840 kW/m^2. After the increase a sudden jump in pressure difference was observed (see Figure 3.17 and the pressure differences quickly decreased to negative values. The first temperature increase above saturation temperature (dryout) occured in about 150 seconds, which was much shorter than the case shown in Figure 3.16. The initial dryout position also shifted to a higher bed position at "T29" (see Figure 2.3). However, as the heating continues the dryout area

(a)

(b)
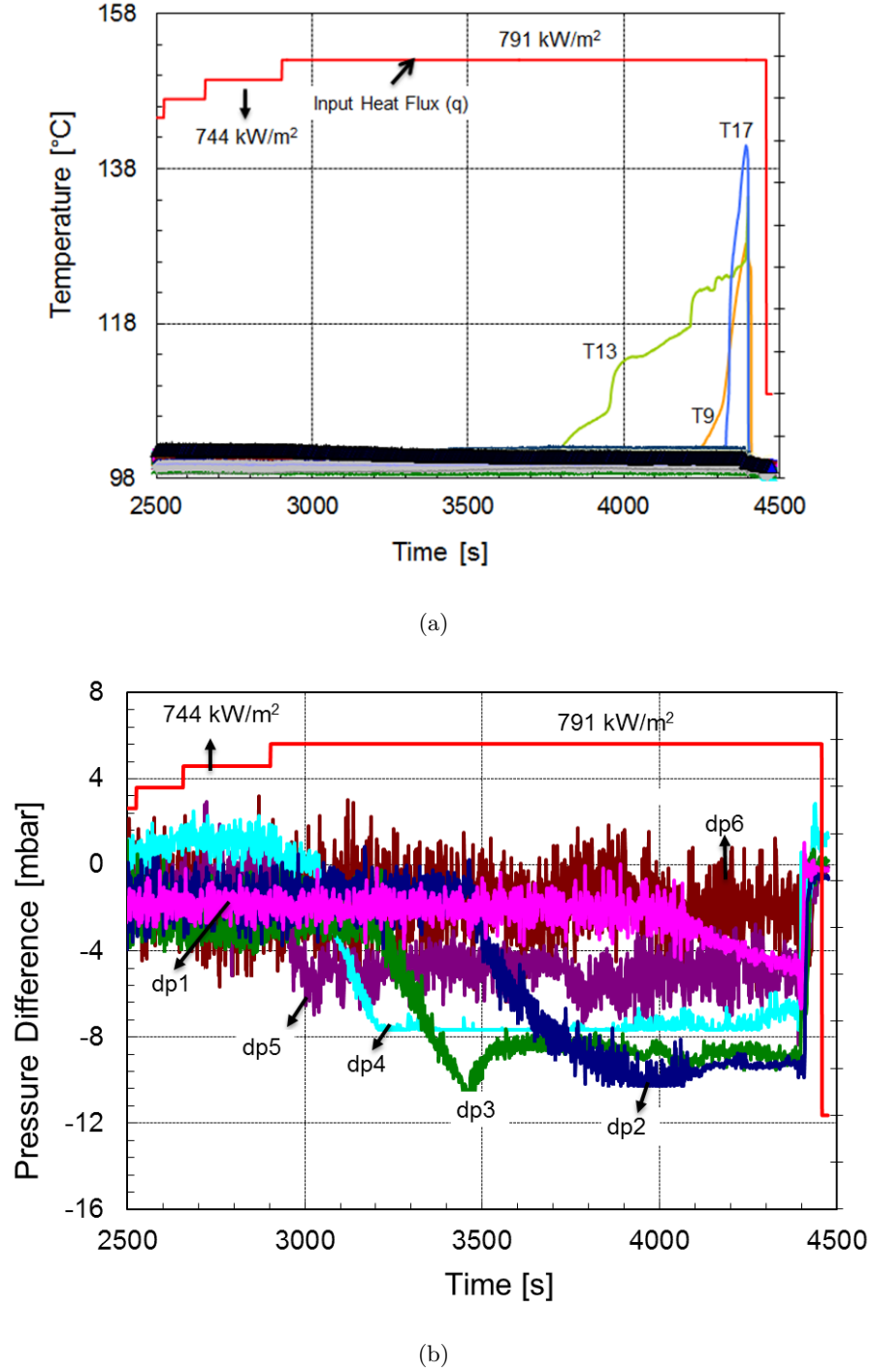
Figure 3.16: Temperature and pressure difference profile during dryout experiment for IPB, small step increament in heat input, 1D top-flooding, $J_l^0 = 0 \; mm/s$, $p_{sys} = 1 \; bar$.

(a)

(b)

Figure 3.17: Temperature and pressure-difference profile during dryout experiment for IPB, large step increament in heat input, 1D top-flooding, $J_l^0 = 0\ mm/s$, $p_{sys} = 1\ bar$.

extended mainly downwards. After the heating is switched off, the temperatures of the dryout area decreased quickly, whereas the pressure differences did not recover until all temperatures return to the saturation temperature, because due to the heat capacity of the superheated particles in the dryout area still continues to provide heat for evaporation. Due to the use of the PTFE-crucible the dryout experiments had to be stopped when a maximum temperature of 160 °C was reached in the bed.

An important observation in these experiments is the sharp drop in pressure before an increase in bed temperature is indicated by the thermocouples. Such pressure drop indicates the increase of vapor contents and decrease in available coolant water. Theoretically, under top-flooding conditions the dryout should occur at the bottom of the bed. However, when the heat input is increased in a big step to a value higher than the minimum dryout heat input, the water supply from the top pool can be throttled completely and dryout can occur at relatively upper bed areas (see also Figure 3.18). In measurements, the general temperature and pressure behavior of the particle bed when approaching the dryout heat flux (DHF) is found to be quite similar for all flow conditions.

(a) Small step increment in q (kW/m^2)

(b) Large step increment in q (kW/m^2)
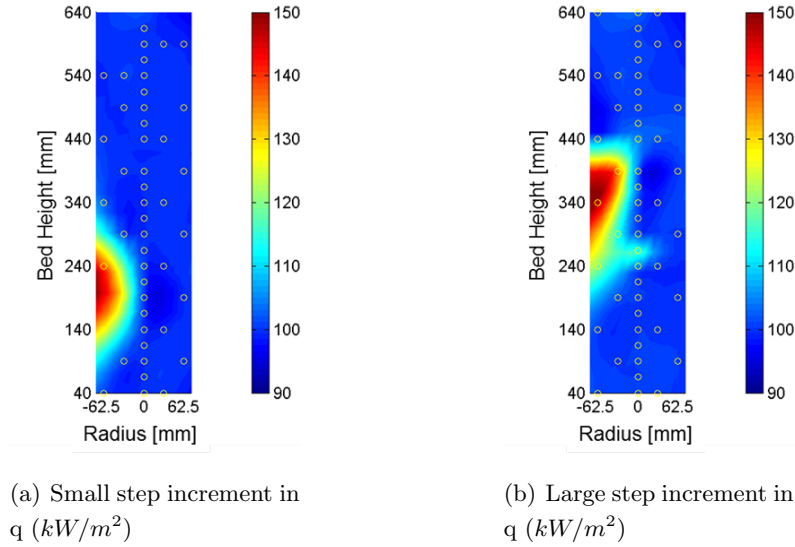
Figure 3.18: 2D Temperature profile indicating the dryout location for IPB, 1D top-flooding, $J_l^0 = 0\ mm/s$, $p_{sys} = 1\ bar$.

3. EXPERIMENTAL RESULTS

Dryout Heat Flux

The Figures 3.19 and 3.20 show the calculated dryout heat flux densities (DHF) of the polydispersed particle bed and the irregular particle bed for different flow conditions (see Section 2.4) and different system pressures (1 *bar*, 3 *bar* and 5 *bar*) [66].

In Figure 3.19 a comparison of dryout heat flux density for polydispersed particle bed with concentrically installed downcomer is shown. For all the calculated DHF values a significant increase in DHF with an increase in system pressure is determined. With an increase in pressure from 1 *bar* to 5 *bar* the DHF increased in an order of about a factor of 1.7 (open downcomer, 1D top- / bottom-flooding), 1.8 (perforated downcomer, 2D top-/ bottom-/ lateral-flooding) and 2 (closed downcomer, 1D top-flooding). This significant increase is related to pressure dependent increase in the specific vapor densities and thus higher potential steam mass flows.

The maximum dryout heat flux density of 2626 kW/m^2 (p_{sys} = 5 *bar*) for experiments with open downcomer (1D top- / bottom-flooding), represents an increase of approximately 74% compared to the dryout heat flux density of q = 1509 kW/m^2 (p_{sys} = 5 *bar*) for the experiments with closed downcomer (1D top-flooding). In contrast, for experiments with internal perforated downcomer (2D top- / bottom-/ lateral-flooding) the DHF was maximum of about 30% (p_{sys} = 1 *bar*) of the one obtained in experiments with closed downcomer (1D top-flooding). The inflow of vapor bubbles into the perforated downcomer resulted in a counter-current flow inside the perforated downcomer which lead to partial blockage of the downcomer flow area (see Section 3.2: 2D top-/bottom-/lateral-flooding (Water supply from top with perforated downcomer)).

Due to poor electromagnetic coupling of the irregular particle bed an insufficient heat generation resulted and certain limitations were realized in dryout experiments. In this case the dryout heat flux could only be reached for the flow configurations (I), (III) and (IV). Again, the strong pressure-dependent increase in the DHF values is observed (see Figure 3.20). For experiments with closed downcomer, the dryout heat flux density increased by a factor of 1.8 with an increase in system pressure from 1 *bar* to 5 *bar*. Dryout heat flux densities also increased with better coolant supply to the bed e.g. with perforated downcomer where in addition to top-flooding, bottom- and lateral-flooding was also provided. For experiments with perforated downcomer in the center of the particle bed, the dryout heat flux density increased by a factor of 1.3 with an increase in system pressure from 1 *bar* to 3 *bar*, here in the DHF value (due to heat generation limitation, see also Section 3.1.1) could not be reached at 5 *bar* system pressure. The maximum dryout heat flux density of 1630 kW/m^2 is reached at p_{sys} = 3 *bar* for experiments with perforated

66
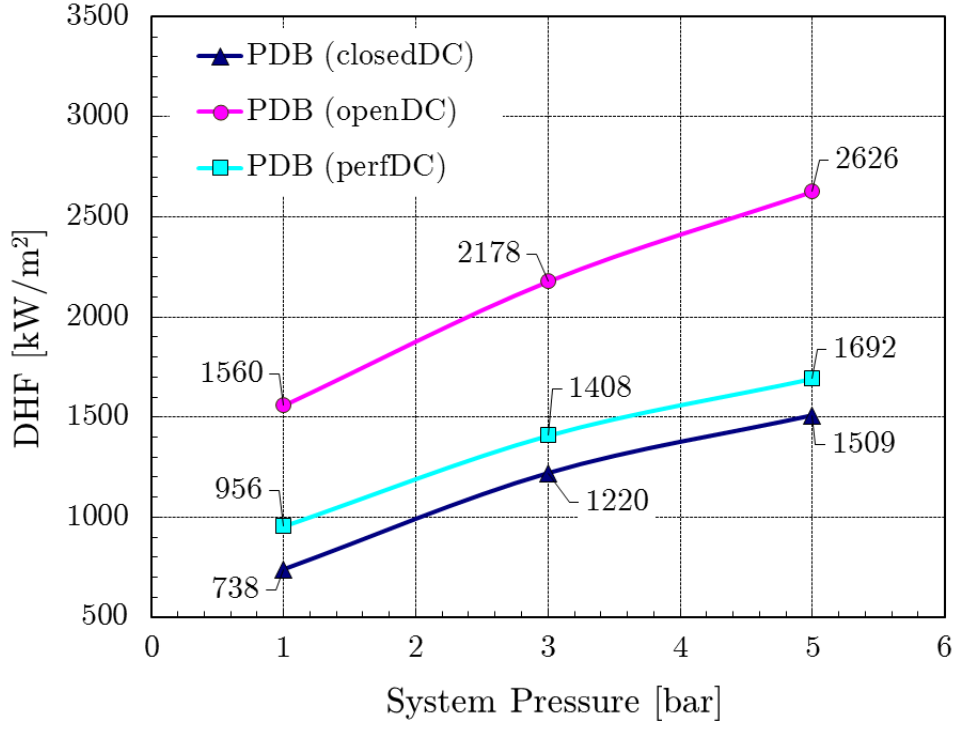
Figure 3.19: Dryout heat flux for PDB, internal downcomer configurations, $p_{sys} = 1/3/5\ bar$.

downcomer (2D top-/bottom-/lateral-flooding), representing an increase of approximately 35% compared to the dryout heat flux density $q = 1206\ kW/m^2$ of the experiment with closed downcomer (1D top-flooding) at system pressure $p_{sys} = 3\ bar$. The reasons for this DHF increase rates are the same as in the case of polydispersed particle bed, namely, increased specific steam density at higher system pressures and increased coolant supply through perforated central downcomer to the bottom and radial bulk regions, which allows an increased steam production.
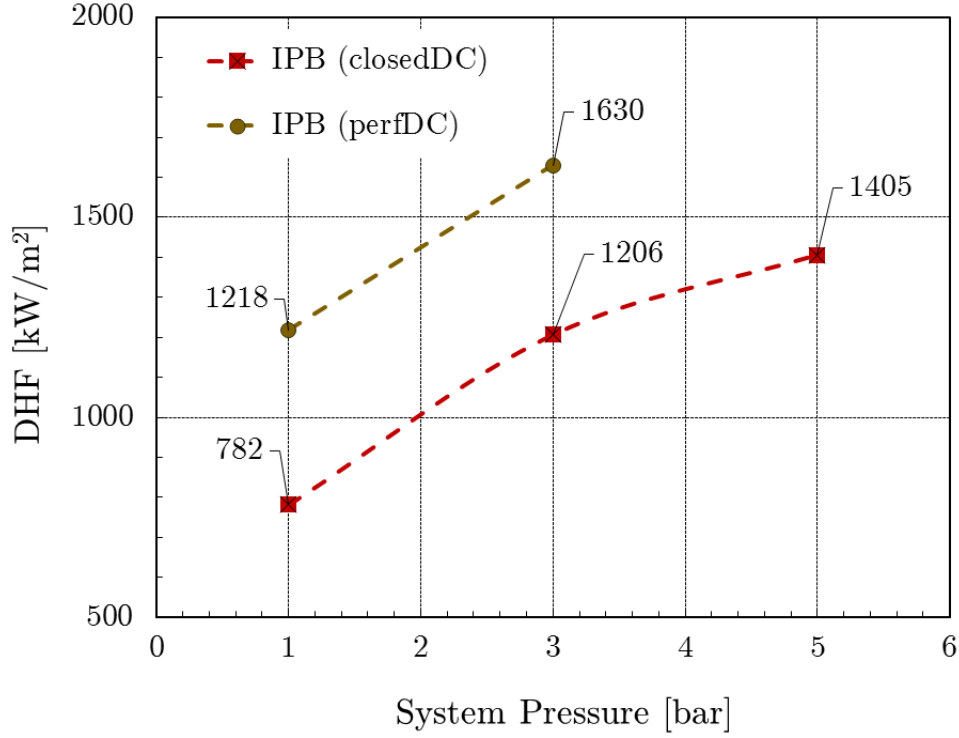
Figure 3.20: Dryout heat flux for IPB, internal downcomer configurations, $p_{sys} = 1/3/5\ bar$.

3.4 Quenching Experiments

During the course of a nuclear accident, with the depletion of the coolant reservoir a dry bed situation arises. Due to the presence of the decay heat the dry bed heats up and the temperatures rise above saturation temperature. To avoid any damage to the RPV, the removal of decay heat is of great importance. The debris bed needs to be quenched by water either flooding from the top or flooding from the bottom until continuous cooling is established. In an accident scenario, quenching of the hot debris is one of the first problems to be faced. The quenching experiments are related to the study of cool down behavior of dry hot debris bed i.e. heat transport from hot and dry debris bed (particle bed with zero liquid saturation and above saturation temperatures).

The particle bed is inductively heated to pre-defined temperatures. Due to unavoidable heat losses from the wall of the test section to the surroundings and a non-uniform heat generation by the particle bed, a non-uniform temperature profile exists inside the particle bed. Hence, the initial temperature conditions are characterized by three different temperature notations (see also Table 2-6) i.e. average temperature (T_{avg}), average temperature in the center of the bed (T_{cent}) and and local maximum temperature in the whole bed (T_{max}). Due to safety reasons the inductive heating is turned off before flooding

the particle bed. The inductively pre-heated debris bed is flooded with coolant (water) at about 15 °C in all the tests. Similar to boiling/dryout experiments, different cooling concepts have been investigated for quenching of the hot debris bed. In the study cases with coolant supply from the top (all top-flooding experiments, Table 2-3) the particle bed is supplied with cooling water in a quick manner. The large amount of coolant water supplied forms a water pool above the hot particle bed, from which the further flooding of the bed takes place. During the flooding process the height of the water pool was maintained at 200 mm above the upper surface of the particle bed by continuously adding cooling water to the system with excess water leaving the system via an overflow [67]. In case of bottom-flooding the coolant water is supplied either by pump, a forced flow coolant supply with constant mass flow (flow condition (II), Table 2-3) or alternatively, a gravity-driven coolant flow under hydrostatic pressure of a water column from a reservoir (flow condition I).

For polydispersed particle bed quenching experiments for a larger initial temperature range have been performed for a bed height of 640 mm and 200 mm. Whereas for irregular particle bed certain limitations, caused by different technical problems e.g. poor inductive heat, cracks in test section and in some cases breakup of the test section induced by the thermal shock etc., have been realized which resulted in change of test section more often than expected and the experiments are only carried out with a reduced bed height of 340 mm (flow condition(I), (II)and (III: external downcomer)) and 200 mm (flow configurations (II: internal open downcomer) and (IV) (see Table 2-3). The experimental results described in this section discuss the time dependent quench front progression and two-dimensional representation of the temperature measurements along the bed height. During the progression of the flooding/quenching experiment, the quench front is defined by the drop of the bed temperature to saturation temperature ($T_{sat} = 100$ °C for water) in the respective location inside the particle bed and is determined by the thermocouple measurements in the respective regions. In the following sections below the experimental results, for quenching of dry hot bed, at ambient pressure conditions ($p_{sys} = 1$ bar) for different cooling concepts are described. Due to relatively large number of figures used in the section below, and the similarities found in the results, the experimental results are discussed for different cooling concepts but under separate sub-headings for two different particle beds (polydispersed particle bed and irregular particle bed).

(I) *1D top-flooding (water supply from top)*

Polydispersed particle bed

3. EXPERIMENTAL RESULTS

In top-flooding quench experiments, after switching off the heating for safety reasons, the superheated (above saturation temperature) particle bed was flooded with cold water from top via an overlying water tank. Within a short interval of time a water pool was formed on top of the particle bed. The height of the water pool is maintained by a continuous supply of water to the water pool and the excess water is taken out of the system via an overflow line. The top-flooding quenching process is quite complex and more three dimensional in nature and is generally described by two-phase water progression.

In the first quench phase an inhomogeneous, continuous cooling of the particle bed cross section from top to bottom occurs. This quench phase is predominantly controlled by the initial bed temperature conditions. In case of moderate initial bed temperatures (see Figure 3.21) at the very start of the top-flooding the quench front moves uniformly over the whole cross section of the bed. Initially only upper portions of the bed are cooled to saturation temperature. After a short time water starts to penetrate into the bed preferably near the wall regions, where the quench front propagates faster than in the rest of the bed (see Figure 3.21). This can be explained by the lower bed temperature and higher porosity (wall effect) near the crucible wall. A sharp decrease in temperature is observed when the quench front reaches a thermocouple.

Some thermocouple measurements show transient temperature behavior, e.g. "T44" and "T50" (see Figure 3.22). The amount of water available at the quench front dictates such transient behavior. If there is a sufficient amount of water available in certain parts of the bed, the thermocouples indicate a sharp decrease in temperature of the bed, but if the amount of water is insufficient at the quench front, the temperatures will remain on a superheated temperature level. Similarly, thermocouples "T22" and "T23", which are placed at the same axial position, show different quench behavior. Thermocouple "T23" shows a decrease in temperature whereas thermocouple "T22" remains at $\sim$ 322 °C for $\sim$ 148s until it is also cooled to saturation temperature. In case of higher initial bed temperatures a stagnant quench front at the top of the bed has been observed (see Figure 3.23), and the quench front mainly progresses in the near-wall regions until the water reaches the bottom of the particle bed.

In the second quench phase, once the water reaches the bottom of the bed, the quench front moves upward, and the temperature measurements indicate more of a one-dimensional quench front progression from bottom to top (see Figures 3.21, 3.23). The quench front progresses almost uniformly over the whole cross section of the particle bed and results in the quenching of remaining uncooled parts of the bed. Depending upon the
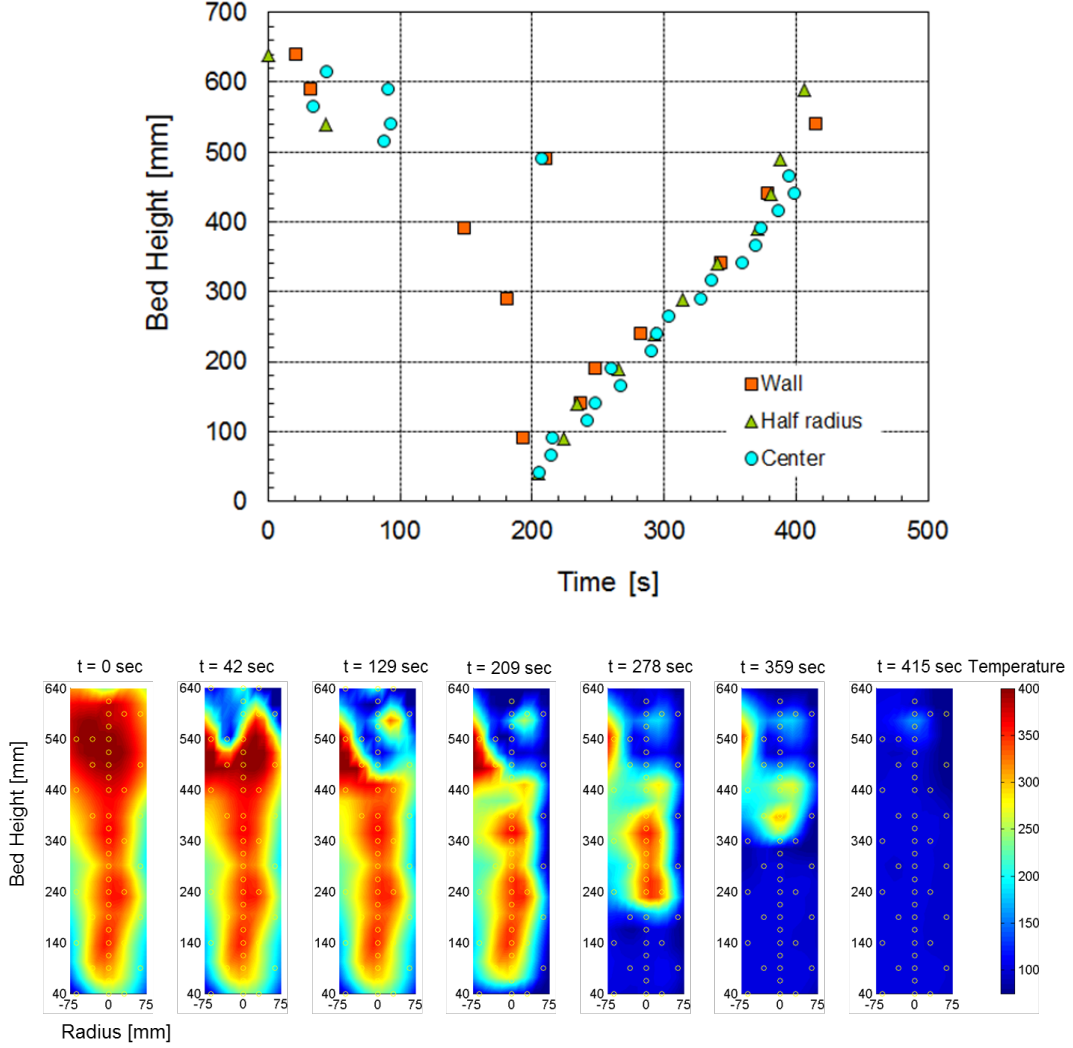
Figure 3.21: Quench-front progression and axial 2D temperature profile for PDB, 1D top-flooding, ($J_l^0 = 0\ mm/s$, $T_{max} = 432$ °C, Table 2-6).

initial temperature profile, the required quench times for the second quench phase are approximately $200s$ and $750s$ for experiments with relatively moderate initial temperatures ($T_{max} = 432$ °C, see Figure 3.21) and for experiment with relatively higher initial bed temperatures ($T_{max} = 747$ °C, see Figure 3.23). Similarly the overall quench time, i.e. whole particle bed cooled down to saturation temperature, are about $415s$ and about $935s$ for experiments with moderate ($T_{max} = 432$ °C) and higher ($T_{max} = 747$ °C) initial bed temperatures respectively.

As discussed earlier the characteristic cooling behavior during the top-flooding quenching experiments is governed by the initial temperature profile of the dry hot bed where inhomogeneous temperature profile of the particle bed has been observed. Significantly lower
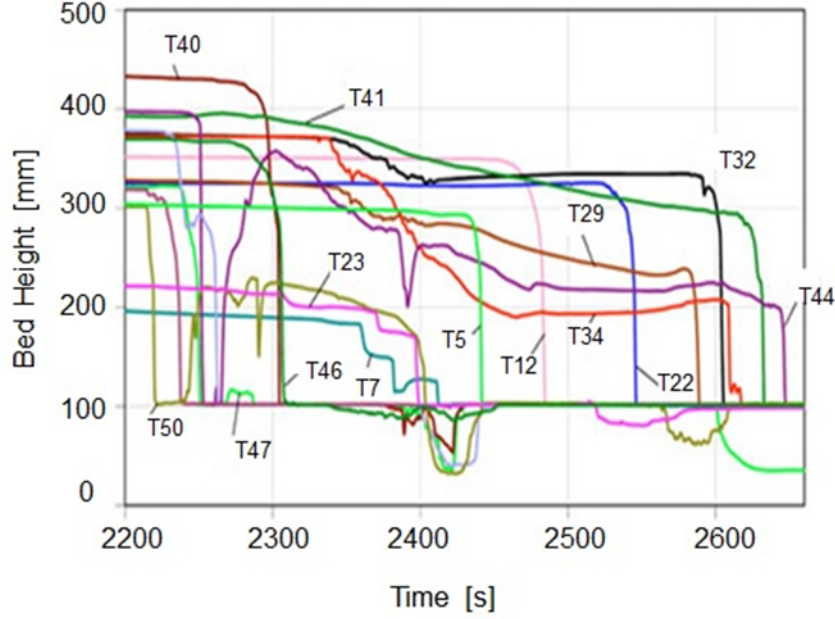
Figure 3.22: Temperature measurements during the quenching process, PDB, 1D top-flooding, ($T_{max} = 432°$C, Table 2-6).

bed temperature (caused by unavoidable radial heat losses to the surrounding through the wall of the test section and non-uniform inductive heating of the particle bed due to particle-size dependent electromagnetic coupling) and relatively higher bed porosity in the near-wall regions favor the penetration of the coolant from above into different parts of the particle bed. At the same time, on one hand, due to lower temperatures and hence lower thermal energy in the near-wall regions, relatively less steam is generated in the near-wall regions and consequently a lower center of steam flow counteracts the coolant (counter-current flow), on the other hand, due to less friction (higher porosity in the near-wall regions) the coolant can penetrate coolant easier, so that the particles can be cooled quickly. In the hotter core of the particle bed, central bed areas with relatively higher initial temperatures, however there is higher steam production which results in higher counter flow. Higher steam flows (counter-current flow limitation) combined with relatively higher particle friction in the bed core regions cause obstruction to the coolant inward ingression.

Both effects can cause faster ingression of coolant in the near-wall regions than in the center of the bed. Furthermore, there is the possibility of separation of the fluid phases, i.e. between inflowing water and the rising steam. The generated steam flows upwards preferably over dry bed areas, whereas the water flows downwards in streak like flow under gravity. Such flow patterns result in reduced interphase friction and internal heat exchange,
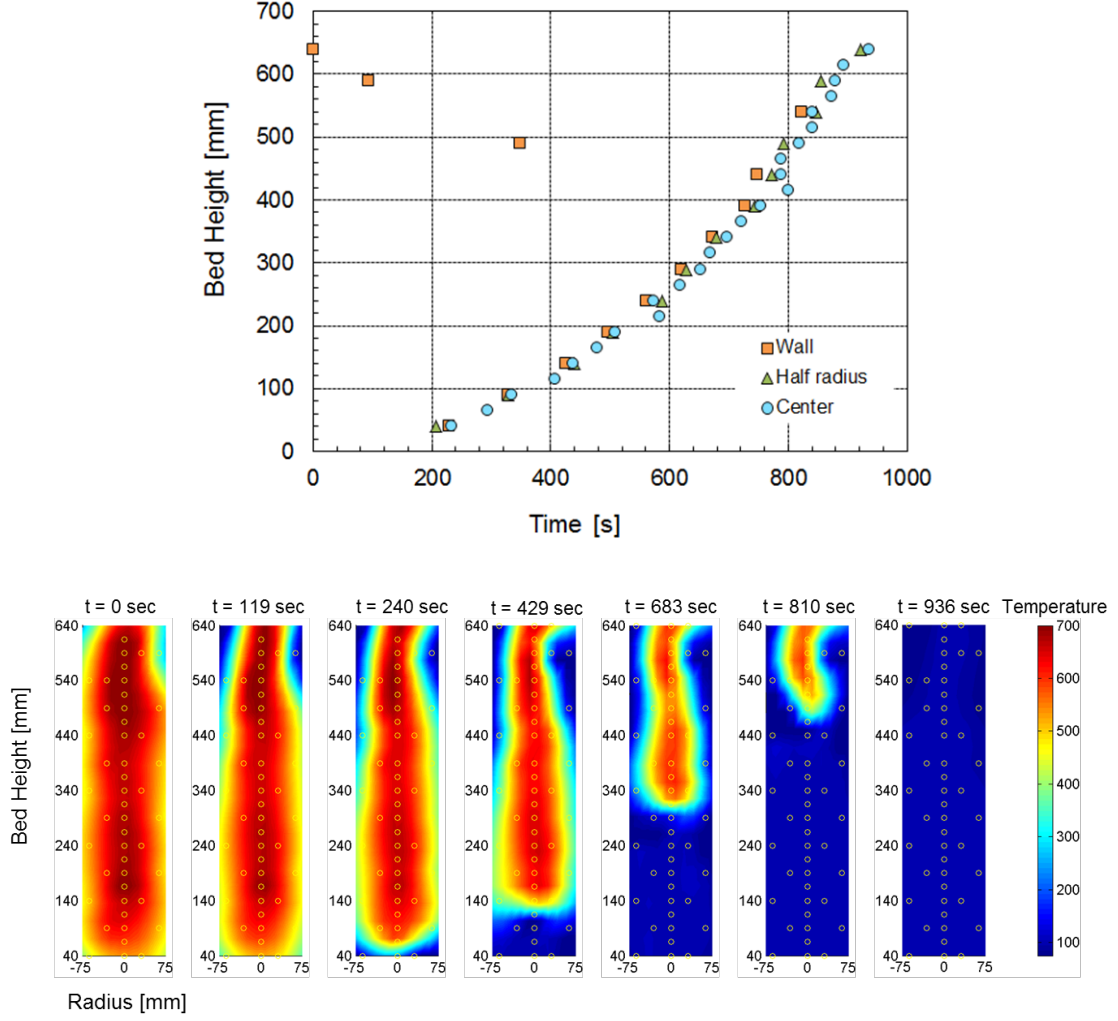
Figure 3.23: Quench-front progression and axial 2D temperature profile for PDB, 1D top-flooding, ($J_l^0 = 0$ mm/s, $T_{max} = 747$ °C, Table 2-6).

and hence lead to an inhomogeneous ingression of the liquid phase into the particle bed. With the available data could not be established which of the above discussed phenomena, the near-wall temperature and the effect of the porosity or the phase separation, play the dominant role in the first quench phase in determining the flow pattern,. However it is to be noted that with increasing initial bed temperature, the stagnant quench zone observed in the upper bed sections at the start of the flooding becomes more dominant and cooling only takes place close to the wall regions ($t<200$ s see Figures 3.21, 3.23). In this context one should also remember, that with the increase in the bed bulk temperature the film boiling phenomenon also becomes important which induces phase separation and thus a streak like channel flow of the coolant into the particle bed takes place.

The second quench phase is initiated when the coolant reaches the bottom of the particle bed. There exists quenched areas which, during the first quench phase, were cooled to Tsat (usually upper and local, lateral charge zones), and extended hot areas in the central axial core zone of the bed. In this phase the coolant water starts to fill up the bed and resulting in more of a bottom-flooding flow condition where both generated steam and the coolant water move in the same direction (upwards) resulting in a co-current flow situation and hence a faster quenching of the particle bed. In second quench phase the speed the flooding process may, however, be limited by the coolant supply via the cooled bed areas (streaks). Provided the water supply is as sufficient as needed for the fill-up and the quench front progression, no significant fluid mechanical restrictions are to be expected, and the quench time is then primarily influenced by the heat transfer conditions in the particle bed, i.e. the heat dissipation of the stored thermal energy from the particle bed by evaporation of the coolant. In this context a tendency is also observed that some wall regions reach the saturation temperatures (T_{sat}) slightly faster than, at the same height, further inward core bed sections (see Figure 3.23, measurement points wall, half radius and center). This behavior can be explained by the non-uniform initial temperature distribution (slightly lower temperatures in the wall regions) of the particle bed, which means that less heat energy has to be dissipated in the wall regions and thus may be quenched faster, and by the slightly higher bed porosity in the near-wall regions that allow a faster penetration of the coolant from bottom to top.

Irregular particle bed

Figure 3.24 shows the time based quench front progression and axial 2D temperature profile for quenching experiment with irregular particle bed (IPB)with reduced bed height of 340 mm under top-flooding conditions for an initial temperature profile with $T_{max} = 492$ °C. The upper most section of the bed is quenched immediately after the start of the quenching, and remains thermally stable during the whole quench process. Right after the start of the flooding, a stagnation phase has been observed, which indicates a counter-current limit between the liquid water and the generated vapor by the hot particle bed. Similar to the top-flooding case for polydispersed particle bed the quenching takes place in two phases. During the first phase the coolant water mainly flows downwards and at about $t = 100$ s reaches the bottom of the bed. Due to relatively higher porosities and radial temperature gradients the coolant water, preferably, flows in the near-wall regions (see Figure 3.24) and the near-wall bed regions are quenched to saturation temperature ($T_{sat} = 100$ °C). As soon as the water reaches the bottom of the bed, it starts filling up the particle bed and so the flooding front as well as the quench front progress in the upward direction. Similar to the flooding front ingression during the first quench phase, in the second quench phase the water front also follows the near-wall regions. This flow pattern can be attributed to the lower bed temperatures in the already quenched bed region and higher porosities near the wall. Over the course of whole quenching process some, thermally stable, local superheated regions have been observed. Some local in-homogeneities in the bed porosity can cause higher resistance to the fluid flow and hence impeding the access of coolant water to these regions.

As a result uncooled superheated regions, surrounded by cooled zones, are observed (see Figure 3.24, the temperature profile $t = 150$ s). The quenching process is completed at time $t = 199$ s, i.e. the whole particle bed is completely flooded with water and T_{sat} is achieved throughout the particle bed.
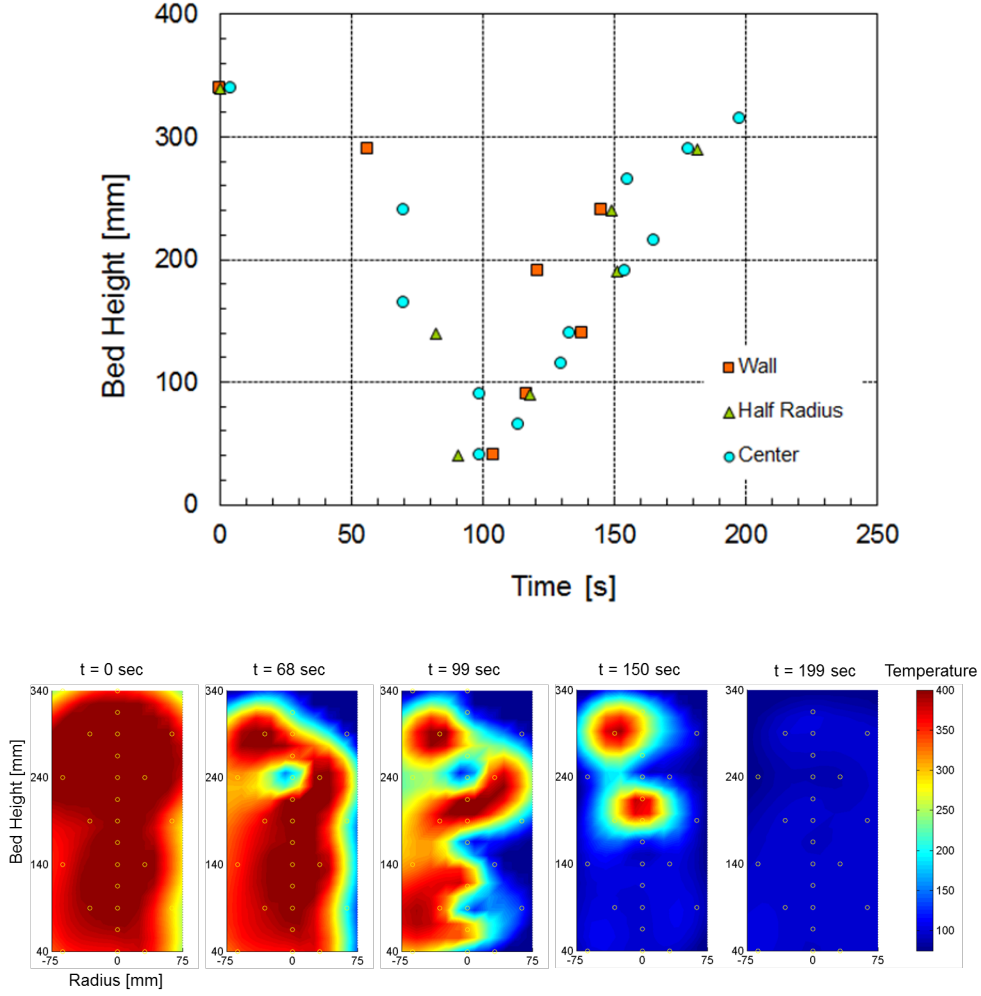
Figure 3.24: Quench-front progression and axial 2D temperature profile for IPB, 1D top-flooding, ($J_l^0 = 0$ mm/s, $T_{max} = 492$ °C, Table 2-6).

(II) ***1D bottom-flooding (water supply from the bottom using a pump, forced inflow)***

Polydispersed particle bed, forced inflow via pump

Figure 3.25 shows chronologically axial quench front progression (bed reached T_{sat}) along the bed height corresponding to three different measurement points in the bed cross section (wall, half radius and center of the particle bed). Furthermore representative axial 2D temperature profiles are also shown at certain time steps during the flooding from the bottom via pump (bottom-flooding, forced flow) at constant liquid superficial velocities $J_l^0 = 1.9$ mm/s and 2.3 mm/s (corresponds to a volumetric flow rate of 2 l/min and 2.4 l/min respectively) and the corresponding maximum initial temperatures

$T_{max} = 445$ °C and 745 °C) (see Figure 3.26). In case of bottom-flooding with forced flow conditions, generally, the quench front proceeds from bottom to top uniformly over the whole cross section of the bed. As compared to the top-flooding experiments the quenching is more of one dimensional in nature. As discussed in previous section the near-wall regions quench (reach T_{sat}) faster than the core regions of the particle bed (see Figures 3.25 and 3.26). Here a mean quench time delay of about 20 s and more is observed from the three measurement points (wall, half-radius, and center of the bed see Figures 3.25 and 3.26).
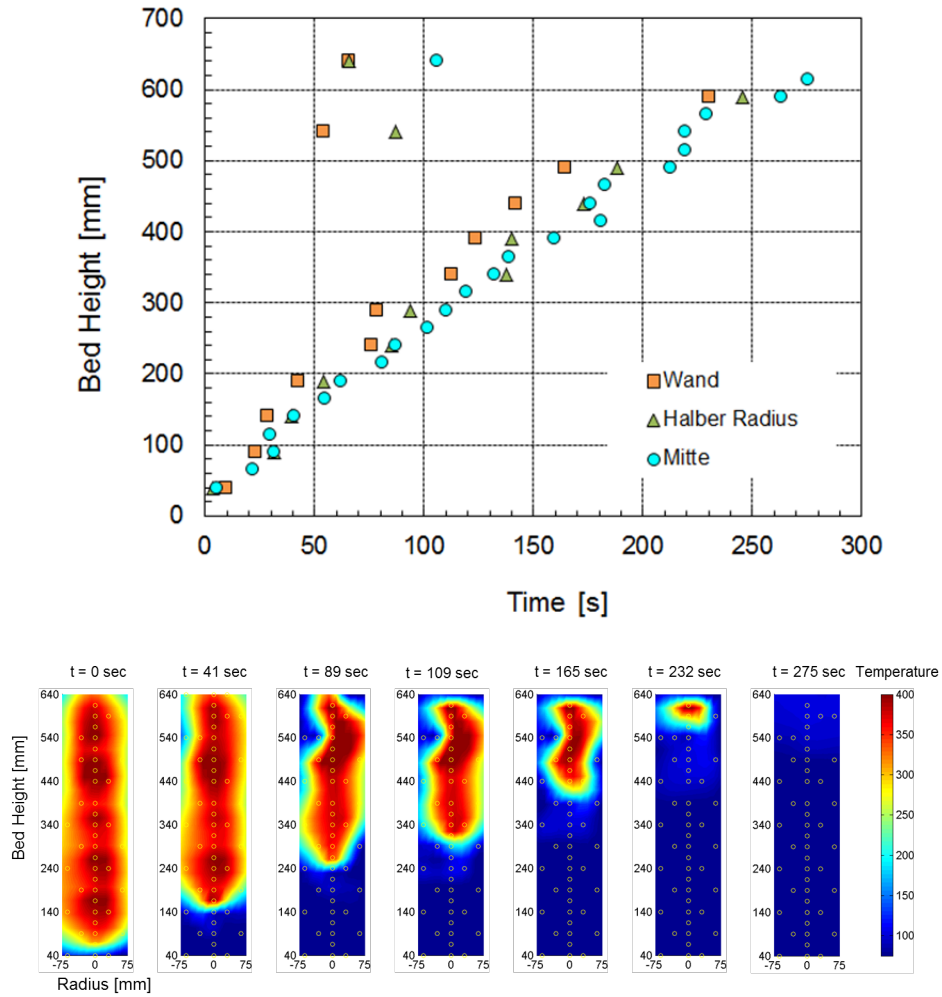
Figure 3.25: Quench-front progression and 2D temperature profile, polydispersed particle bed , 1D bottom-flooding with pump, ($J_l^0 = 1.9$ mm/s,$T_{max} = 445$ °C, Table 2-6).

In addition to this global cooling characteristic, localized cooling zones in the upper section of the particle bed, preferably near the wall, can be observed. The local cooling zone occurs, generally, within the first 100 s of start of flooding and typically remains

unaffected during the further flooding progression (see temperature profiles Figure 3.25; bed height 540 mm, $t = 89$ s, 109 s, 165 s, and Figure 3.26; bed height of 540 mm, $t = 43$ s, 160 s, 245 s). Similar to top-flooding case this can be explained by a fast, streak like penetration of water (driven by the feed pumps) from bottom to top. After water reaching a certain position inside the bed a stagnant phase follows. One explanation for this could be that a state of equilibrium, between the inflowing water and the generated vapor in that section of the bed, is achieved and thus no excess coolant is available for further quenching of surrounding bed sections.
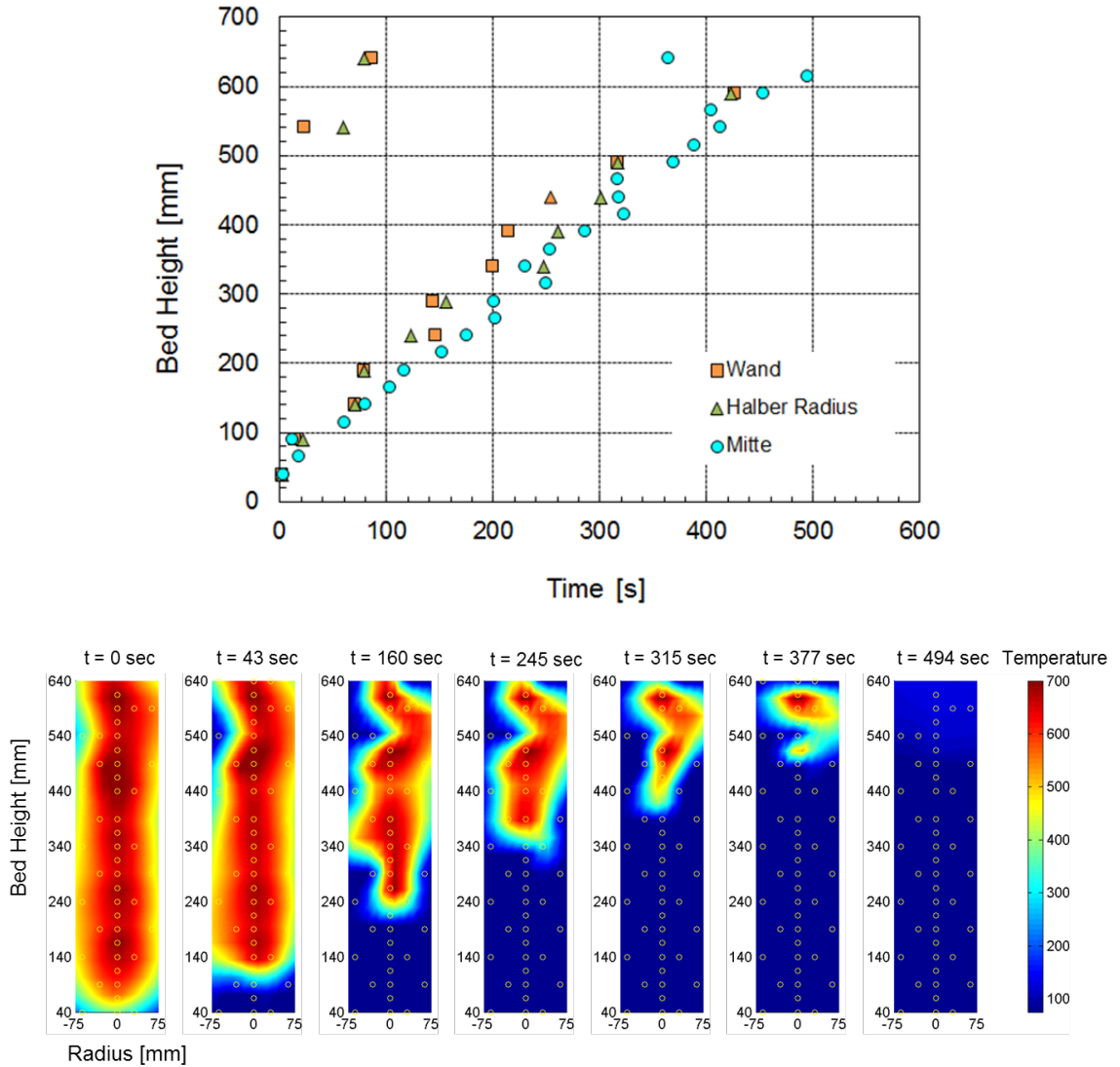
Figure 3.26: Quench-front progression and 2D temperature profile, PDB, 1D bottom-flooding with pump, ($J_l^0 = 2.3$ mm/s, $T_{max} = 745$ °C, Table 2-6).

Irregular particle bed, forced inflow via pump

Figures 3.27 and 3.28 present the quench results for irregular particle bed (IPB) with reduced bed height of 340 mm under bottom-flooding condition via pump with a constant inlet superficial velocity $J_l^0 = 2.3\ mm/s$ and the maximum initial bed temperature $T_{max} = 416\ °C$ and $T_{max} = 527\ °C$. The saturation temperature is mostly reached in the near-wall regions faster than the rest of the bed and is followed by the half radius bed sections and at the end in the center of the bed. In direct comparison with the polydispersed particle bed under the similar inflow conditions, overall the quench front progression curves (at three different measurement positions, wall, half radius and center) show similarities in qualitative behavior to the ones obtained for polydispersed particle bed (see also Figures 3.25 and 3.26 with the corresponding discussion). In case of irregular particle bed the cool down behavior in near-wall regions is more pronounced than that for polydispersed particle bed, particularly for higher initial bed temperature $T_{max} = 527\ °C$ at times $t = 50\ s$ and $100\ s$ (see also Figures 3.25 and 3.26. To understand such characteristic more pronounced behavior, compared to polydispersed particle bed, it is important to take into consideration the slightly higher bed porosity of the irregular particle bed and the temperature boundary conditions. Relatively poor inductive heat generation by the irregular particle bed, combined with the radial heat losses, results in larger radial temperature gradients thereby enhancing the coolant flow in the near-wall regions. In consideration of the time based quench front progression, for example at the measurement positions "center", there is a somewhat faster quench front progression for irregular particle bed than that for polydispersed particle bed. Moreover, an increased surface area by the irregular shape of the Al_2O_3 particles combined with relatively higher bed porosity result in a better and quicker heat dissipation. The overall quench time for the bed with initial temperature $T_{max} = 416\ °C$ is about $100\ s$ (see Figure 3.27) and with $T_{max} = 527\ °C$ in about $127\ s$ (see Figure 3.28).
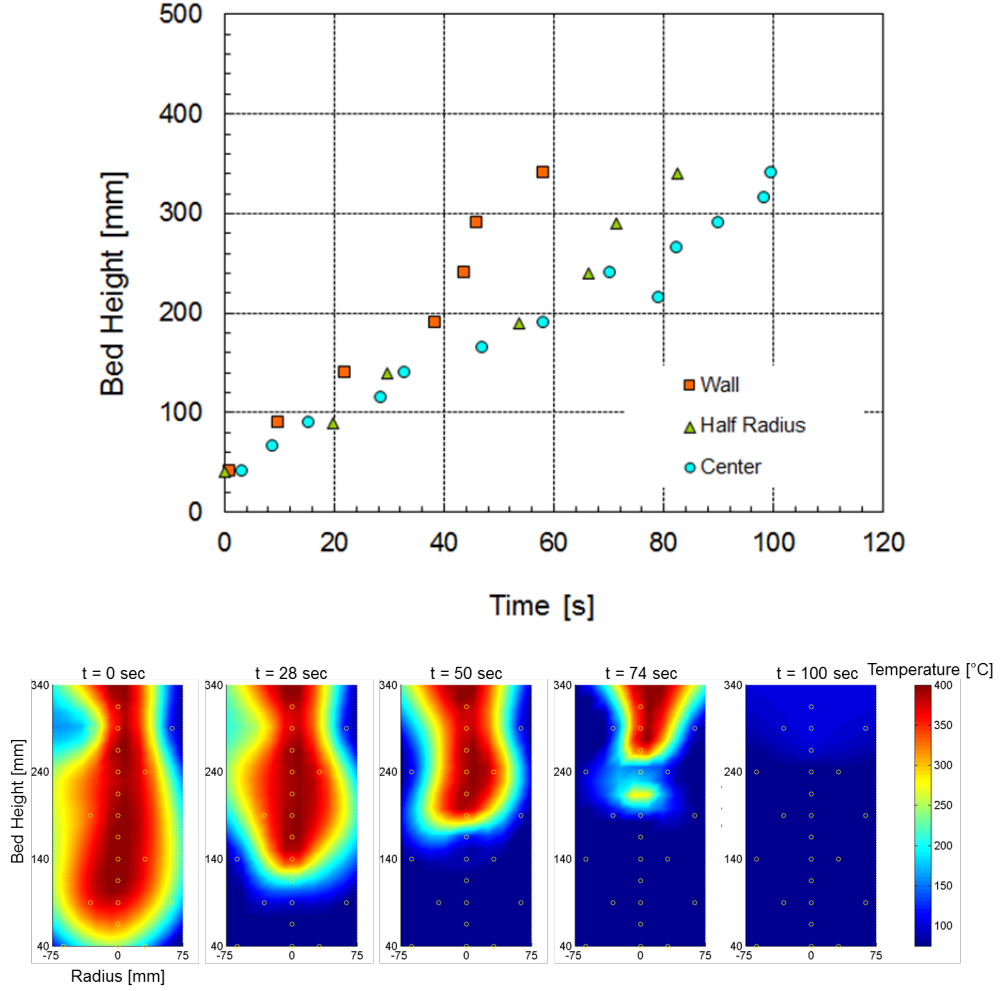
Figure 3.27: Quench-front progression and axial 2D temperature profile for IPB , 1D bottom-flooding with pump, ($J_l^0 = 2.3\ mm/s$, $T_{max} = 416$ °C, Table 2-6).

Polydispersed particle bed, hydrostatic head via water tank

In case of bottom-flooding via water tank, the water is fed into the bottom of the particle bed from an over lying water tank via an external downcomer under hydrostatic head. At beginning the quench front progression is relatively fast and slows down with time due to the rising water level inside the crucible which equates more and more the hydrostatic head of the water storage tank. The pressure constraint at the water inlet of the particle bed mainly differentiates this flow condition from the forced bottom-flooding condition (flow configuration (II), with pump). Under forced inflow condition the heated particle bed is flooded with predetermined constant mass flow at constant feed pressure and thus during quenching, to a certain extent, is independent of the pressure development inside the particle bed.
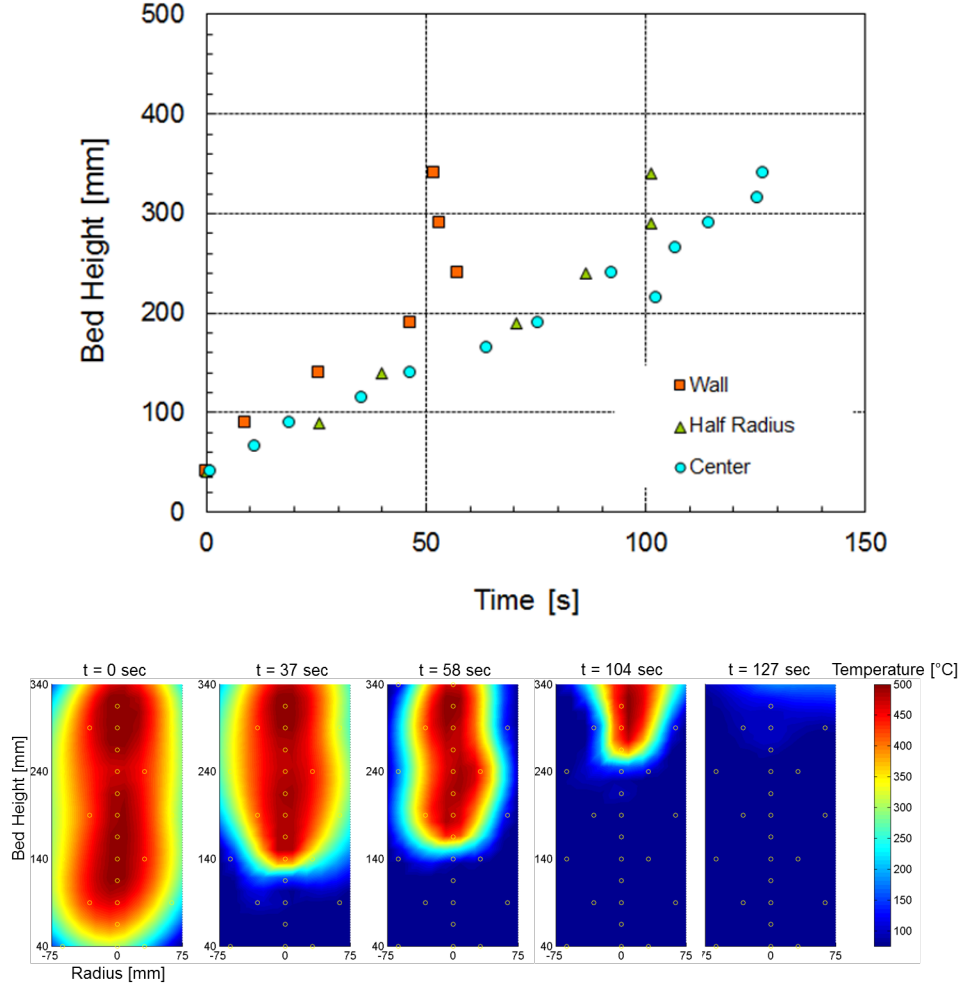
Figure 3.28: Quench-front progression and axial 2D temperature profile forIPB , 1D bottom-flooding with pump, ($J_l^0 = 2.3\ mm/s$, $T_{max} = 527\ °C$, Table 2-6).

For bottom-flooding under hydrostatic conditions the feed rate is coupled directly with the pressure build-up by evaporation and frictional pressure losses in the bed. This results in a variable water inflow over the whole quenching period and is significantly controlled by the pressure difference between the pressure at the bottom of the particle bed and the height of the hydrostatic column. In Figures 3.29 and 3.30 the quenching results of polydispersed particle bed with initial temperature $T_{max} = 447\ °C$ and $T_{max} = 725\ °C$ are shown. Both results show a relatively uniform, linearly increasing flood front line. This also shows a great similarity with the quenching experiments under forced flow condition (feed pump), in particular, after start of the flooding the wall regions in the upper bed section of the particle bed are quenched faster than rest of the section at the same height. Similar to forced bottom-flooding condition, the formation of such local cooling effect in
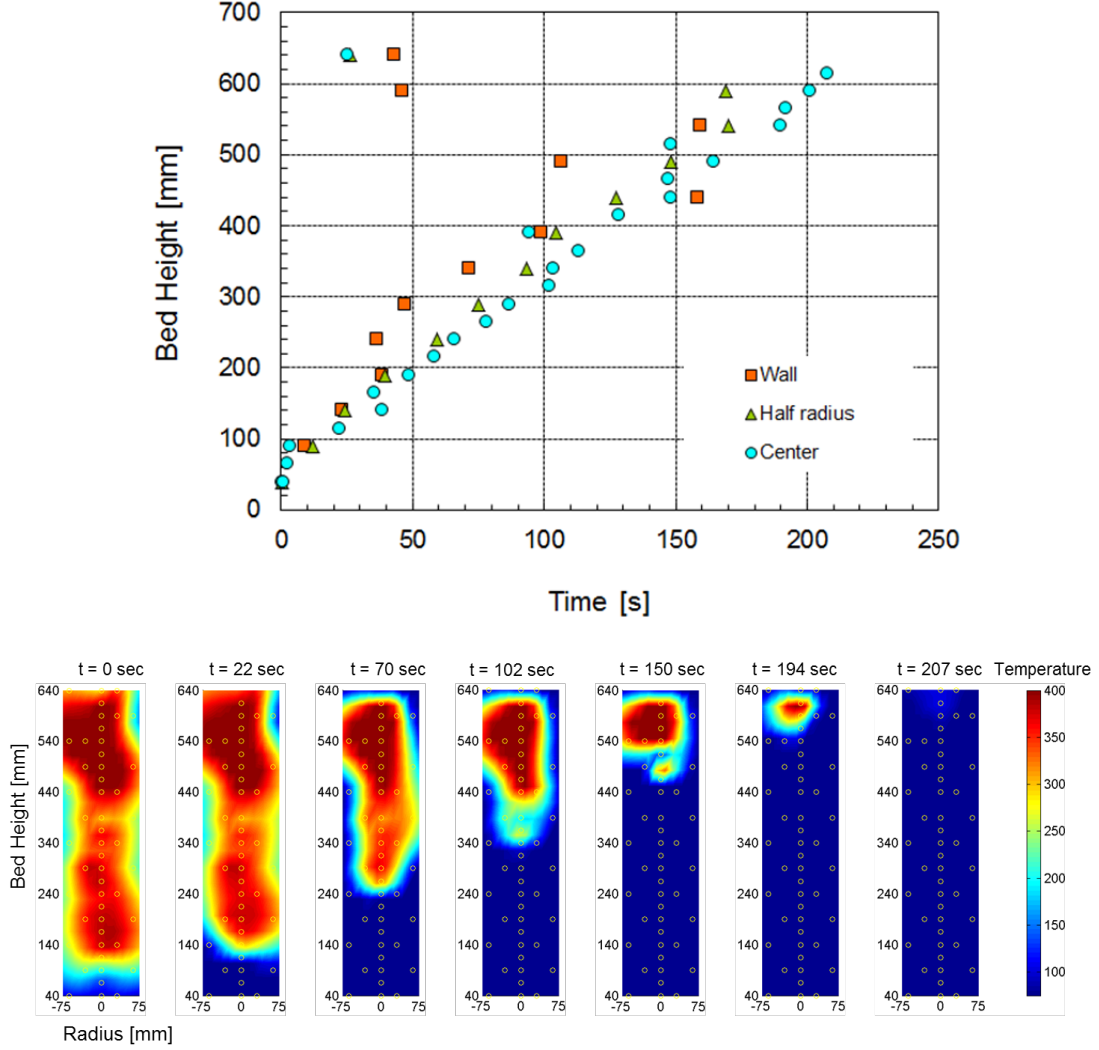
Figure 3.29: Quench-front progression and 2D temperature profile, PDB, 1D bottom-flooding under hydrostatic head (external downcomer), ($T_{max} = 447$ °C, Table 2-6).

the upper section of the particle bed are driven by relatively faster coolant progression in the near-wall regions. The difference in overall quenching time for two different initial bed temperature profiles (see Figures 3.29 and 3.30) can be explained by the difference in stored thermal energy in the particle bed. Thus for higher initial bed temperatures more coolant for the evaporation and hence more time is required for the heat removal. Also, provided comparable liquid inflow rates, less liquid is available for the development of local flow paths to the upper bed section. Both these effects also result in a delayed quenching in the near-wall regions for higher initial bed temperatures. The overall quench time for the bed with initial temperature $T_{max} = 447$ °C is about 210 s (see Figure 3.29) and with $T_{max} = 725$ °C about 435 s (see Figure 3.30).
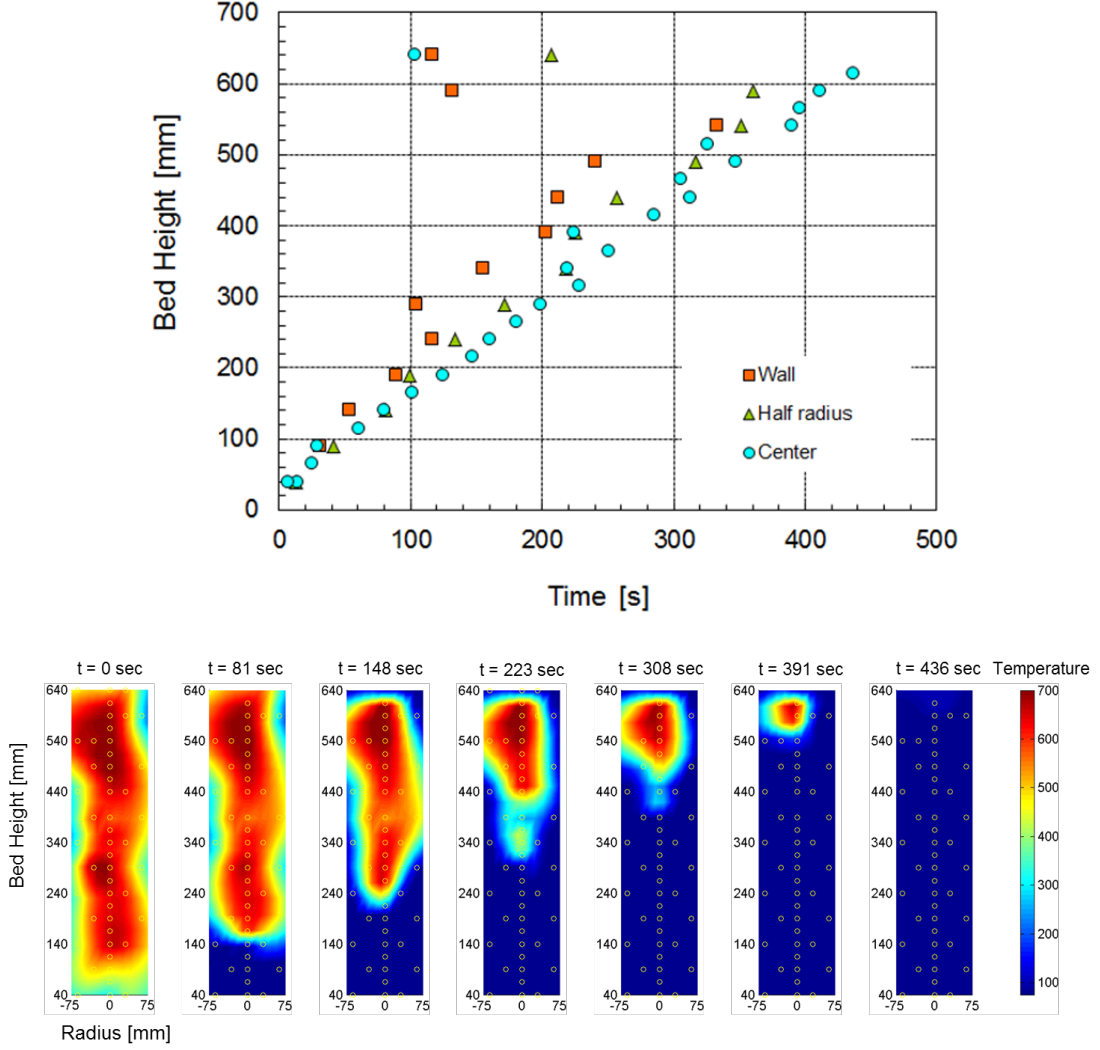
Figure 3.30: Quench front progression and 2D temperature profile, PDB, 1D bottom-flooding under hydrostatic head (external downcomer), ($T_{max} = 725$ °C, Table 2-6).

Irregular particle bed, hydrostatic head via water tank

Figures 3.31 and 3.32 represent the quenching experimental results for irregular particle bed with flooding from the bottom (bottom-flooding) under hydrostatic head via an overlying water tank. As can be seen from the time based quench front progression and 2D temperature profiles, the near-wall bed regions quench (reach $T_{sat} = 100$ °C) within a few seconds (about 12 s at $T_{max} = 442$ °C, about 21 s at $T_{max} = 530$ °C) up to the top of the bed. The quench front progresses in the remaining part of the particle bed (half radius and center) over a relatively uniform manner. Such quench front progression behavior has already been discussed in earlier results with similar flow conditions for polydispersed

particle bed (bottom-flooding via pump and via tank) as well as for irregular particle bed (1D bottom-flooding via pump).

Additionally, at time $t = 40$ s and bed height 240 mm an increase in quench front velocity at the half radius measurement positions has been observed. This increase in quench velocity is more prominent for the case of initial bed temperature $T_{max} = 442$ °C than the one for $T_{max} = 530$ °C (see Figures 3.31 and 3.32). The quench front progression remains smooth and continuous. The overall quench time for both initial bed temperatures $T_{max} = 442$ °C and $T_{max} = 530$ °C is about 60 s, which is much lower than those observed (100 s and 127 s respectively for comparable initial bed temperatures) for forced (via pump) bottom-flooding. As compared to the quench times for bottom-flooding via pump, the reduction in quench times under hydrostatic head has also been observed for polydispersed particle bed but in smaller magnitudes. The possible reasons for this, as also discussed in earlier results, are in addition to the radial temperature gradients, the overall slightly higher bed porosity and expected higher porosity in the near-wall regions of the particle bed.
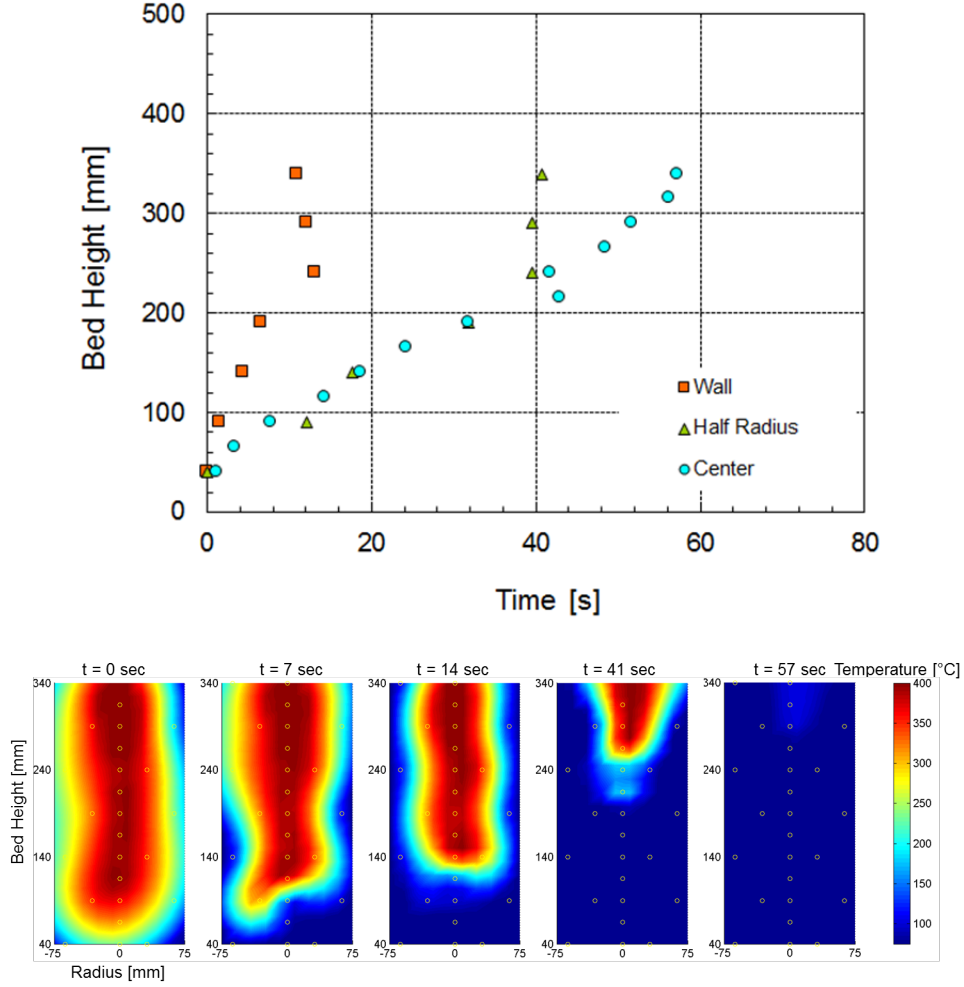
Figure 3.31: Quench-front progression and axial 2D temperature profile, IPB, 1D bottom-flooding under hydrostatic head (external downcomer), ($T_{max} = 442$ °C, Table 2-6)

(III) *1D top-/bottom-flooding (water supply from the top and bottom via internal downcomer, natural circulation)*

Quenching experiments with internal downcomer configurations (flow conditions (III) and (IV)) were carried out with a reduced bed height (see Section 2.1.2.2).

Polydispersed particle bed with an internal open downcomer

Figure 3.33 shows the time-based quench front progression for a polydispersed particle bed with an initial temperature $T_{max} = 447$ *celsius*. An internal downcomer is installed in the center of the particle bed and the bed, after preheating, is flooded from the top. As compared to the particle friction inside the particle bed, the open downcomer offers, relatively, low friction path to the downward water flow. This results in a combination
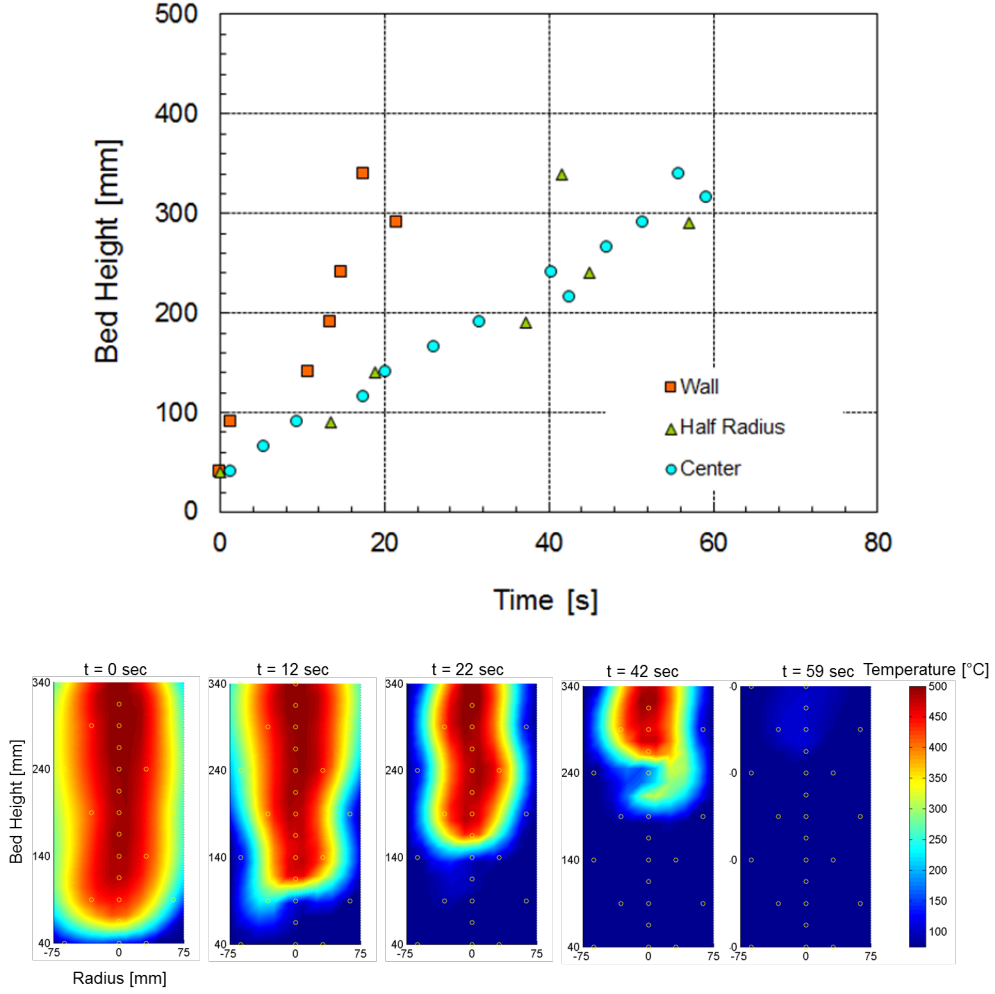
Figure 3.32: Quench-front progression and axial 2D temperature profile, IPB, 1D bottom-flooding under hydrostatic head (external downcomer), ($T_{max} = 530\ °C$, Table 2-6).

of both top- and bottom-flooding situation inside the particle bed. After flooding the bed with coolant a 200 mm high water pool is formed above the particle bed. Initially only the highest measurement position in the bed (at $h = 200\ mm$) indicate saturation temperature and coolant water does not ingress further into the lower parts of the bed for a few seconds. This can be attributed to the resistance to the water flow offered by the steam generated by the hot particle bed which flows upwards and counters the downward flow of water. Only after a few seconds ($t = 16\ s$) the whole cross section of the bed, at a measurement level of 20 mm, reaches saturation temperature, followed in time by the bed height 60 mm ($t = 28\ s$), 100 mm ($t = 46\ s$). Similar to pure top flooding, after initial flooding, the water flood front progresses continuously from bottom to top and leading to co-current flow inside the particle bed. The near-wall regions of the particle bed are

always quenched a little earlier than further inside areas half radius bed or in the bed center. Figure 3.34 shows the axial 2D temperature distribution in the particle bed, over the whole cross section, at three different bed heights ($h = 20\ mm$, $100\ mm$ and $180\ mm$). Flooding starts at time $t = 0\ s$ (bed is on initial temperature), and after 3 s local quenching takes place at the near-wall regions at a bed height of $h = 180\ mm$, which up to the time $t = 16\ s$ continues to expand, under top-flooding conditions, to the rest of the bed regions at the same height. At time step $t = 19\ s$ reheating of the upper bed regions is observed. This can be explained by the fact that, once water reaches the bottom bed regions more steam is generated, which moves upwards and in turn pushes the water out of the bed. The loss of water inventory in the upper regions, the convective heat transfer between the superheated steam (moving upwards) and the quenched particle bed result in a dryout and reheat of the upper region of the particle bed.

At $t = 16\ s$ the quench front has reached a bed height of $h = 20\ mm$ and already large near-wall particle bed areas have cooled down to the saturation temperature. At $t = 19\ s$ the whole cross-section is quenched. Thereafter, the quench front reaches the next measurement level at height $h = 100\ mm$, cooling it to saturation temperature. Finally (at $t = 78\ s$), the upper bed sections are symmetrically quenched from outside to the inside as indicated by the thermocouples at a measurement level of bed height $h = 180\ mm$ again radially symmetrical cooled from the outside to the inside. The quenching process is completed at time $t = 86\ s$, i.e. the whole particle bed is completely flooded with water and T_{sat} is achieved throughout the particle bed.
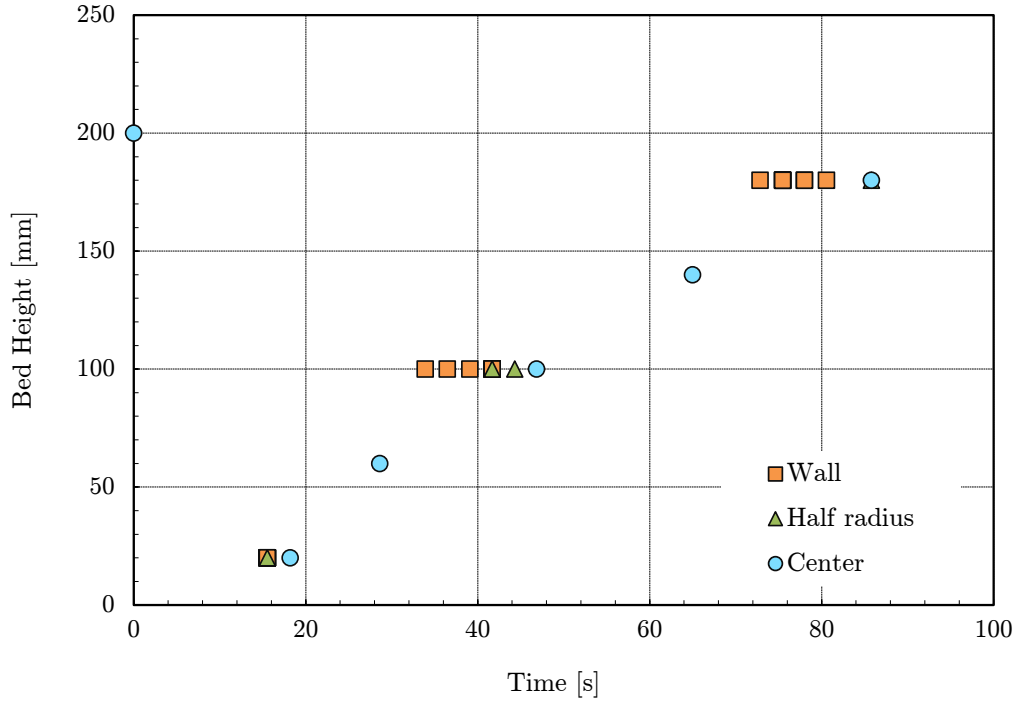
Figure 3.33: Quench-front progression at different bed heights for PDB, 1D top-/bottom-flooding with an internal open downcomer, ($T_{max} = 447°$C, Table 2-6).

Irregular particle bed with an internal open downcomer

Figures 3.35 and 3.36 represent the time based quench front progression and 2D temperature profiles of the quenching experiment for an irregular particle bed (initial bed temperature $T_{max} = 451$ °C) with an open downcomer installed in the center of the particle bed. The preheated particle bed is mainly flooded from top. The flood front progression takes place in two stages, where in during first stage the water mainly flows downwards along the near-wall regions and via open downcomer which offers a low resistance flow path to the water. The first stage is dominant by counter-current flow situation, where water flows downwards and the generated steam moves upwards, inside the particle bed (see Figure 3.36, $t = 4$ s and 12 s at a bed height of $h = 180$ mm and $h = 100$ mm respectively). From Figures 3.35 and 3.36 is also visible that the water does not flow over the whole cross section rather only in the near-wall regions and hence the counter-current between two phases must also exists only in the near-wall regions. In parallel the water also flows downwards via, concentrically installed, open tubular downcomer.
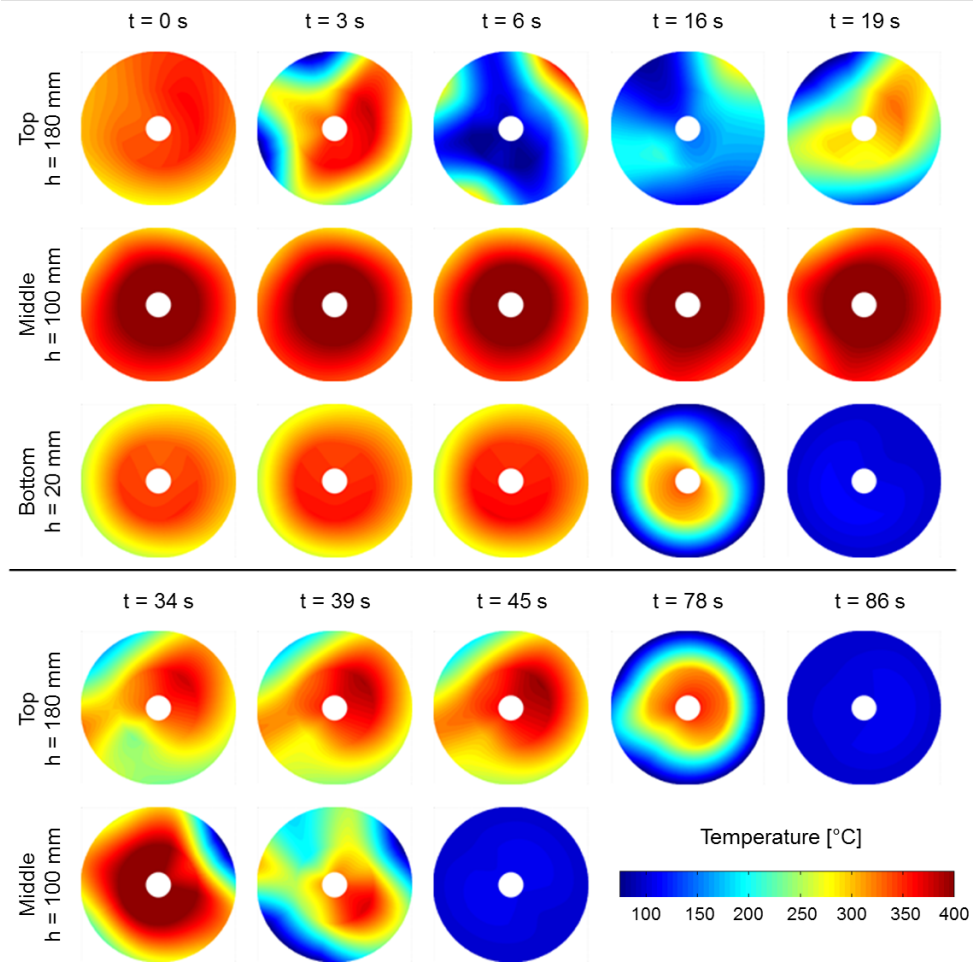
Figure 3.34: Axial 2D temperature profile for PDB, 1D top-/bottom-flooding with an open downcomer, ($T_{max} = 447°$C, Table 2-6).

(IV) *2D top-/bottom-/lateral-flooding (water supply from the top with a perforated downcomer)*

The flow conditions (flow conditions (I), (II) and (III)) discussed in the aforementioned sections have more of a 1D cooling characteristic where the fluid tends to flow in the axial direction (upwards and downwards). In experiments with a perforated downcomer, installed in the center of the particle bed, the fluid tends to flow not only in the axial direction but also radial direction. The perforated downcomer, in addition to, top-flooding (water supply from an overlying water pool) and bottom-flooding (via downcomer in the center) also leads to lateral-flooding (lateral flow via perforations in the downcomer), which in turn results in a more complicated 2D flow condition inside the particle bed. The aim of using the perforated downcomer, on one hand, is to simulate the more realistic flow situation, and on the other hand, is to enable the lateral water flow to the larger bed
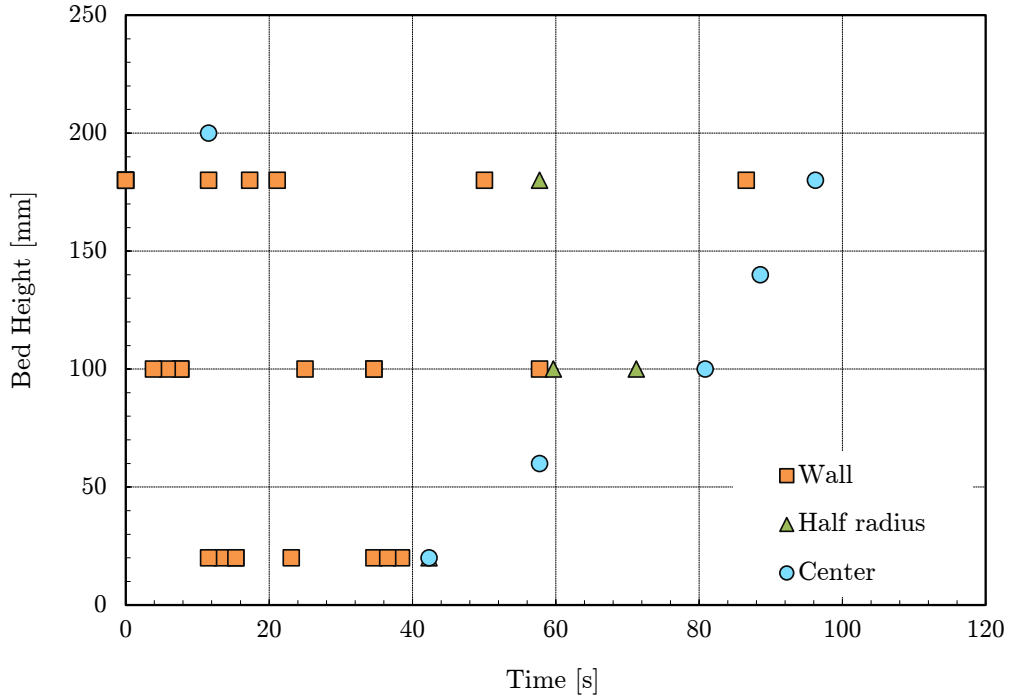
Figure 3.35: Quench-front progression at different bed heights for IPB, 1D top-/bottom-flooding with an internal open downcomer, ($T_{max} = 451\,°\mathrm{C}$, Table 2-6).

sections and hence enhance the coolability of the particle bed.

Polydispersed particle bed with perforated downcomer

Figure 3.37 shows the cool down (cooled to saturation temperature) behavior of the particle bed with initial temperature $T_{max} = 442\,°\mathrm{C}$. It is striking that within a short time ($t \leq 2\,s$) wide wall areas along the particle bed height have reached saturation temperature. After flooding the test section with water from top, within a short interval a water pool is formed above the bed. The coolant should preferably be supplied either from the water pooled formed above the hot particle bed (top-flooding), or from below (bottom-flooding) via the perforated tubular downcomer, . In this context, it is also important to take into account the fact that, due to the perforations in the downcomer and higher flow resistance to the steam generated inside the hot particle bed, the generated steam might follow the low flow resistance path offered by the downcomer and hence hindering the downward flow of coolant water. This would result in a relatively less coolant flow downwards into the bottom of the bed. At the same time the perforated downcomer also enables the lateral water ingression into different bed sections resulting in a more complex, as compared to pure top-, bottom-flooding, flow situation inside the particle bed. As compared to the
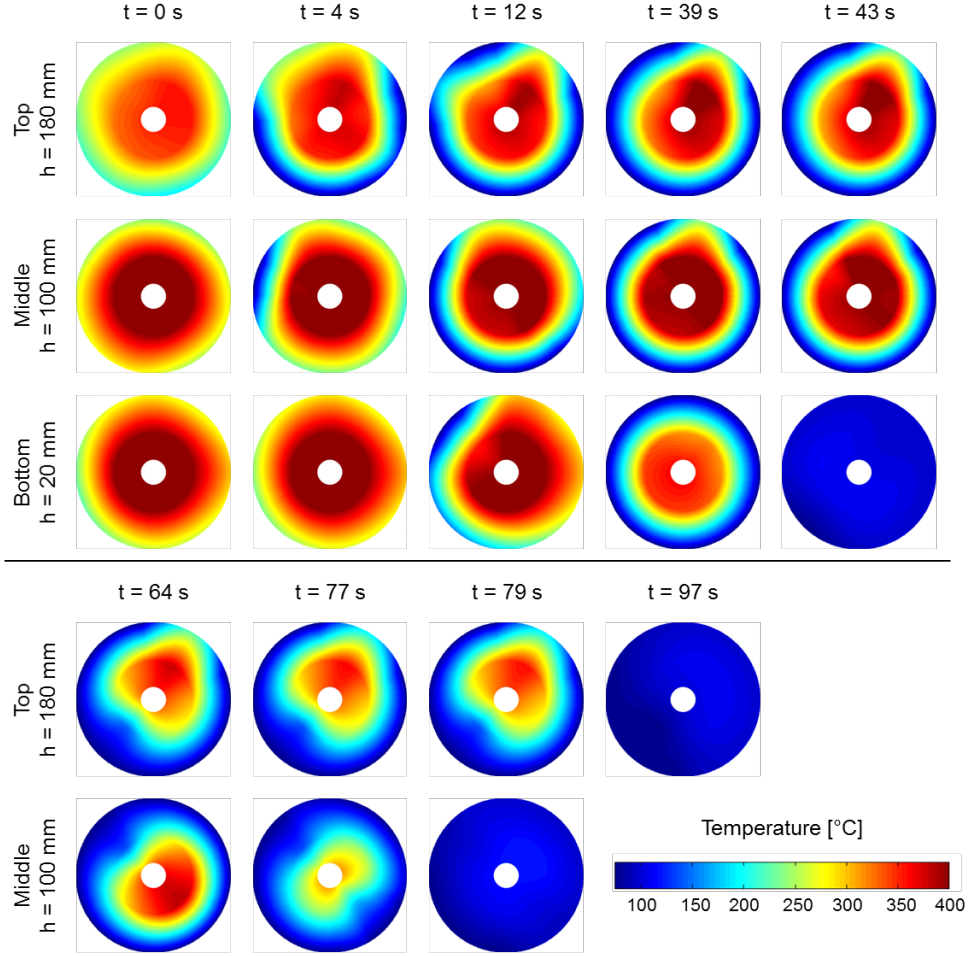
Figure 3.36: 2D temperature profiles in different bed heights for IPB, 1D top-/bottom-flooding with an open downcomer, ($T_{max} = 451$ °C, Table 2-6)

flooding with an open downcomer, where predominantly quench front moves from bottom to top, a parallel downward and upward quench front progression is expected.

Figure 3.38 shows the 2D temperature profiles in different bed heights and a relatively rapid cooling in the near-wall regions of the particle bed, in all three measurement cross sections, at time $t = 5\ s$ is visible. At time $t = 28\ s$, the lower sections of the particle bed reach saturation temperature ($h = 20\ mm$, bottom measurement plane). Subsequently at $t = 77\ s$, the temperature in the middle part of the bed also drops to the saturation temperature ($h = 100mm$, mid measurement plane). In contrast, in the upper bed sections ($h = 180\ mm$, top measurement plane) a relatively stagnant temperature profile is observed. The quenching process is completed at time $t = 102\ s$, i.e. the whole particle bed is completely flooded with water and T_{sat} is achieved throughout the particle bed.

Figure 3.37: Quench-front progression at different bed heights for PDB, 1D top-/bottom-/lateral-flooding with perforated downcomer, ($T_{max} = 442\ °$C, Table 2 4).

Irregular particle bed with perforated downcomer

Figures 3.39 and 3.40 represent the quench front progression over time and 2D temperature profiles of the quenching experiment for an irregular particle bed (initial bed temperature $T_{max} = 439\ °$C) with a perforated downcomer installed in the center of the particle bed. The perforated downcomer concept is quite similar to the open downcomer flow case.

The major difference is that the perforated downcomer, in addition to downward and upward flow, facilitates the lateral flow of water to different bed sections. The lateral flow should possibly lead to an overall improved coolant distribution in the bed and in consequence to a more rapid flooding of different bed regions which, in case of top-, bottom-flooding scenario, are usually flooded only at a later stage of quenching. The measured data indicate significant similarities to the experimental results of the open downcomer configuration(Figure 3.39) as well as the same flow configuration (perforated downcomer) for the polydispersed particle bed (Figure 3.37).

The quench front progression is controlled by different flow conditions at different stages of the quenching. In case of perforated downcomer, in addition to the downward
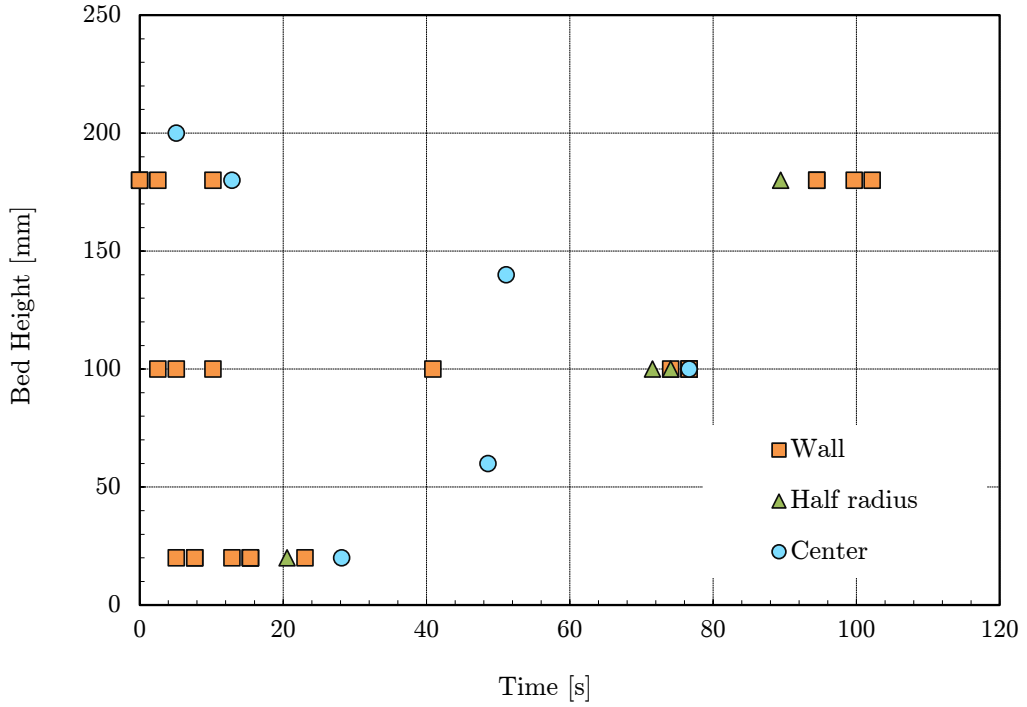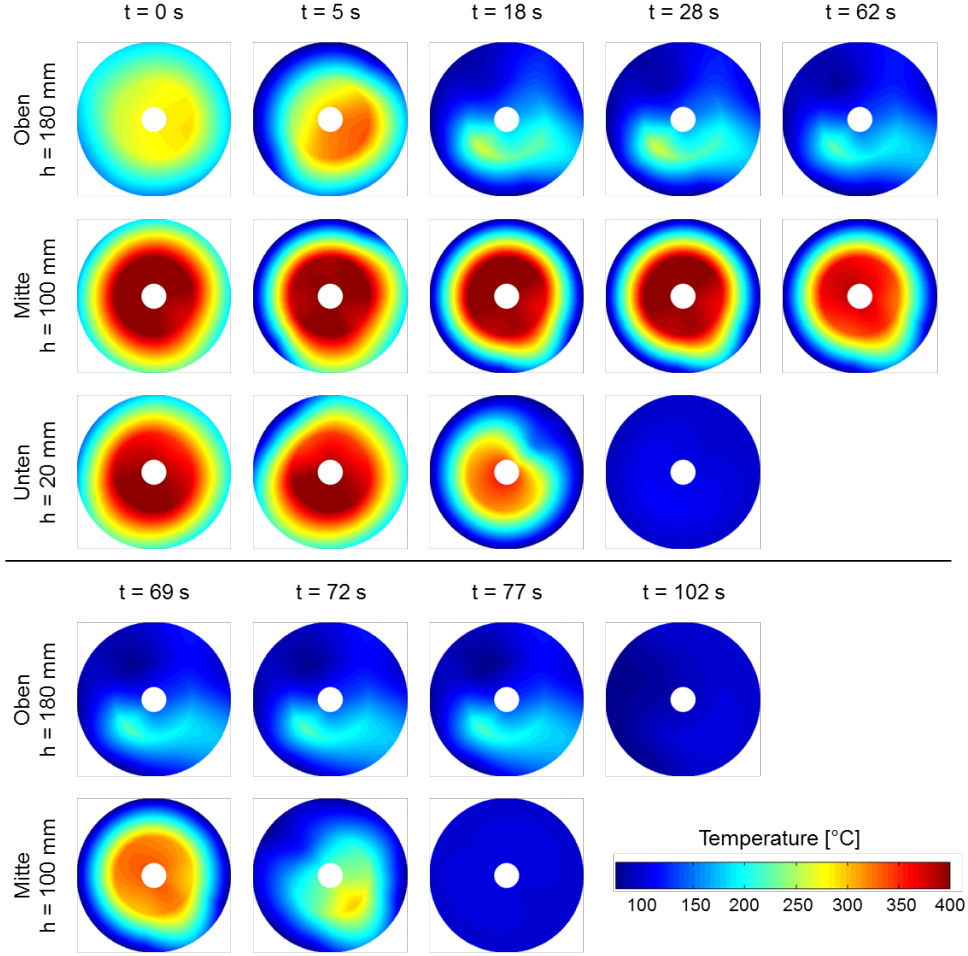
Figure 3.38: 2D temperature profiles in different bed heights for PDB, 1D top-/bottom-/lateral-flooding with perforated downcomer, ($T_{max} = 442\,°C$, Table 2-4).

flow in the near-wall regions and via tubular downcomer the water will also flow laterally into different bed sections. In early stage of the quenching mainly the near-wall regions reach the saturation temperature dominated by top-flooding (counter-current flow). This is followed by quenching of the rest of the bed and is mainly dominated by bottom-flooding (co-current flow). For some time both co- and counter-current flow co-exist inside the particle bed but towards the later stage of the experiment the quench front progression is mainly dominated by co-current flow (see Figures 3.39 and 3.40). The quenching process is completed at time $t = 98\,s$, i.e. the whole particle bed is completely flooded with water and T_{sat} is achieved throughout the particle bed.

Figure 3.39: Quench-front progression at different bed heights for IPB, 1D top-/bottom-/lateral-flooding with perforated downcomer, ($T_{max} = 439$ °C, Table 2-4).

Quench Times

The duration of quenching process is determined from the stored thermal energy, water influx and the resulting evaporation rate, which specifies how much heat per unit time can be removed from the particle bed. The greater the stored thermal energy is, the more coolant and time is necessary to remove this heat by means of evaporation. A brief discussion of the determined quench times for different particle beds (PDB and IPB) under different flow conditions is given below.

Polydispersed particle bed

Figure 3.41 summarizes the comparison of the quench times for different flow conditions (top-flooding, bottom-flooding (hydrostatic head and fixed flow rates via pump)) for different initial temperature profiles (T_{max}). The quench times, at comparable temperature profiles (T_{max}), for top-flooding flow are more than 2 times higher than those for bottom-flooding under hydrostatic head (415 s / 935 s ($T_{max} = 432$ °C/747 °C) to 210 s / 435 s ($T_{max} = 441$ °C/ 725 °C)). For bottom-flooding with fixed inflow rates (via pump)
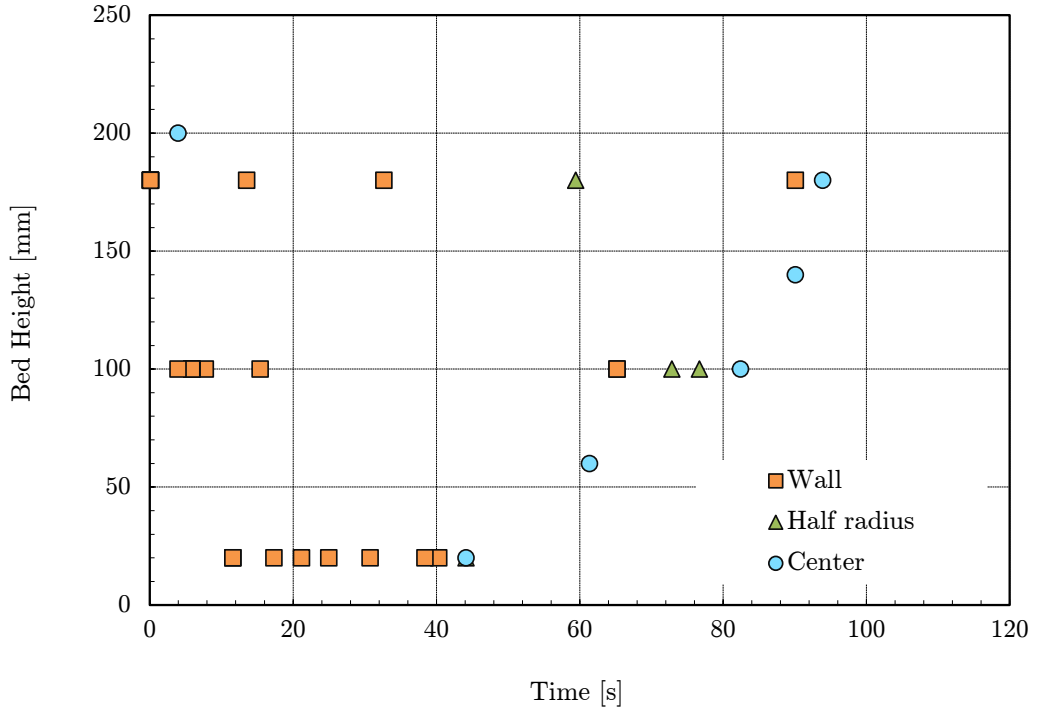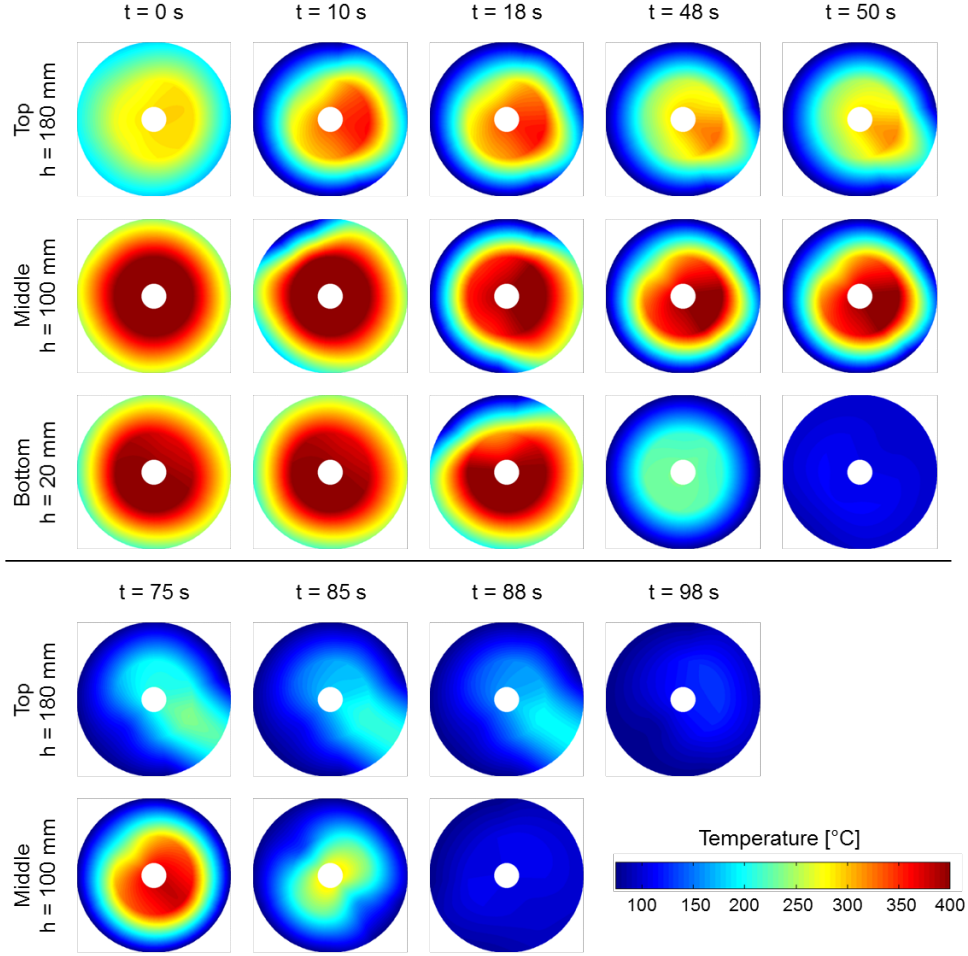
Figure 3.40: 2D temperature profiles in different bed heights for IPB, 1D top-/bottom-/lateral-flooding with perforated downcomer, ($T_{max} = 439$ °C, Table 2 4).

the corresponding quench times are 275 s ($T_{max} = 445$ °C) and 495 s ($T_{max} = 745$ °C), and are thus in the order of the quench times for bottom-flow under hydrostatic head.

For quenching process with different flow conditions, in addition to quantitative differences, qualitative differences have also been observed. For experiments with bottom-flooding flow conditions a linear relationship between the initial temperature profiles (T_{max}) and the quenching time has been observed. For top-flooding flow conditions, with increase in bed temperature and the associated increase in steam production by the particle bed, the counter-current flow situation between the liquid water and the steam makes it difficult for the coolant water, needed for evaporation and heat dissipation, to penetrate into the particle bed. Thus, per unit of time less heat is to be dissipated and hence the particle bed takes longer to quench to the saturation temperatures. Under co-current conditions with bottom-flooding, as long as sufficient water is provided for evaporation,
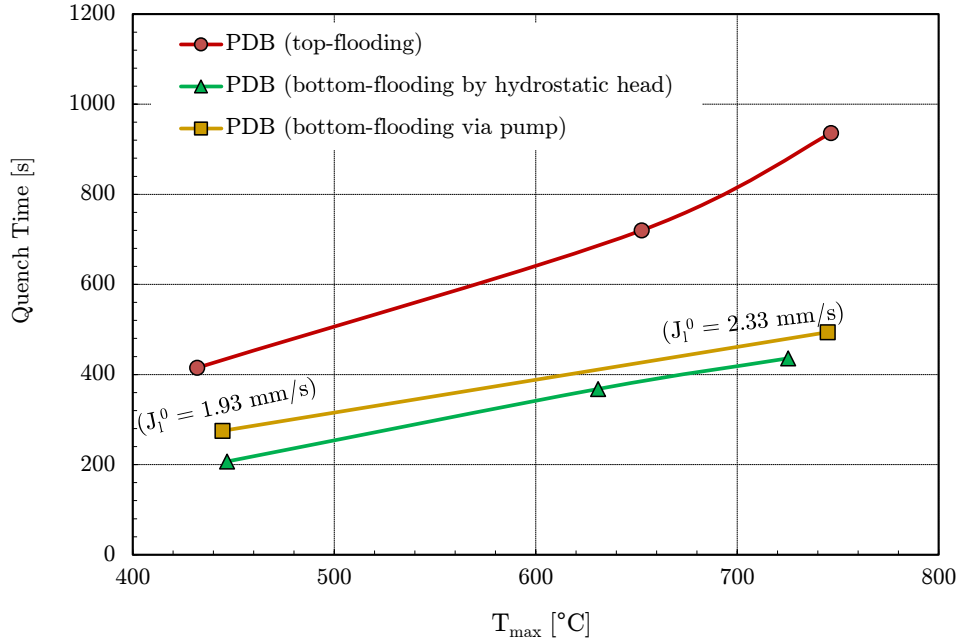
Figure 3.41: Comparison of quench times for PDB, (1D top-flooding, bottom-flooding (hydrostatic head and fixed flow rates via pump), different initial temperature profiles (T_{max})

the vapor flow does not obstructs the liquid flowing in the same direction, and the quench times are in a proportional relation to the dissipated heat energy. In general terms it can be concluded that the dry, superheated particle beds are better quenched with water being fed into the bottom (bottom-flooding) of the particle bed than being only supplied from the top (top-flooding), i.e. in given time interval more thermal energy can be transported from the particle bed and the particle bed is faster cooled down to saturation temperatures.

In Table 3.2, the quench times determined from quenching experiments for flow conditions with open downcomer and perforated downcomer are given. As mentioned in earlier paragraphs, with increasing initial temperature profiles (T_{max}) the quench time is also increased. Comparing the data with each other for above mentioned flow conditions (open- and perforated downcomer flow conditions), it can be seen that the superheated particle bed for perforated downcomer flow condition, despite having slightly lower bed temperatures (T_{max}), takes longer time to quench than that for open downcomer flow condition. This result has the similar trend as in the case of boiling/dryout experiments for perforated downcomer in which, contrary to expectations, deterioration of coolability of the particle bed with respect to the flow condition with open downcomer was also observed (see Section 3.2). Due to reduced bed height for experiments with open- and perforated

Table 3.2: Overview of quench times, PDB, open downcomer and perforated downcomer (see also Table 2-3), different initial temperature profiles (T_{max})

Test No.	T_{max} [°C]	Quench Time [s]
(III) 1D top-/bottom-flooding, (water supply from top and bottom via internal, natural circulation)		
1	333	63
2	340	76
3	447	86
4	457	94
5	459	94
(IV) 2D top-/bottom-/lateral-flooding (water supply from top with perforated downcomer)		
1	396	94
2	422	102

downcomer case, a direct overall quantitative comparison between all the experiments with different flow conditions could not be made. Under a very strong simplified assumption of a linear relationship between the bed height to be flooded and the quench time, corresponding difference of the bed height would be of a factor of 3. For the assumed bed height and the comparable bed temperature conditions, the extrapolated quench times of Table 3.2 would be approximately 270 s for internal open downcomer flow condition (III) and 300 s for perforated downcomer flow condition (IV). These are thus between the quench times of the top-flooding and bottom-flooding under hydrostatic head flow conditions, which seems plausible. However, no generalized statement can be made only based on this extrapolation comparison rather can only be seen as a first qualitative indication for the classification of results. In any case to make clear and reliable statements more experimental data are needed, which unfortunately due to time and cost limitation could not be achieved within the framework of the present work.

Irregular particle bed

Figure 3.42 shows the comparison of quench times for different flow conditions (top-flooding, bottom-flooding (hydrostatic head and fixed flow rates via pump)) for different initial temperature profiles (T_{max}). Due to technical limitations (thermomechanical problem with the main test section) of the experimental setup, quenching experiments with irregular particle bed were carried out with a reduced bed height. For generalized interpretation and the respective clear conclusion more experimental data with increased bed

height are needed which unfortunately within the time frame and scope of this research work could not be achieved.
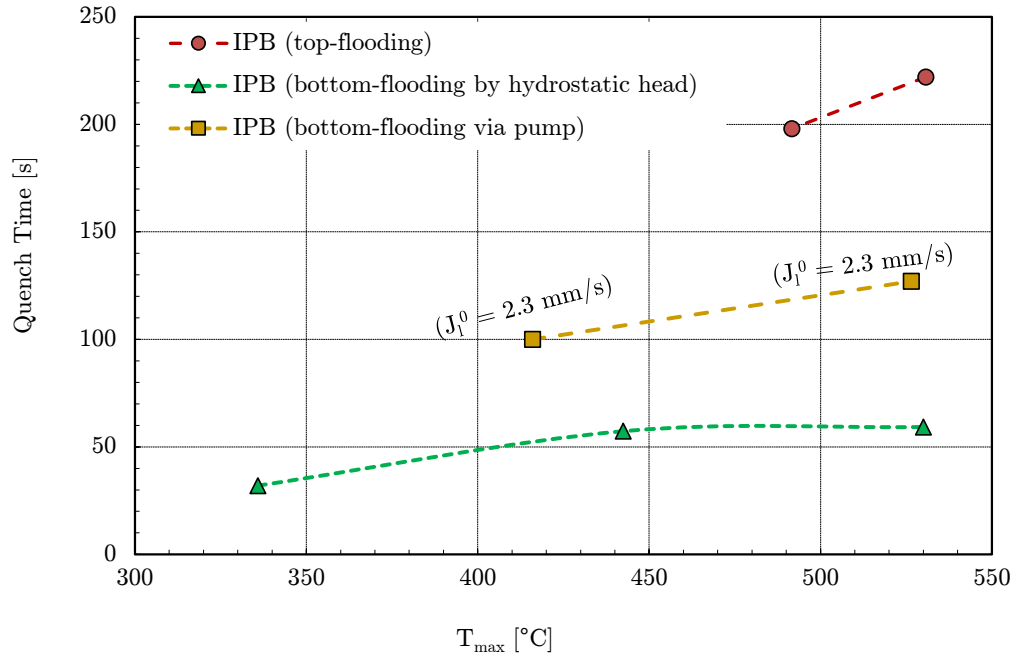
Figure 3.42: Comparison of quench times for IPB, (1D top-flooding, bottom-flooding (hydrostatic head and fixed flow rates via pump), different initial temperature profiles (T_{max})

3.5 Uncertainty Analysis

In terms of experimental results the quality of the measurements is generally defined in terms of uncertainties. An important aspect of experimental work is to report the inevitable uncertainties in the experimental data. In general the aim of the uncertainity analysis is to study and evaluate the measurement uncertainties. Reproducibility and accuracy of the measurements are the key components of the uncertainity analysis. In this section a brief description of general error analysis for key measurements is given.

3.5.1 Pressure Measurements

For pressure measurements piezo resistive differential pressure transmitters (Keller PD23 series) were used. As described by the manufacturer the pressure sensors have a measuring range of 100 $mbar$ and an accuracy class 0.1 %, that, the absolute maximum error in the pressure measurement is 0.1 $mbar$. Each pressure transducer is installed over a 100 mm bed section. This, from the perspective of measurement technology, results in a maximum error of 100 Pa/m in the differential pressure measurement. This value is significantly lower than the fluctuations observed in the experiments. The pressure measurement for both single phase and two phase flow experiments showed fluctuations in the measured pressure data which were beyond the accuracy range of the transducer. The single phase flow experiments were repeated with good reproducibility but for boiling experiments with two phase flow inside the particle bed poor reproducibility of the pressure measurements were observed (see left column in Figures 3.43 and 3.44).

For two phase flow in porous media (polydispersed and irregular particle bed), the poor reproducibility of the measurement results seems a typical phenomenon. The reasons for this may be:

- A complex liquid and vapor flow condition inside the particle bed (two phase flow in porous media).

- For particle beds (PDB and IPB) with mixture of different particle diameters, a change in porous bed structure, due to the repositioning of smaller particles into the voids between bigger particles, might result in measurement uncertainties.

In Figures 3.43 and 3.44 the data from 6 pressure measurements along the bed height (left columns) and probability distribution of the measurments (right columns) for two phase boiling experiment for IPB at a generator level 6.6 is shown. In the boiling processes no constant change in pressure was observed rather there were strong fluctuations around a constant average value (see left columns in Figures 3.43 and 3.44). In Figures 3.43 and 3.44

(see right columns) shows the probability distribution of the measured data for respective pressure measuments. Evaluation of the measured individual values for all 6 transducers installed along the particle bed height approximately follow a similar normal distribution. Therefore the pressure data presented in the results section was obtained from the average of all the measurements in each respective bed section (dp1 to dp6).

3.5.2 Volumetric Heat Generation

In heat input calibration experiments the particle bed was heated to below saturation temperatures and the temperature gradient was used to determine the volumetric heat generation ($\dot{Q}$) for respective generator level. Equations 3.1 and 3.2 (see section 3.1.1) were used to calculate the heat generation rate by polydispersed and irregular particle bed respectively. The physical properties of water and stainless-steel are standard values and so are not considered in uncertainty calculations. Due to the computerized recording of measurement data, the time interval dt is also not considered. The temperature is measured with thermocouples (type N) with an accuracy range of 0.2 K. Thus for determining the volumetric heat generation the uncertainty is limited to the temperature measurement and porosity determination. For porosity an uncertainty of 0.02 and for temperature difference between two time intervals an uncertainty of 0.4 K is considered. Based on adiabatic assumption, a temperature gradient of 10 °C is considered for the uncertainty analysis. According to the Gaussian error propagation law the uncertainty in volumetric heat generation Q can be determined by the following equation:

$$\Delta \overline{\dot{Q}} = \sqrt{\Delta \overline{\varepsilon}^2 \left(\frac{\partial \dot{Q}}{\partial \varepsilon} \right)^2 + \Delta \overline{T}^2 \left(\frac{\partial \dot{Q}}{\partial T} \right)^2}$$

Using above equation for a generator level 5 for PDB an uncertainty of less than 4%, in overall heat generation of the particle bed, is determined. Overall reliable accuracy of the measurements is achieved.

3.5.3 Vapor Superficial Velocity

For boiling experiments vapor superficial velocity is also an important parameter. With water in the bed at saturation temperature, the steam superficial velocity is calculated from the heat applied to the bed. In this case the possible uncertainties are related to the the above described volumetric heating power and the mass flow rate of the water. In case of pure top-flooding case, with no additional water injection, the uncertainty is limited to the heat generation only. But for bottom-flooding experiments with forced inflow of

water the uncertainty of the flow rate measurement should also be taken into account. Moreover, as the water being fed is at lower temperatures the energy needed to heat the water to saturation temperature has to be taken into account.

$$J_g = \frac{\dot{Q}.z - \dot{G}.C_p.\Delta T}{\rho_g.h_{fg}}$$

The possible uncertainty in determining the temperature of the inlet water is assumed to be negligible. Hence, the possible uncertainty of the steam superficial velocity is derived as follows:

$$\Delta \overline{J_g} = \sqrt{\Delta \overline{\dot{Q}}^2 \left(\frac{\partial J_g}{\partial \dot{Q}}\right)^2 + \Delta \overline{\dot{G}}^2 \left(\frac{\partial J_g}{\partial \dot{G}}\right)^2}$$

A bed section of height $z = 0.1 \ m$ is considered, which is also used for the measurement of pressure gradients. According to the manufacturer The flowmeter has an accuracy of 0.7%. In addition, a calibration curve as a function of pump frequency was created for feed rates below the measuring range. The error in the water mass flow should thus be less than 5%. If no water is fed, the error is exactly the error of the volumetric heating. It can be stated however that vapor superficial velocities greater than 0.1 m/s can be measured with an accuracy of approximately 5%.
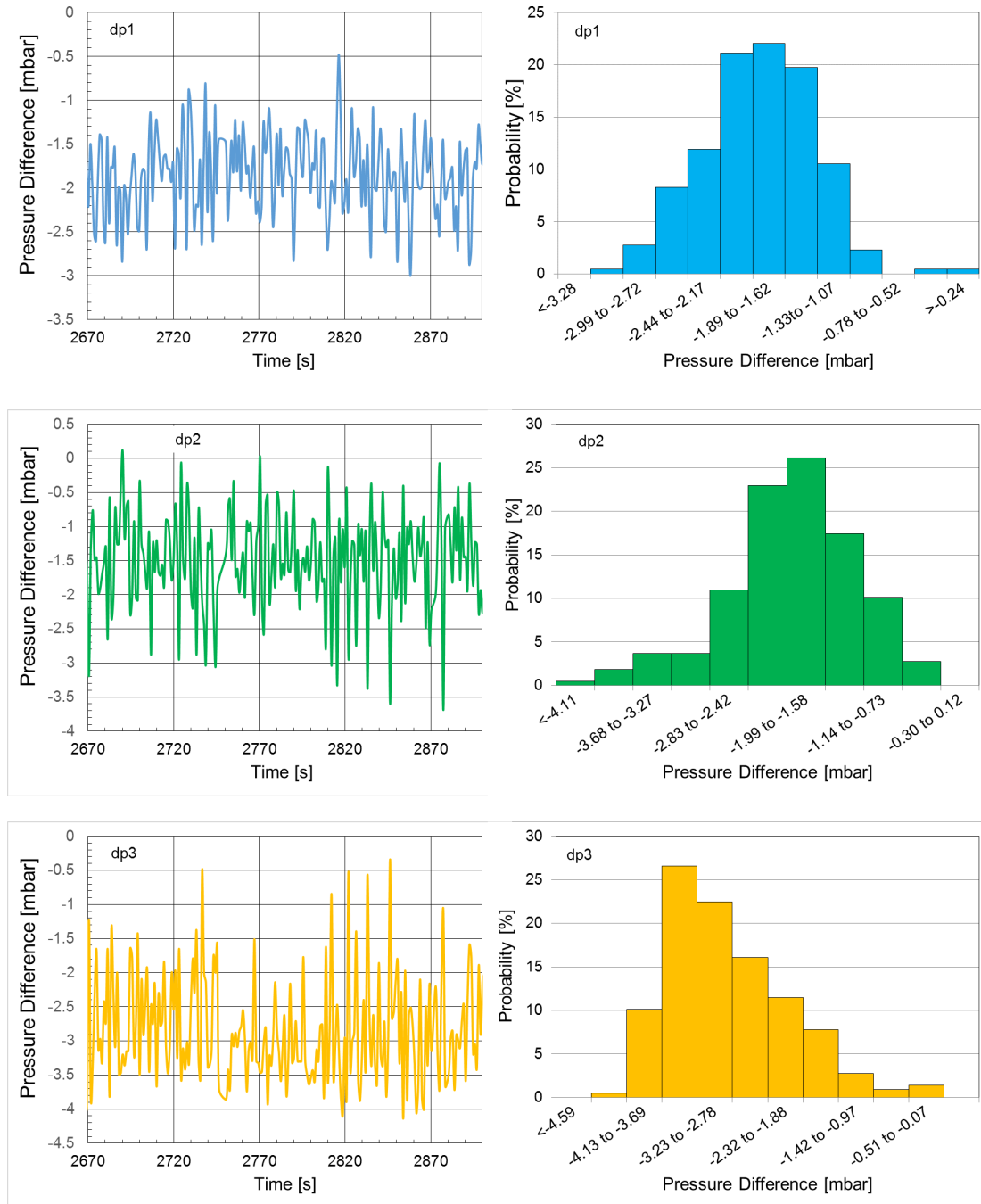
Figure 3.43: Two-phase pressure measurements for IPB in three bed sections (dp1-dp3) from along the bed height, generator level 6.6
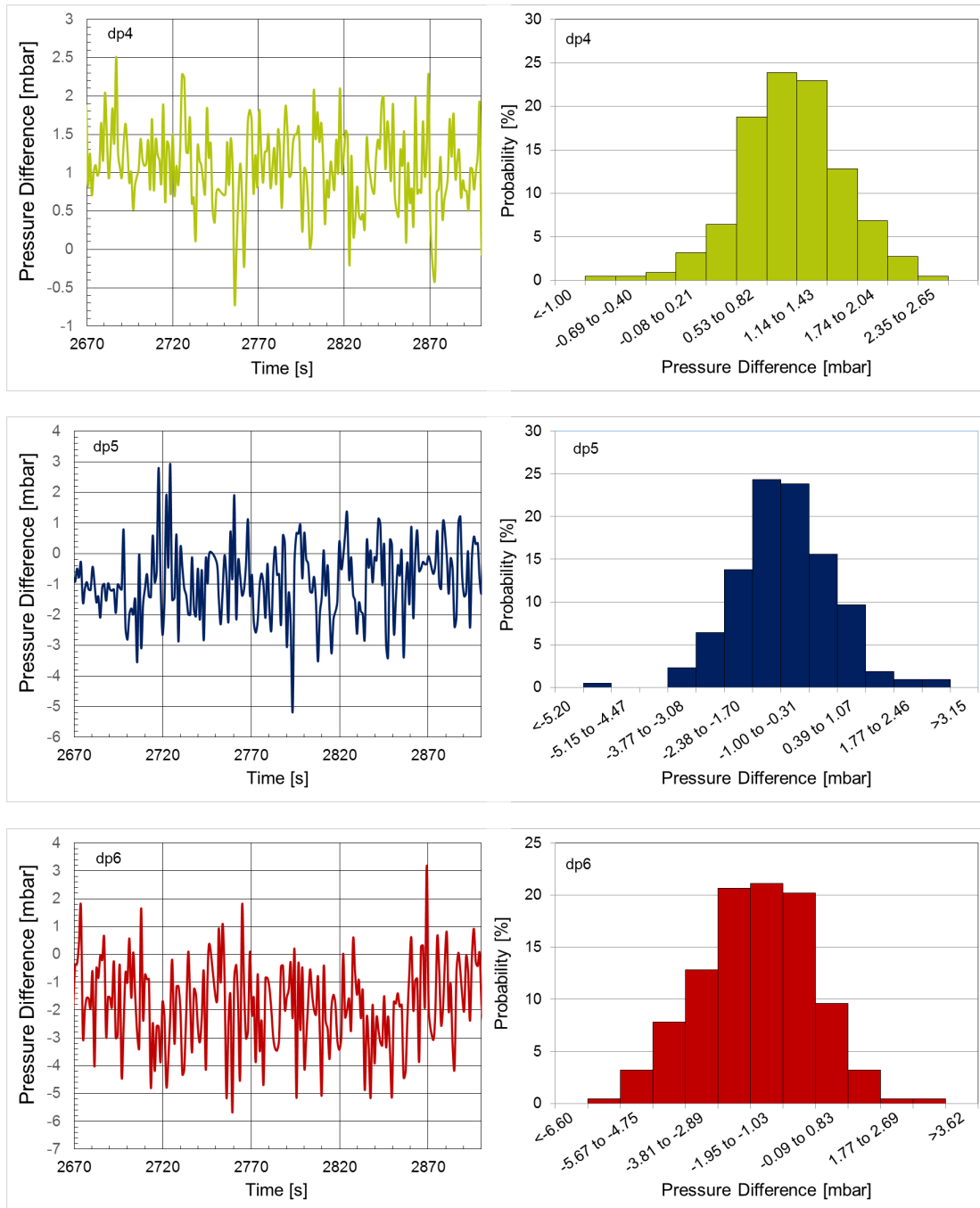
Figure 3.44: Two-phase pressure measurements for IPB in three bed sections (dp4-dp6) along the bed height, generator level 6.6

Chapter 4

Summary and Conclusion

The background of the present work is the fundamental question regarding the controllability of severe accidents with core meltdown in nuclear reactors and in this context, the coolability of particle beds with internal heat sources. The overall focus of the present work have been the boiling/dryout experiments on water-filled particle beds at saturation conditions and the flooding (quenching) experiments of dry, superheated particle beds. The individual objectives are related to two areas, the impact of different particle bed configurations (polydispersed particle bed (PDB) and irregular particle bed (IPB)) and the impact of different flow concepts (1D top-flooding, 1D bottom-flooding and 2D top-/ bottom-/ lateral-flooding) on the coolability of the particle (debris) beds. With respect to the above mentioned main focus areas and the objectives, the experimental resutls are summerized below.

In boiling/dryout experiments the differential pressure along the bed height, for given particle beds (PDB and IPB) and at different sytem pressures (1, 3 and 5 *bar*), was measured by pressure transducers. Moreover, the dryout heat flux (DHF), which is the maximum amount of heat that can be removed from the particle bed under steady state boiling conditions, was also determined. The boiling experiments with 1D top-flooding flow condition, without any additional water supply, for small vapor superficial velocities (J_g) generally show a marked decrease in pressure gradient. With increasing J_g values an increase in pressure gradients is observed which is followed by a second decrease in pressure gradient shortly before the appearance of dryout. Also for 1D bottom-flooding (via pump), at very small inflow rates, the pressure gradients tend to negative values but this trend diminishes with increasing water inflow rates and the pressure gradients indicate positive values over the whole water flow range. The pressure gradient behaviour for 1D bottom-flooding under hydrostatic head flow condition (internal and external downcomer) is also similar to the one obtained for the pure top-flooding case. This basic characteristic

behavior of the pressure gradient curve has been observed for all system pressures (1 bar, 3 bar and 5 bar). The measured typical pressure profiles have also been confirmed by model calculations by Rahman [59] and are characterized by the role of different friction forces e.g. particle friction and interphase friction. The measured pressure gradients for 2D top-/ bottom-/ lateral-flooding with internal perforated downcomer show only negative values. After initial decrease an equally strong increase in pressure drop is observed, which is followed by a renewed, even more powerful decrease in the pressure gradient near the DHF. Here, the maximum steam mass flows compared to corresponding values of the flow configuration with internal open downcomer are unexpectedly reduced by approximately 35%, which leads to a significant reduction of DHF.

For all the calculated DHF values a significant increase in DHF with an increase in system pressure is determined. With an increase in pressure from 1 bar to 5 bar the DHF increased in an order of about a factor of 1.7 (open downcomer, 1D top- / bottom-flooding), 1.8 (perforated downcomer, 2D top-/ bottom-/ lateral-flooding) and 2 (closed downcomer, 1D top-flooding). This significant increase is related to a pressure-dependent increase in the specific vapor densities and thus higher potential steam mass flows. In case of 1D bottom-flooding flow, a significant increase in the coolability of the particle beds was observed with DHF values of approximately 1.7 to 2.1 times higher than in 1D top-flooding flow conditions. The maximum dryout heat flux density of 2626 kW/m^2 ($p_{sys} = 5\ bar$) for experiments with open downcomer (1D top- / bottom-flooding), represents an increase of approximately 74% compared to the dryout heat flux density of 1509 kW/m^2 ($p_{sys} = 5\ bar$) for the experiments with closed downcomer (1D top-flooding). In contrast, for experiments with internal perforated downcomer (2D top-/ bottom-/ lateral-flooding) the DHF was maximum of about 30% ($p_{sys} = 1\ bar$) of the one obtained in experiments with closed downcomer (1D top-flooding). The possible explanation, for lower than expected DHF and DHF for 1D bottom-flooding flow condition, is the likely significant vapor flow into the perforated downcomer and hence resulting in impediment of downward water flow via downcomer (see also Section 3.2: 2D top-/bottom-/lateral-flooding (Water supply from top with perforated downcomer)). Due to poor heat generation by the irregularly shaped particles DHF could not be reached neither with internal nor external downcomer.

The primary objective of quenching (flooding) experiments was the analysis of heat transfer between dry superheated particle beds and the coolant. During the flooding process, for various initial temperature profiles (T_{max}) and different cooling concepts at system pressure 1 bar, the temperature measurements were carried out until the whole particle bed reached the saturation temperature.

4. SUMMARY AND CONCLUSION

The experiments with 1D top-flooding flow showed that for all particle bed configurations and regardless of initial temperature profile (T_{max}) a systematic quench front progression with two distinct stages of water ingression exist during the overall flooding process. During the first stage water infiltrated downwards in the near-wall regions of the particle bed in streak-like flow and primarily counter-current flow conditions prevailed in the near-wall regions of the particle bed. Later, once the water front reached the bottom of the particle bed, the second flooding stage started and the water resp. quenching front moved in the upward direction and is dominated by co-current flow condition inside the particle bed. The individual quench times, i.e. the required time until the whole particle bed reached the saturation temperature of 100 °C, varied with the initial temperature profile of the particle bed. Higher initial bed temperatures (T_{max}) resulted in longer cooling times, for example, the cooling times for polydispersed particle bed with initial temperature profiles $T_{max} = 354$ °C and $T_{max} = 680$ °C were about 420 s and 940 s respectively.

The experiments with 1D bottom-flooding were carried out under two inflow conditions, forced inflow (via pump) with constant coolant mass flows and natural circulation with differential pressure-driven (hydrostatic pressure difference between the water column and internal bed pressure, external downcomer) variable coolant mass flows. For both PDB and IPB, in contrast to the 1D top-flooding, uniformly extending, homogeneous flood front moving upwards was observed. With increased initial bed temperatures the flood front velocities decreased because higher heat content resulted in an increased steam production and therefore a greater liquid content of the total mass flow must be replaced for vaporization. For given experimental parameters no noticeable differences in the overall qualitative quench behavior of both particle bed configurations were found.

1D resp. 2D experiments with internal downcomer configurations (open and perforated downcomer) served as a transition to more realistic flow conditions in the particle bed. Due to technical difficulties (test section problems during heating) these experiments were carried out with reduced bed height and under moderate initial bed temperatures (average temperatures in the packed bed center between 340 °C and 380 °C). The objective of the experiments with internal downcomer was to investigate the quenching behavior of the particle beds with simultaneous top- and bottom-flooding flow (co- and counter-current flow). Furthermore, in case of the perforated downcomer, to study the quenching behavior of heated particle beds with, in addition to top- and bottom-flooding, lateral-flow via perforations in the central downcomer. With internal downcomer flow condition, for PDB, initially the upper bed sections reached the saturation temperature while in the later stage the lower bed sections are quenched through bottom-flooding via downcomer. During the

further course of the quenching process, a partial re-heating in the upper bed sections was observed whereas the core regions cooled gradually over the continuously rising flood front as in the case of bottom-flooding. By contrast, the quenching process in IPB was more marked by near-wall quenching process with downward coolant flow. At start the downward water flow mainly took place in the near-wall regions and via internal downcomer. In this case, no partial re-heating of the bed as in the case of PDB was observed. However, the quench times of both flood tests were found to be similar despite their different phenomenology.

The 2D quenching experiments for irregular particle bed with perforated downcomer showed no significant differences compared to the results with internal downcomer. The apparent faster cooling in the upper and lower bed sections than the rest of the bed could be explained by the lower initial temperatures of the bed before the start of the flooding.

For polydispersed particle bed, in comparison to internal downcomer 1D flow condition, with perforated downcomer 2D top-/bottom-/ lateral-flooding a different quench profile has been observed. On one hand the upper bed region is consistently cooled to saturation temperature, on the other hand stronger cooling takes place in the near-wall regions, i.e. the wall near regions of the test section is provided with coolant from top (counter-current flow) or from bottom (co-current flow) via downcomer. For both bed configurations, no significant temperature drop along the perforated downcomer has been observed, hence it could be assumed that no significant radial coolant flow from the perforated downcomer seems to take place. Rather, it is likely to assume that as in the case of boiling experiments with perforated downcomer, vapor flows into the downcomer and flows upwards against the downward flow of coolant leading to a counter-current flow situation inside the downcomer and hence reducing the overall availability of the coolant to the broader sections of the bed.

Based on the experimental data following conclusions are drawn below:

- The effective particle diameter, calculated from single phase pressure drop measurements of irregular particle bed (IPB) was found to be 3 mm and that of polydispersed particle bed (PDB), was 2.85 mm.

- In comparison to the PDB higher dryout heat flux (DHF) values, means better coolability, for IPB has been observed.

- For each particle bed configuration, with an increase in system pressure higher coolability (higher DHF) has been obsereved.

- Both particle beds (PDB and IPB) are always significantly better cooled under bottom-flooding flow conditions than under pure top-flooding flow conditions.

    - The improved radially symmetrical lateral flooding via perforated downcomer also results in a better coolability of the particle bed, although not as strong as in bottom-flooding.

  Despite experimental limitations, some useful basic understanding of the quenching of superheated particle beds (polydispersed particle bed and irregular particle bed) for different flow conditions is derived as follows:

- With increasing bed temperatures (T_{max}), the quench time also increased for all different flow conditions. Taking into account the individual bed temperatures, the longest quench times are observed with water being supplied to the superheated particle bed only from above (top-flooding)

- Comparing the quench time values with each other, the quench time for top-flooding flow condition is longer than that for bottom-flooding flow condition (with pump and with external downcomer).

- For quench times of bottom-flooding with internal open downcomer flow and lateral-flooding with perforated downcomer flow conditions, there exists marginal difference in the scope of the measurement accuracy.

One of the aim of this work was to contribute to the existing understanding and experimental database on the coolability of debris bed. A large number of experiments were carried out and the results were used for the validation of numerical code (MEWA-2D) (see also [58]). Keeping the complex nature of the debris bed in mind future studies may investigate wider particle bed variations, e.g. shape, diameter and porosity variation, downcomer configurations; variable perforation in the downcomer, position of the downcomer and a combination of different downcomer configurations.

References

[1] Kemeny, J. G.: "Report of the Presidents Commission on the Accident on Three Mile Island", Washington, D.C., October, 1979

[2] Buck, M.: Modelling of the Late Phase of Core Degradation in Light Water Reactors, Dissertation, Institut fr Kernenergetik und Energiesysteme (IKE), Universitt Stuttgart, IKE 2-153, November 2006.

[3] Wolf, J.R., Rempe, J.L., Stickler, L.A., Akers, D.W., North, G.E. and Neimark, L.A.: "TMI-2 Vessl Investigation Project Report", Idaho National Engineering Laboratory, Idaho Falls: OECD.NEA, 1993.

[4] Bürger, M., Cho, S.H., Berg, E.v. and Schatz, A.:"Break-up of Melt Jets as Precondition for Premixing: Modeling and Experimental Verification" J. Nucl. Eng. Des. 155, pp. 215-251, 1995.

[5] Pohlner, G., Vujic, Z., Bürger, M. and Lohnert, G.: Simulation of melt jet breakup and debris bed formation in water pools with IKEJET/IKEMIX, J. Nucl. Eng. Des. 236, pp. 2026-2048, 2006.

[6] Schmidt, W.: Influence of Multidimensionality and Interfacial Friction on the Coolability of Fragmented Corium, PhD Thesis, Institute of Nuclear Technology and Energy Systems (IKE), University of Stuttgart, IKE 2-149, 2004.

[7] Theofanous, T.G., Liu, C., Additon, S., Angelini, S., Kymlinen, O. and Salmassi, T.: In-vessel Coolability and Retention of Core Melt, J. Nucl. Eng. and Des. 169, pp. 1-48, 1997.

[8] Seiler, J.M., Latrobe, A., Sehgal, B.R., Alsmeyer, H., Kymlinen, O., Turland, B., Grange, J.L., Fischer, M., Azarian, G., Brger, M., Cirauqui, C.J. and Zurita, A.: Analysis of Corium Recovery Concepts by the EUROCORE group, J. Nucl. Eng. Des. 221, pp. 119-136, 2003.

REFERENCES

[9] Sehgal B. R.: Stabilisation and Termination of Severe Accidents in LWRs, J. Nucl. Eng. Des. 236, pp. 1941-1952, 2006.

[10] Fischer, M.: Main Conceptual Features of the EPR Melt Retention Concept, Proc. of the OECD Workshop on Ex-Vessel Debris Coolability, FKK, 15-18 November 1999.

[11] Tian Wan: Safety Issues of NPP with WWER: Research on Processes During Beyond Design Basis Accidents with Core Degradation, Proc. of the Applied Research Workshop, St. Petersburg, 12-14 September 2000.

[12] Fischer, M., Herbst, O. and Schmidt, H.: Demonstration of the Heat Removing Capabilities of the EPR Core Catcher, Nucl. Eng. Des. 235, pp. 11891200, 2005.

[13] Bittermann, D., Krugmann, U. and Azarian, G.: EPR Accident Scenarios and Provisions, J. Nucl. Eng. Des. 207, pp. 49-57, 2001.

[14] Alsmeyer, H., Albrecht, G., Fieg, G., Stegmaier, U., Tromm, W. and Werle, H.: Controlling and Cooling Core Melts Outside the Pressure Vessel, J. Nucl. Eng. Des. 202, pp. 269-278, 2000.

[15] Alsmeyer, H. and Tromm, W.: Experiments for a Core Catcher Concept Based on Fragmentation, Proc. of the ARS 94-International, Topical Meeting on Advanced Reactor Safety, April 2124, Pittsburgh, 1994.

[16] Widmann, W., Brger, M., Lohnert, G., Alsmeyer, H. and Tromm, W.: Experimental and Theoretical Investigations on the COMET Concept for Ex-vessel Core Melt Retention, J. Nucl. Eng. Des. 236, pp. 2304-2327, 2006.

[17] Takano, M., Nishi, T., Kurata, M., Amaya, M. and Nagase, F.: High Temperature Reaction Between UO2 and Sea Salt Deposit, 5th European Review Meeting on Severe Accident Research (ERMSAR-2012), Cologne (Germany), 21-23 March 2012.

[18] Dorsselaere, J.-P. V., Fichot, F. and Seiler, J.-M.: "Views on R&D Needs About In-vessel Reflooding Issues, with a Focus on Debris Coolability", J. Nucl. Eng. Des. 236, pp. 1976-1990, 2006.

[19] McCardell, R. K. , Russell, M. L., Akers, D.W. and Olsen, C. S.: Summary of TMI-2 Core Sample Examinations, J. Nucl. Eng. Des. 118, pp. 441-449, 1990.

[20] Spencer, B.W., Wang, K., Blomquist, C.A., McUmber, L.M. and Schneider, J.P.: Fragmentation and Quench Behaviour of Corium Melt Streams in Water, US Nuclear Regulatory Commission, NUREG/CR-6133, ANL-93/32 1994.

[21] Huhtiniemi, I., Magallon, D. and Hohmann, H.: Results of Recent KROTOS FCI Tests: Alumina vs. Corium Melts, Proc. of OECD/CSNI Specialists Meeting on Fuel-Coolant Interactions, Tokai-Mura (Japan), 1997.

[22] Huhtiniemi, I. and Magallon, D.: Insight into Steam Explosions with Corium Melts in KROTOS, Proc. of the 9th Int. Topical Meeting on Nuclear Reactor Thermal-Hydraulics (NURETH-9), San Francisco (USA), October 3-8, 1999.

[23] Magallon, D. and Huhtiniemi, I.: Corium Melt Quenching Tests at Low Pressure and Subcooling Water in FARO, J. Nucl. Eng. Des. 204, pp. 369-376, (2001).

[24] Magallon, D., Huntiniemi, I. and Hohmann, H.: Lessons Learnt from FARO/TERMOS Corium Melt Quenching Experiments, J. Nucl. Eng. Des. 189, pp. 223-238, (1999).

[25] Magallon, D.: Characteristics of Corium Debris Bed Generated in Large-scale Fuel-coolant Interaction Experiments, J. Nucl. Eng. Des. 236, pp. 1998-2009, (2006).

[26] Kato, M. and Nagasaka, H. et al.: Fuel Coolant Interaction Tests Under Ex-vessel Conditions, Proc. of the OECD Workshop on Ex-vessel Debris Coolability, Karlsruhe (Germany), 1999.

[27] Song, J.H. et al.: Insights from the Recent Steam Explosion Experiments in TROI, J. Nuclear Science and Technology 40 (10), pp. 783-795, (2003).

[28] Karbojian, A., Ma, W., Kudinov, P. and Dinh, T.: A Scoping Study of Debris Bed Formation in the DEFOR Test Facility, J. Nucl. Eng. Des. 239, pp. 1653-1659, (2009).

[29] Kaiser, A., Schtz, W. and Will, H.: "PREMIX Experiments PM12 - PM18 to Investigate the Mixing of a Hot Melt with Water, Wissenschaftliche Berichte, FZKA-6380, Forschungszentrum Karlsruhe GmbH, 2001.

[30] Li, L. and Ma, W.: Experimental Characterization of the Effective Particle Diameter of a Particulate Bed Packed with Multi-Diameter Spheres, J. Nucl. Eng. Des. 241, pp. 1736-1745, (2011).

[31] Richardson, J.F., Harker, J. and Backhurst, J.: Coulson and Richardson's CHEMICAL ENGINEERING Particle Technology and Separation Processes 5th Edition, Butterworth Heinemann, 2002.

[32] Abe, Y. and Sudo, Y.: Experimental measurement of frictional law under CCFL in porous debris. J. Nucl. Eng. Des. 236, pp. 2075-2083, (2006).

REFERENCES

[33] Lindholm, I., Holmstrom, S., Miettinen, J., 2006. Dryout heat flux experiments with deep heterogeneous particle bed. J. Nucl. Eng. Des. 236, pp. 2060-2074, (2006).

[34] Zeisberger, A and Mayinger, B.: Heat transport and void fraction in granulated debris. J. Nucl. Eng. Des. 236, pp. 2117-2123, (2006).

[35] Atkhen, K. and Berthoud, G.: SILFIDE experiment: Coolability in a volumetrically heated debris bed. J. Nucl. Eng. Des. 236, pp. 2075-2083, (2006).

[36] Takasuo, E., Holmstrm, S., Kinnunen, T., Pankakoski, P. H.: The COOLOCE experiments investigating the dryout power in debris beds of heap-like and cylindrical geometries, J. Nucl. Eng. and Des. 250, pp. 687- 700, (2012).

[37] Repetto, G. , Garcin, T., Eymery, S., March, P. and F. Fichot: Experimental program on debris re-flooding (PEARL) results on PRELUDE facility, Proc. Of 14th International Topical Meeting on Nuclear Reactor Thermal Hydraulics (NURETH-14), September 25-29, Toronto, Canada, 2011.

[38] Repetto, G. , Garcin, T., Eymery, S., March, P. and F. Fichot: Main outcomes on debris bed cooling from PRELUDE experiments, 5th European Review Meeting on Severe Accident Research (ERMSAR-2013), October 02-04, Avigon, France, 2013.

[39] Tutu, N. K., Ginsberg, T., Klein, J., Klages, J. and Schwarz, C. E.: Debris bed quenching under bottom flood conditions, Brookhaven National Laboratory, NUREG/CR-3850, BNL-NUREG-51788, 1984.

[40] Nayak, A. K., Sehgal, B. R. and Stepanyan, A. V.: An experimental study on quenching of a radially stratified heated porous bed, J. Nucl. Eng. and Des. 236, pp. 2189-2198, (2006).

[41] Tung, V. X. and Dhir, V. K.: Quenching of debris beds having variable permeability in the axial and radial directions, J. Nucl. Eng. and Des. 99, pp. 275-284, (1987).

[42] Sehgal, B.R., Konovalikhin, M.J., Yang, Z.L., Kazachkov, I.V., Amjad, M., Li, G.J.: Experimental Investigations on Porous Media Coolability, RIT/NPS Research report, 2001.

[43] Schäfer, P., Groll. M., Kulenovic. R.: Basic investigations on debris cooling, J. Nucl. Eng. and Des. 236, pp. 21042116, (2006).

[44] Schäfer, P., et al.: Wechselwirkung Debris/RDB-Wand: Analytische und experimentelle Untersuchung zur Khlbarkeit und Rckhaltung verlagerten Kernmaterials (Debris) im unteren RDB-Plenum eines LWR, Abschlussbericht FKZ 150 1011, IKE 5TB-1751-03, 2003, ISSN 0173-6892, 2003.

[45] Schäfer, P: Experimentelle Untersuchungen zur Khlbarkeit volumetrisch beheizter Schttbetten, Dissertation, Institut fr Kernenergetik und Energiesysteme (IKE), Universitt Stuttgart, IKE 5-256, Juli 2005.

[46] Groll, M., Schäfer, P. and Kulenovic, R.: Experimental Investigation on the Coolability of Porous Media. Proc. of the International Workshop on New Horizons in Nuclear Reactor Thermal Hydraulics, Mumbai, 7-8 January 2008.

[47] Buck, M. Bürger, M., Rahman, S., Pohlner, G.: Validation of the MEWA model for quenching of a severely damaged reactor core, Joint OECD/NEA EC/SARNET2 Workshop on In-Vessel Coolability, October 12 14, Paris, France, 2009.

[48] Fichot, F., Duval, F., Tregoures, N., Bechaud, C., Quintard, M.: The impact of thermal non-equilibrium and large-scale 2D/3D effects on debris bed reflooding and coolability, Nucl. Eng. Des. 236, 2144-2163, (2006).

[49] Darcy, H.: Les Fontaines Publiques de la Ville de Dijon, Dalmont, Paris, 1856.

[50] Ergun, S.: Fluid Flow Through Packed Columns, J. Chem. Eng. Progress 48 (No.29), pp. 89-94, (1952).

[51] Kaviany, M.: Principles of Heat Transfer in Porous Media. Second ed. Springer, New York, 1995.

[52] Lipinski, R. J.: A Model for Boiling and Dryout in Particle Beds. Sandia National Laboratories, SAND 82-9765, NUREG/CR-2646, 1982.

[53] REED, A. W.: The effect of channeling on the dryout of heated particulated beds immersed in a liquid pool, PhD Thesis, Massachusetts Institute of Technology, Cambridge, 1982.

[54] Hu, K. and Theofanous, T. G.: On the measurement of dryout in volumetrically heated coarse particle beds, Int. J. Multiphase Flow 17 (4), 519532, (1991).

[55] Tutu, N. K., Ginsberg, T. and Chen, J. C.: Interfacial Drag for Two-Phase high permeability porous beds, J. of Heat Transfer, 106, 865-870, (1984).

REFERENCES

[56] Hofmann, G.: On the location and mechanisms of dryout in top-fed and bottom-fed particulate beds, Nucl. Technology 65, 3645, (1984).

[57] Schulenberg, T. and Müller, U.: A refined model for the coolability of core debris with flow entry from the bottom, Proc. of the Sixth Information Exchange Meeting on Debris Coolability, University of California, Los Angeles, EPRI NP-4455, March, 1986.

[58] Tung, V. X. and Dhir, V. K.: A hydrodynamic model for two-phase flow through porous media, J. Multiphase Flow, Vol. 14 (No. 1), 4765, (1988):

[59] Rahman, S.: Coolability of corium debris under severe accident conditions in Light water reactors, PhD Thesis, Institute of Nuclear Technology and Energy Systems (IKE), University of Stuttgart, IKE 2-155, 2013.

[60] Haga, D., Niibori, Y. and T. Chida: Tracer responses in gas-liquid two-phase flow through porous media, Proceeding of the World Geothermal Congress, Kyushu, Tohoku, Japan, 2000.

[61] Stürzel, T.: Ultraschnelle Röntgen Tomographie zur Untersuchung Zweiphasiger Strömung in Porösen Medium, PhD Thesis, Institute of Nuclear Technology and Energy Systems (IKE), IKE 8-118, University of Stuttgart, 2013.

[62] Boldt, T.: Experimentelle Untersuchungen zum zweidimensionalen Flutverhalten stark überhitzter Partikelschüttungen, Diplomarbeit, IKE 8D-71, Institut für Kernenergetik und Energiesysteme, Universität Stuttgart, Januar 2012.

[63] Rashid M., Chen, Y., Kulenovic R. and Laurien E.: Experiments on the Coolability of a Volumetrically Heated Particle Bed with Irregularly Shaped Particles, Proc. of the 7th International Topical Meeting on Nuclear Reactor Thermal Hydraulics, Operation and Safety (NUTHOS-7), Seoul, (Korea), October 5-9, 2008.

[64] Kulkarni P.P., Rashid M., Kulenovic R., Nayak A.K., Experimental Investigation of Coolability Behaviour of Irregularly Shaped Particulate Debris Bed, J. Nucl. Eng. and Des. 240, pp. 3067-3077, (2010).

[65] Rashid M., Kulenovic R., Laurien E. and Nayak A. K., Experimental Results on the Coolability of a Debris Bed with Multidimensional Cooling Effects, J. Nucl. Eng. and Des. 241, pp. 4537-4543, (2011).

[66] Rashid M., Kulenovic R. and Laurien E., Experimental Results on the Coolability of Debris Bed with Down Comer Configurations, NJ. Nucl. Eng. and Des. 249, pp. 104-110, (2012).

[67] Rashid M., Rahman S., Kulenovic R. Bürger M. and Laurien E., Quenching Experiments: Coolability of Debris Bed, Nucl. Technology 181, pp. 208-215, (2013).

Appendix A

Application of Experimental Results For Validation of Numerical Models in Melt Water Code

Experimental database of this research work was extensively used by Rahman [59] for the validation of numerical models implemented in MEWA (MElt WAter) code. Schmidt [6] had modified the original Tung & Dhir model suggesting that, for particles with smaller diameters, a steep transition towards slug and annular flow regimes (see Figure A.1)takes place. The modifications made by Schmidt have been incorporated into the friction formulations in the MEWA code, which is fundamentally based on the Tung & Dhir model. Rahman [59] suggested following further modifications to the MEWA code:

- He suggested the flow patterns in the bubbly and slug flow regimes with a gradual decrease in void fraction (see Figure A.1), as compared to the rapid decrease suggested by Schmidt [6].

- Further modified the relative permeabilities and passabilities for vapor/particle and liquid/particle friction. The classical Tung & Dhir model predicts dryout heat flux too low for counter-current flow conditions (top-flooding), which may be caused by interfacial friction that is too high.

- Also introduced a reduction factor to the interfacial friction in the bubbly, slug, and annular flow regimes.

By Rahman [59] calculated DHF values with different friction models and reported the best results were found with the modified Thung and Dhir (MTD) approach. Hence in this
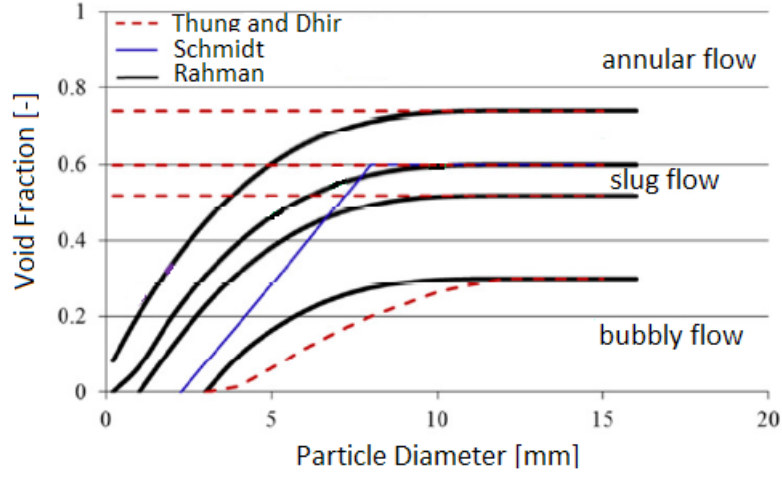
Figure A.1: Different flow pattern maps [59]

section only the comparison is discussed for selected experiments and the corresponding MEWA calculations with modified Thund and Dhir model.
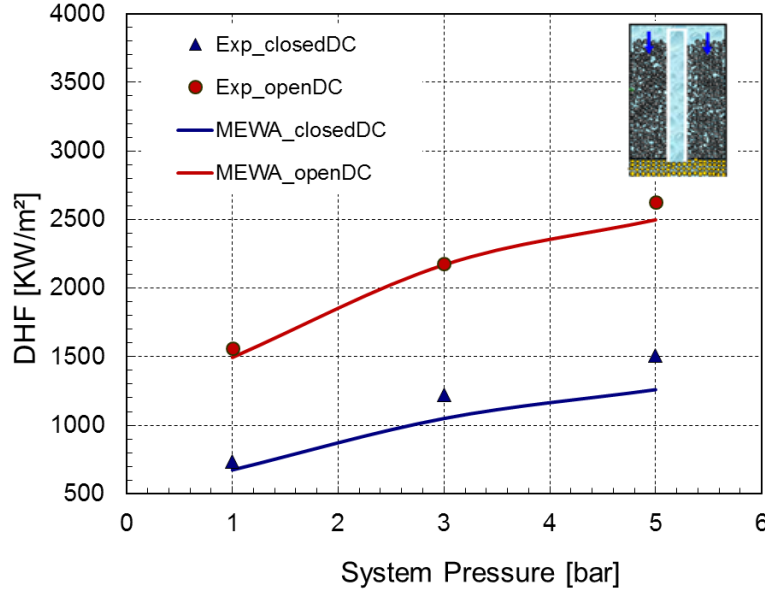
A.1 Dryout Heat Flux

Figure A.2 represents a comparison between the experimental results and corresponding MEWA calculations by Rahman [59] for dryout heat flux values for polydispersed particle bed (PDB). Comparison is made for two different flow configurations (closed downcomer and open downcomer)at three different system pressures ($1, 3$ and $5 bar$). The measured bed porosity of 0.36 and the effective particle diameter (d_e) of 2.9 mm, as determined from single phase pressure drop calculations (by Ergun's Eq.), was considered for numerical calculations. The numerical simulation results with MTD model gave a very good approximation of the DHF values (see Figure A.2). From calculations it is also evident that the DHF for bottom-flooding (open downcomer) was much higher than that for top-flooding (closed downcomer) case.

A.2 Quenching

The particle bed is inductively heated to pre-defined temperatures. Due to unavoidable heat losses from the wall of the test section to the surroundings and a non-uniform heat generation by the particle bed, a non-uniform temperature profile exists inside the particle bed. The quenching experiments were only performed at ambient pressure (1 bar). The bottom flooding was provided via an external lateral water column and the hydrostatic

Figure A.2: Dryout heat flux for PDB with closed and open downcomer configurations and corresponding MEWA results with modified Thung and Dhir model [59], $p_{sys} = 1/3/5$ bar

head of the water column was 950 mm. Rahman [59] performed calculations for quenching experiments with initial bed temperatures from 400 to 700 °C. For MEWA calculation the bed porosity of 0.36 and an effective particle diameter (d_e) of 2.9 mm was considered. The calculations were performed with the MEWA code for axisymmetric geometry. A pressure boundary condition was defined at the bottom of the bed. Similar to the experiments, axial and radial temperature profiles were chosen with lower bed temperatures at the bottom and in the near wall regions. Figure A.3 shows the MEWA calculation for temperature
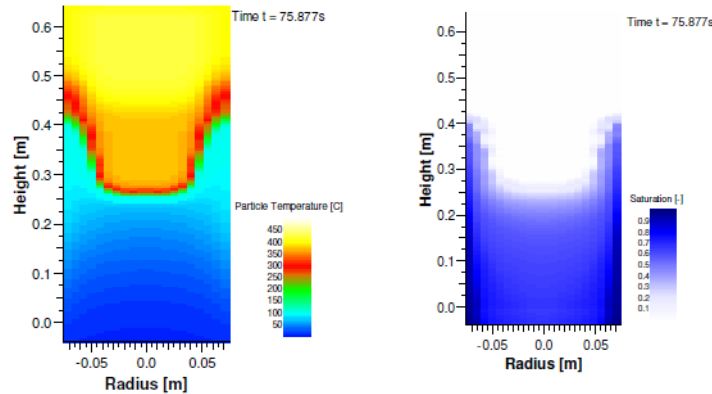
Figure A.3: Distribution of temperature and saturation (water contained inside the bed) from a MEWA-2D simulation for the test, BF400, $p_{sys} = 1$ bar [59]

distribution and saturation for PDB. The faster quench front progression in the near

wall regions was also captured in the calculations (see Figure A.3). Comparison between experimental data and the MEWA calculation of quench front progression for different initial bed temperature profiles is given in Figure A.4. The MEWA results show a good agreement with the quench time data as well as with the quench velocities. In both, the experiments and the calculations slower quench velocities were obtained for higher bed temperatures. This is mainly attributed to, at higher bed temperatures, the higher thermal energy content. Overall Rahman [59] reported a good agreement between the MEWA calculations and different experiments carried out in this thesis.
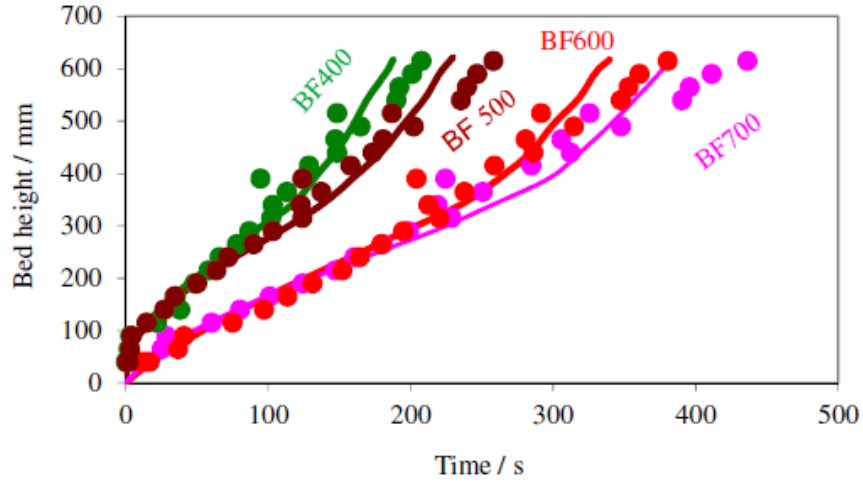
Figure A.4: Comparison of measured and calculated quench-front progression in the center of the bed for bottom-flooding with different initial bed temperatures, $p_{sys} = 1$ bar [59]